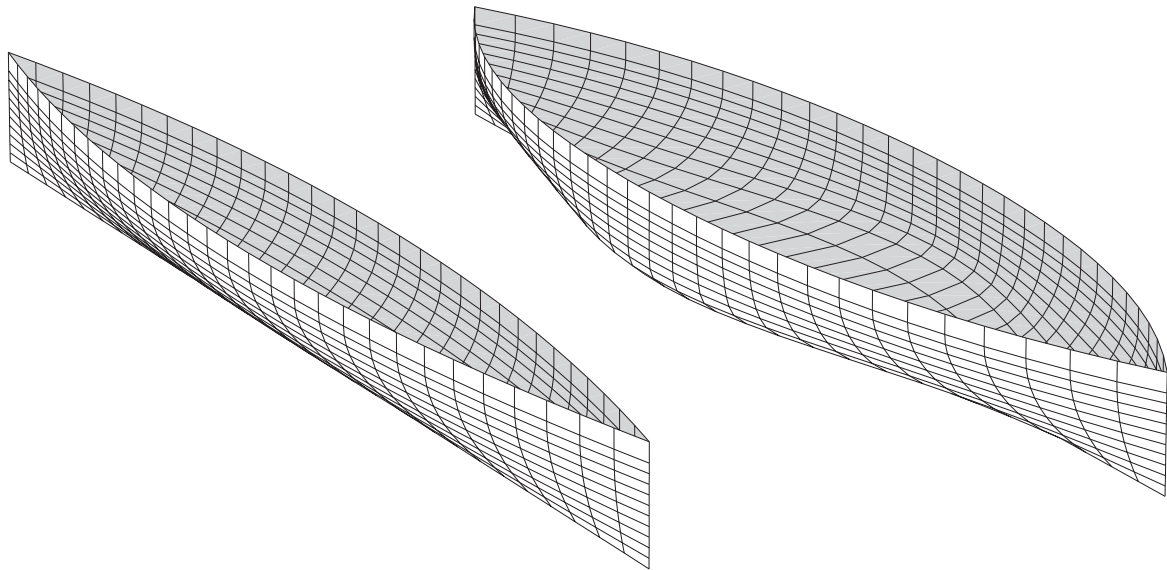


CHALMERS



Potential of Rolls-Royce HYDRA Code for Ship Hull Performance Prediction

Master of Science Thesis

ERIK WIBERGER
GABRIEL ÖSTLING

Department of Shipping and Marine Technology
Division of Sustainable Ship Propulsion
CHALMERS UNIVERSITY OF TECHNOLOGY
Gothenburg, Sweden 2010
Report No. X-10/248

A THESIS FOR THE DEGREE OF MASTER OF SCIENCE

Potential of Rolls-Royce HYDRA Code for Ship Hull Performance Prediction

ERIK WIBERGER

GABRIEL ÖSTLING



Department of Shipping and Marine Technology

CHALMERS UNIVERSITY OF TECHNOLOGY

Gothenburg, Sweden 2010

Potential of Rolls-Royce HYDRA Code for Ship Hull Performance Prediction

ERIK WIBERGER

GABRIEL ÖSTLING

© ERIK WIBERGER & GABRIEL ÖSTLING, 2010

Report No. X-10/248

Department of Shipping and Marine Technology

Chalmers University of Technology

SE-412 96 Gothenburg

Sweden

Telephone +46 (0)31-772 1000

Printed by Chalmers Reproservice

Gothenburg, Sweden 2011

Abstract

In this study the potential of Rolls-Royce in-house CFD code HYDRA, designed for high speed flows in gaseous fluids, is investigated for ship performance prediction in a marine environment. Using two different test cases in form of well known Wigley hull shapes the code is validated against commercially available software FLUENT and previously known results from experimental testing. Since HYDRA requires an ideal gas as the working fluid the surrounding conditions have been scaled from water to a fictional ideal gas with respect to the Reynolds number. Free surface solution is not possible at this point in HYDRA, therefore the hulls have been considered fully submerged.

The parameters that have been studied are Mach number, mesh, mesh boundary layer resolution, convergence and CPU time. For comparison of the results the total resistance, as well as its decomposition into pressure and viscous resistance, have been observed. Simulations have been done at Mach numbers between $1 \cdot 10^{-6}$ and 0.7 and y^+ between 1 and 120 using both k- ω SST and Spalart-Allmaras as turbulence models. Both structured and unstructured meshes have been applied.

The results show that HYDRA, using an unstructured mesh with Mach number 0.01 and y^+ at 1, calculates the total resistance 2.3% higher than FLUENT and 3.85% lower than experimental results. However, as the Mach number in HYDRA increases the results become inconsistent, e.g. between Mach number 0.01 and 0.25 the total resistance increases around 3%. Even if that would bring HYDRA closer to the experimental results it is a highly unwanted effect since consistency is considered significantly more important than accuracy in CFD. When using unstructured meshes with higher y^+ HYDRA displays difficulties predicting accurate viscous and pressure resistance contributions. With a structured Mesh HYDRA is comparable to FLUENT and shows none of the above mentioned problems. In CPU time FLUENT was proven to be superior for these type of cases.

Keywords: Computational Fluid Dynamics, Wigley hull, FLUENT, HYDRA, GAMBIT, RANS, Spalart-Allmaras, k- ω SST, Mach number, y^+ , Comparison

Preface

This thesis is the final piece in the study for the Master's degree at Chalmers University of Technology, Gothenburg, and has been carried out at the Department of Shipping and Marine Technology, Chalmers University of Technology, together with Rolls-Royce Marine in Derby, UK.

We would primarily like to thank our main sources of assistance during the project; our supervisors Alec Wilson, David Radford and Indi Tristante at Rolls-Royce. Without their effort and guidance this project would have been impossible. We would also like to extend our gratitude to everyone else working in the Aerothermal methods group at Rolls-Royce that helped us throughout the project.

Finally we would like to thank our examiner Professor Rickard Bensow at Chalmers that helped to make this project possible.

Table of Contents

1	Introduction.....	3
1.1	Background.....	3
1.2	Objective.....	3
1.3	Methodology.....	3
2	Basic theory.....	5
2.1	Ship resistance.....	5
2.2	Navier-Stokes equations.....	5
2.3	Ideal gas behaviour.....	7
2.3.1	Equations of state.....	7
2.3.2	Sutherland’s law.....	8
2.3.3	Compressibility.....	9
2.4	RANS.....	9
2.5	Turbulence models.....	11
2.5.1	Spalart-Allmaras.....	11
2.5.2	k- ω SST.....	12
2.6	Boundary layer and its modelling.....	12
2.6.1	Wall functions.....	14
2.6.2	Slip wall function.....	15
2.7	Cell vs. Node based solver.....	16
2.8	Coupled vs. Segregated solver.....	17
2.9	HYDRA.....	17
2.9.1	Flux evaluation.....	17
2.9.2	Multigrid.....	19
2.9.3	Pre-conditioner.....	19
2.9.4	Low Mach number pre-conditioning.....	20
2.10	FLUENT.....	21
2.10.1	Pressure – Velocity coupling.....	22
2.10.2	Gradient.....	23
2.10.3	Upwind scheme.....	23
2.10.4	Under relaxation factors.....	24
2.10.5	Multigrid.....	24
3	Test cases.....	25
3.1	Mathematical definition and main particulars.....	25
3.2	Operating conditions.....	26
3.3	Geometry generation.....	26
3.4	Meshing.....	27
3.4.1	Wigley I.....	27
3.4.2	Wigley II.....	28
3.4.3	Wigley II structured.....	31

4	Hydra setup	33
4.1	Similarity.....	33
4.2	Scaling of input values.....	34
4.2.1	SI.....	35
4.2.2	STP2.....	36
4.3	Boundary conditions.....	38
4.4	Solution methods	39
5	FLUENT setup.....	41
5.1	Boundary conditions.....	41
5.2	Fluid properties	42
5.3	Solution methods	42
6	Results and discussion	43
6.1	Experimental results.....	43
6.1.1	Wigley I.....	44
6.1.2	Wigley II.....	44
6.2	Mach number dependence	45
6.3	Dependence of boundary layer resolution.....	48
6.3.1	Introducing Slip Wall	50
6.4	Spalart-Allmaras vs. k- ω SST.....	53
6.5	Froude number span	55
6.6	Wake cuts	55
6.7	Convergence.....	57
6.7.1	HYDRA.....	58
6.7.2	FLUENT	62
6.8	CPU utilisation	63
6.8.1	CPU time Default vs. LMNP	63
6.8.2	CPU time vs. boundary layer resolution.....	64
6.8.3	Scalability.....	65
6.8.4	CPU time HYDRA vs. FLUENT	66
7	Conclusions.....	67
8	Further work.....	69
9	References.....	71
	Appendix A – Calculations	I
	Appendix B – Corrections	V
	Appendix C – Line drawings.....	VII
	Appendix D – Figures.....	IX
	Appendix E – Tables	XI
	Appendix F – Hull generation	XV

Nomenclature

Latin Characters

B	Beam
c	Sound speed
C_b	Block coefficient
C_p	Pressure resistance coefficient
C_t	Total resistance coefficient
C_v	Viscous resistance coefficient
c_p	Specific heat for constant pressure
c_v	Specific heat for constant volume
d	Draught
e	Internal energy
Fn	Froude number
L	Length
Ma	Mach number
P	Pressure
R	Specific gas constant
Re	Reynolds number
S	Wetted surface
S_{suth}	Sutherland's temperature
T	Temperature
y^+	Dimensionless wall distance

Greek Characters

γ	Adiabatic index
μ	Dynamic viscosity
κ	Von Kármán's constant
ν	Kinematic viscosity
ρ	Density
$\tau_{xx}, \tau_{yy}, \tau_{zz}$	Normal stresses
$\tau_{xy}, \tau_{xz}, \tau_{yz}$	Shear stresses

Acronyms

AMG	Algebraic Multigrid
CFD	Computational Fluid Dynamics
CFL	Courant-Friedrichs-Levy
CPU	Central Processing Unit
DOF	Degrees of Freedom
FVM	Finite Volume Method
ITTC	International Towing Tank Conference
LMNP	Low Mach Number Pre-conditioning
LPP	Length between perpendiculars
MUSCL	Monotonic Upstream-centered Scheme for Conservation Laws
N-S	Navier-Stokes
RANS	Reynolds Average Navier-Stokes
S-A	Spalart-Allmaras
SI	International system of units
SIMPLE	Semi-Implicit Method for Pressure-Linked Equation
SST	Shear Stress Transport
STP	Standard Temperature Pressure

1 Introduction

1.1 Background

HYDRA is a Rolls-Royce proprietary CFD code which so far has been developed for high speed flows in aero engine and industrial applications with air as the working fluid. Hence it is written as a coupled solver that uses the Equations of State to close the Navier-Stokes equations and therefore it will interpret all fluids as compressible ideal gases and has no real capability to simulate water. One possible way around this is to use one of the built in features in HYDRA; namely the Low Mach Number Pre-conditioner (LMNP) that will let the code run smoothly at really low Mach numbers, where even air is considered to be incompressible. I.e. there is a possibility of using HYDRA as a numerical wind tunnel in which applications intended for water are tested.

The recommendation when running HYDRA is to use a structured mesh with y^+ around one, i.e. well within the viscous sub layer. Since these meshes often requires longer calculation time (from their high number of degrees of freedom) and can sometimes result in skewed cells and high aspect ratios they are not always preferable. Further there are many situations where the geometry, e.g. appendages on a hull, makes it almost impossible to use a structured mesh. Therefore it is of interest to investigate how HYDRA will perform with unstructured meshes and coarser boundary layers which are more suitable for marine use.

Turning HYDRA into a fully capable marine code would require substantial work. Rolls-Royce has to balance the cost of developing and maintaining HYDRA as a marine code against the cost of licensing a commercial CFD code. This study shall be seen as a first step on the way to evaluate how well HYDRA can perform in a marine environment.

1.2 Objective

Investigate use of Rolls-Royce in-house aerodynamic CFD code HYDRA to calculate ship performance.

- Establish penalty/benefit of HYDRA relative to commercial FLUENT code in terms of CPU time and mesh requirements for equivalent accuracy.
- Establish relationship between HYDRA code stability and run time versus Mach number using both LMNP and default settings.
- Investigate differences between Spalart-Allmaras and k- ω SST turbulence models.

1.3 Methodology

Steady RANS calculations made in HYDRA have been evaluated against experimental results and equivalent calculations in FLUENT. The comparisons have mainly been focused on resistance prediction, mesh dependence and CPU time consumption. As test cases two different Wigley hulls, originally found in Ju [11] and Journée [10], have been modelled with Fortran code into STL files and then meshed in different manners using GAMBIT. Data over resistance prediction and convergence histories from both HYDRA and FLUENT have been saved into a specially designed MATLAB program. The purpose of it was to easily evaluate data based on different parameters. All graphs included in this report have been extracted from that program. All graphical post processing, such as wake cut and pressure comparisons, have been done using JLO9 and PARAVEIW.

2 Basic theory

2.1 Ship resistance

In hydrodynamics there are numerous approaches when it comes to grouping the forces acting on a hull together. One common way described in Larsson and Raven [12] is to divide the total force into two main components, viscous and wave resistance. The viscous part contains the “flat plate friction”, “roughness” (neglected at model scale or in CFD), “form effect friction” and the “form effect pressure”. The wave part contains the “wave making and breaking”. The latter is not studied in this report since HYDRA currently does not have any free surface model.

Contrary to the common practice results from both HYDRA and FLUENT (disregarding the free surface) presents the total force separated into viscous resistance and pressure resistance. The form effect pressure is no longer part of the viscous resistance, instead it becomes a term of its own called pressure resistance. The way the forces are divided can best be described as tangential (viscous) and normal forces (pressure).

For this reason when the viscous resistance includes the “form pressure effect”, as in Ju [11] from where some of the experimental reference values (presented in Section 6.1) were taken, it is from now referred to as the total resistance. Further, the total resistance or the total resistance coefficient does not include the wave making and breaking unless it is said so. The following definitions are made

C_v – Viscous resistance coefficient (tangential forces)

C_p – Pressure resistance coefficient (normal forces)

$C_t = C_v + C_p$ – Total resistance coefficient

2.2 Navier-Stokes equations

The basic governing equations behind fluid dynamics, generally called the Navier-Stokes equations are shown in differential conservation form. That implies that the fluid is moving through an infinitesimal control volume, dV , fixed in space. Further they are presented in the full compressible (ρ changes with time and space) and viscous form.

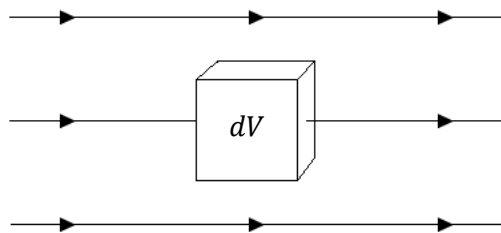


Figure 2.1: Infinitesimal control volume, dV , fixed in space.

First some basic definitions are made.

The vector velocity field

$$\mathbf{V} = (u, v, w) \quad (2.1)$$

where the scalar field's u , v , and w , giving the velocity component in each of the three Cartesian directions, are defined as

$$u(x, y, z, t)$$

$$v(x, y, z, t)$$

$$w(x, y, z, t)$$

The magnitude of velocity V at any given point in space is then

$$V = \sqrt{u^2 + v^2 + w^2} \quad (2.2)$$

The density scalar field is defined as

$$\rho(x, y, z, t)$$

The “force per unit mass” (body force terms e.g. gravity) vector field is defined as

$$\mathbf{f} = (f_x, f_y, f_z) \quad (2.3)$$

The first of the Navier-Stokes equations is the continuity equation, which states that mass is conserved. In words it has been described “The mass flow out of the element must equal the time rate of decrease of mass inside the element”, John D. Anderson [2].

$$\frac{\partial \rho}{\partial t} + \nabla \cdot (\rho \mathbf{V}) = 0 \quad (2.4)$$

The second equation is really a set of equations, one for each of the three Cartesian directions. The principle of the equations is Newton’s second law that gives the relationship between force, mass and acceleration ($F = ma$). They are called the Momentum equations.

$$\frac{\partial(\rho u)}{\partial t} + \nabla \cdot (\rho u \mathbf{V}) = -\frac{\partial p}{\partial x} + \frac{\partial \tau_{xx}}{\partial x} + \frac{\partial \tau_{yx}}{\partial y} + \frac{\partial \tau_{zx}}{\partial z} + \rho f_x \quad (2.5)$$

$$\frac{\partial(\rho v)}{\partial t} + \nabla \cdot (\rho v \mathbf{V}) = -\frac{\partial p}{\partial y} + \frac{\partial \tau_{xy}}{\partial x} + \frac{\partial \tau_{yy}}{\partial y} + \frac{\partial \tau_{zy}}{\partial z} + \rho f_y \quad (2.6)$$

$$\frac{\partial(\rho w)}{\partial t} + \nabla \cdot (\rho w \mathbf{V}) = -\frac{\partial p}{\partial z} + \frac{\partial \tau_{xz}}{\partial x} + \frac{\partial \tau_{yz}}{\partial y} + \frac{\partial \tau_{zz}}{\partial z} + \rho f_z \quad (2.7)$$

Where the following is valid for Newtonian¹ fluids,

$$\tau_{xx} = \lambda(\nabla \cdot \mathbf{V}) + 2\mu \frac{\partial u}{\partial x} \quad (2.8)$$

$$\tau_{yy} = \lambda(\nabla \cdot \mathbf{V}) + 2\mu \frac{\partial v}{\partial y} \quad (2.9)$$

¹ A fluid which has a linear relationship between shear stress and velocity gradient.

$$\tau_{zz} = \lambda(\nabla \cdot \mathbf{V}) + 2\mu \frac{\partial w}{\partial z} \quad (2.10)$$

$$\tau_{xy} = \tau_{yx} = \mu \left(\frac{\partial v}{\partial x} + \frac{\partial u}{\partial y} \right) \quad (2.11)$$

$$\tau_{xz} = \tau_{zx} = \mu \left(\frac{\partial w}{\partial x} + \frac{\partial u}{\partial z} \right) \quad (2.12)$$

$$\tau_{yz} = \tau_{zy} = \mu \left(\frac{\partial w}{\partial y} + \frac{\partial v}{\partial z} \right) \quad (2.13)$$

where λ is the second viscosity often used as

$$\lambda = -\frac{2}{3}\mu \quad (2.14)$$

The final Navier-Stokes equation is the Energy equation which states that energy is conserved. Its physical principle is the first law of thermodynamics (energy can change from one form to another but cannot be created nor destroyed).

$$\begin{aligned} \frac{\partial}{\partial t} \left[\rho \left(e + \frac{V^2}{2} \right) \right] + \nabla \cdot \left[\rho \left(e + \frac{V^2}{2} \right) \mathbf{V} \right] \\ = \rho \dot{q} + \frac{\partial}{\partial x} \left(k \frac{\partial T}{\partial x} \right) + \frac{\partial}{\partial y} \left(k \frac{\partial T}{\partial y} \right) + \frac{\partial}{\partial z} \left(k \frac{\partial T}{\partial z} \right) - \frac{\partial (up)}{\partial x} - \frac{\partial (vp)}{\partial y} \\ - \frac{\partial (wp)}{\partial z} + \frac{\partial (u\tau_{xx})}{\partial x} + \frac{\partial (u\tau_{yx})}{\partial y} + \frac{\partial (u\tau_{zx})}{\partial z} + \frac{\partial (v\tau_{xx})}{\partial x} + \frac{\partial (v\tau_{yx})}{\partial y} \\ + \frac{\partial (v\tau_{zx})}{\partial z} + \frac{\partial (w\tau_{xx})}{\partial x} + \frac{\partial (w\tau_{yx})}{\partial y} + \frac{\partial (w\tau_{zx})}{\partial z} + \rho \mathbf{f} \cdot \mathbf{V} \end{aligned} \quad (2.15)$$

By summarizing the unknowns in the equations above one can easily see and understand that the numbers of unknowns are six (ρ, p, u, v, w, e) while the numbers of equations only are five, i.e. further equations are needed to close the solution. When the working fluid is an ideal gas, e.g. air as in HYDRA, it is possible to achieve with the ideal gas equation together with the caloric equation of state, both described in the next section.

In a case where the fluid is incompressible and ρ is considered constant, as in water, the closing problem disappears since there is no need for using the Energy equation. Hence the number of unknown's drops down to four and the solutions is closed by only the Continuity and the Momentum equations.

2.3 Ideal gas behaviour

As could be understood from the previous section there are some equations and law's that play an important role when using HYDRA (or any CFD code designed for compressible ideal gases) with a different working fluid. During this study they will also play an important role in the scaling process between the present conditions for water and air, see Chapter 4, Hydra setup. In this chapter the equations are presented together with short descriptions.

2.3.1 Equations of state

First of all we have the ideal gas law that states the relationship between pressure, density and temperature for ideal gases.

$$P = \rho RT \quad (2.16)$$

Where R is the specific gas constant calculated as the difference between the specific heat for constant pressure, c_p , and the specific heat for constant volume, c_v .

$$R = c_p - c_v \quad (2.17)$$

A relation between the internal energy and the temperature of an ideal gas can be described through the caloric equation of state.

$$e = c_v T \quad (2.18)$$

The speed of sound in an ideal gas can be described as

$$c = \sqrt{\gamma \frac{P}{\rho}} \quad (2.19)$$

or as

$$c = \sqrt{\gamma RT} \quad (2.20)$$

by substitution of P/ρ using the ideal gas equation. γ is the adiabatic index and determined by the ratio between c_p and c_v .

$$\gamma = \frac{c_p}{c_v} \quad (2.21)$$

The velocity in an ideal gas expressed through the sound speed and the Mach number becomes

$$u = Ma \cdot c \quad (2.22)$$

For closer descriptions of the equations above the reader is referred to Versteeg and Malalasekera [20] and White [21]

2.3.2 Sutherland's law

Another important equation is Sutherland's law which describes the relation between temperature and viscosity for an ideal gas, Sutherland [16]. Figure 2.2 displays the behaviour of air at STP conditions.

$$\mu = \mu_{ref0} \left(\frac{T}{T_{ref}} \right)^{3/2} \frac{T_{ref} + S_{suth}}{T + S_{suth}} \quad (2.23)$$

where

S_{suth} – Sutherland temperature in Kelvin

μ_{ref0} – Sutherland reference viscosity (present at the reference temperature) kg/ms

T – Actual temperature in Kelvin

T_{ref} – Temperature at which μ_{ref0} occurs

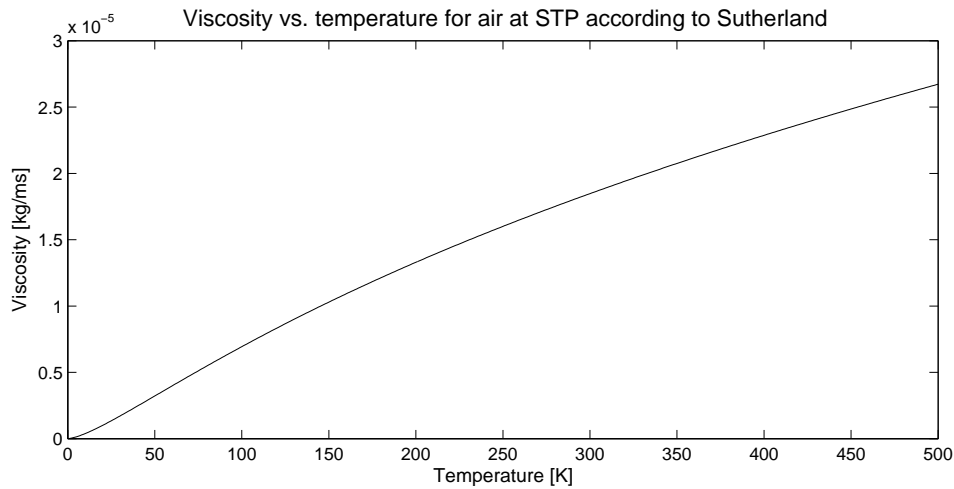


Figure 2.2: Viscosity vs. temperature for air at STP ($S_{suth} = 110.3$, $\mu_{ref0} = 1.79 \cdot 10^{-5}$, $T_{ref} = 288$).

2.3.3 Compressibility

When a fluid is subject to an increasing velocity the effects of compressibility are also increasing, i.e. the pressure coefficient will change. Equation (2.24), derived by Karman-Tsien, describes the effect an increasing Mach number has on the pressure coefficient. The result for an arbitrary case can be seen in Figure 2.3.

$$C_p = \frac{C_{p0}}{\sqrt{1 + Ma^2 + \frac{C_{p0}}{2} (1 - \sqrt{1 - Ma^2})}} \quad (2.24)$$

where

C_p – Compressible pressure coefficient

C_{p0} – Incompressible pressure coefficient

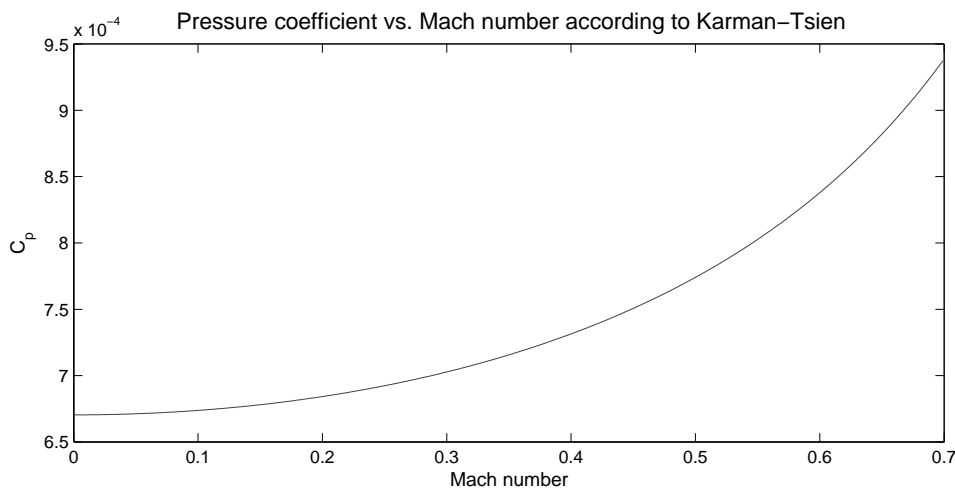


Figure 2.3: Pressure coefficient increases with Mach number.

2.4 RANS

To fully solve the Navier-Stokes equations, presented in Section 2.2, would require a mesh with cells fine enough to capture eddies of sizes down to around $10 \mu\text{m}$ within a domain big enough to capture the

largest eddies (ship scale). This could work for computations taking place within extraordinarily small domains but in most cases where the domains are designed to cover the flow around, e.g. a hull or an airplane it could lead to meshes with up to 10^{12} nodes to capture the whole range. Another problem is that the fastest events in a turbulent flow take place at frequencies down to 10 kHz which would require computational time steps as small as 100 μ s [20]. With the present technology this is not possible and even if it was it would not be economically defendable because of the huge amount of time and computer power it would demand. Luckily, in most of today's applications there is no need to observe the behaviour of the smallest eddies, it is more important how the mean values (inside one reasonable sized computational cell) of quantities such as pressure, velocity, stresses, etc. are affected by the turbulence.

One method that enables this important simplification is called Reynolds Averaged Navier-Stokes (RANS). This method is the main and most common one, used in both HYDRA and FLUENT and the one used exclusively in this study. A short explanation of how it works follows. For further studies see references [20] and [9].

To demonstrate the principle of RANS lets observe how it changes the momentum equation in the x direction, see Equation (2.5). By letting the flow field properties be represented by a mean and a fluctuation part (turbulent part) they change into

$$u = \bar{u} + \acute{u} \quad (2.25)$$

$$p = P + \acute{p} \quad (2.26)$$

$$\rho = \bar{\rho} \quad (2.27)$$

The density fluctuations can be neglected in flows where the velocity fluctuations lie within 5% of the mean velocity for speeds up to Mach number between 3 and 5 [20].

By substitution of u , p and ρ in Equation (2.5), Favre-averaging [20] the result and finally group all fluctuation terms together it transforms into Equation (2.28).

$$\frac{\partial(\rho u)}{\partial t} + \nabla \cdot (\rho u \mathbf{V}) = \frac{\partial P}{\partial x} + \nabla \cdot (\mu \nabla u) + \left[-\frac{\partial(\rho \overline{\acute{u}^2})}{\partial x} - \frac{\partial(\rho \overline{\acute{u}\acute{v}})}{\partial y} - \frac{\partial(\rho \overline{\acute{u}\acute{w}})}{\partial z} \right] + \rho f_x \quad (2.28)$$

By studying Equation (2.28) it is possible to see that this approximation give rise to further unknowns originating from the three fluctuation terms. They are commonly called Reynolds stresses.

$$\frac{\partial(\rho \overline{\acute{u}^2})}{\partial x} \quad (2.29)$$

$$\frac{\partial(\rho \overline{\acute{u}\acute{v}})}{\partial y} \quad (2.30)$$

$$\frac{\partial(\rho \overline{\acute{u}\acute{w}})}{\partial z} \quad (2.31)$$

In the same way as shown above Reynolds stresses also appears in the Momentum equations for the y and z directions and the Energy equation, giving rise to further unknowns. To be able to close the new equation system different types of so called turbulence models are used to as accurately as possible

predict the Reynolds stresses. There are many different types of turbulent models, some of them aimed to cover a broad spectrum of flows while others are more specific. The following section describes the two different models used in this study.

2.5 Turbulence models

As discussed in the previous section the Reynolds stresses have to be modelled since the total numbers of unknowns are higher than the total number of equations. In a 3-dimensional problem the Reynolds stress tensor contains six unknowns meaning that six equations are needed to close the problem. A common way to reduce the number of equations is to apply Boussinesq approximation, a method used for both of the models described in the following subsections.

The Boussinesq approximation is based on the assumption that the Reynolds stresses are proportional to the mean velocity gradient, see Equation (2.32). By using this approximation the six unknowns can be determined by two unknowns, μ_t and k , where μ_t is the turbulent viscosity and k is the turbulent kinetic energy.

$$-\rho \overline{u_i u_j} = \mu_t \left(\frac{\partial u_i}{\partial x_j} + \frac{\partial u_j}{\partial x_i} \right) - \frac{2}{3} \rho k \delta_{ij} \quad (2.32)$$

The number of equations needed to determine these two unknowns depends on what kind of model that is used, a zero, one, two or three equation model. Commonly for many of the models is that they use one additional equation to calculate μ_t from the turbulent length scale.

$$\mu_t = C_\nu u l \rho \quad (2.33)$$

As mentioned, in this study two turbulence models have been used/evaluated, they are the one equation model Spalart-Allmaras and the two equation model k- ω SST.

2.5.1 Spalart-Allmaras

Spalart-Allmaras is a one equation model developed specially for external flows and is widely used within the aerospace industry, including Rolls-Royce. It is also the most mature turbulence model in HYDRA. The model has to large extent been developed from empirical results and has proven to give more accurate results than some two equation models, mainly in flows typical for the aero industry [7].

The model consists of one equation resolving the turbulence viscosity, and in opposite to other one equation models the Spalart-Allmaras model does not include the second term, the turbulent kinetic energy. Further the model is one of the few one equation models that are local (if not the only one), meaning that the equation in one point does not depend on solutions from neighbouring points. The advantage is that a high local value of turbulence, normally caused by convection from upstream generated eddies, is avoided.

Spalart-Allmaras also includes a destruction term designed to dampening the fluctuations near the wall, which means that the flow can be modelled all the way down to the wall. Commonly models with this capability are called "Low Re" models, referring to the lower Reynolds number near the wall. For more information about Spalart-Allmaras see Spalart and Allmaras [15].

When using the Spalart-Allmaras model an initial turbulent viscosity has to be defined on the inlet boundary. See Sections 4.3 and 5.1 for more details.

2.5.2 k- ω SST

The k- ω SST model (where SST is short for Shear Stress Transport) has been built up from two previously well known models k- ω and k- ϵ . It has been developed to give more accurate and reliable solutions for a wider range of flows than the standard k- ω model [6]. This is achieved by a blending function where the standard k- ω model is used near the wall and a transformed k- ϵ model used in the far field. Thereby k- ω 's good near wall capabilities and k- ϵ 's desirable effects on the free stream are combined in the same model. k- ω SST is, like Spalart-Allmaras, also referred to as a "Low Re" model.

k- ω and k- ϵ are both two equation models that have been developed as a general purpose models, basically meaning that they are used for a wide range of purposes of which marine applications is one. A two equation model simply means that the turbulence is described by two equations, e.g. as with k- ω the k and ω equations. The advantages over a one equation model is that they allow the turbulent velocity and the turbulent length scale to be independently determined while the disadvantage simply being that two equations have to be solved, increasing the computational time

The turbulent viscosity, μ_t , in Equation (2.32) is defined by Equation (2.34) for the k- ω model and Equation (2.35) for the k- ϵ model. In both equations k describes the turbulent kinetic energy while ω in Equation (2.34) describes the specific dissipation rate and ϵ in Equation (2.35) the energy dissipation rate.

$$\mu_t = \rho \frac{k}{\omega} \quad (2.34)$$

$$\mu_t = C_v \rho \frac{k^2}{\epsilon} \quad (2.35)$$

In both HYDRA and FLUENT the k- ω SST model has to be defined by initial values for the turbulence intensity and viscosity ratio on the inlet boundary. See Sections 4.3 and 5.1 for more details.

2.6 Boundary layer and its modelling

The most important flow around the hull is the flow inside the boundary layer. It is inside this region where the most turbulence will be developed and that will control the viscous forces acting on the hull. A turbulent boundary layer could be split into two main parts, where the inner part, closest to the wall, can be divided into additionally three parts, see Figure 2.4. The outer region constitutes about 80% of the total boundary layer depth.

The reason to split the boundary layer into different parts is because that the physical behaviour of the flow near the wall is changing due to the rise in shear stress. The total shear stress in a turbulent flow consists of two parts, the viscous stresses and the turbulent stresses (Reynolds stresses). Equations (2.36) - (2.37) describes the shear stress distribution in a two dimensional boundary.

$$\tau_{xy} = \text{viscous} + \text{turbulent} \quad (2.36)$$

$$\tau_{xy} = \rho \nu \frac{\partial U_x}{\partial y} - \rho u_x u_y \quad (2.37)$$

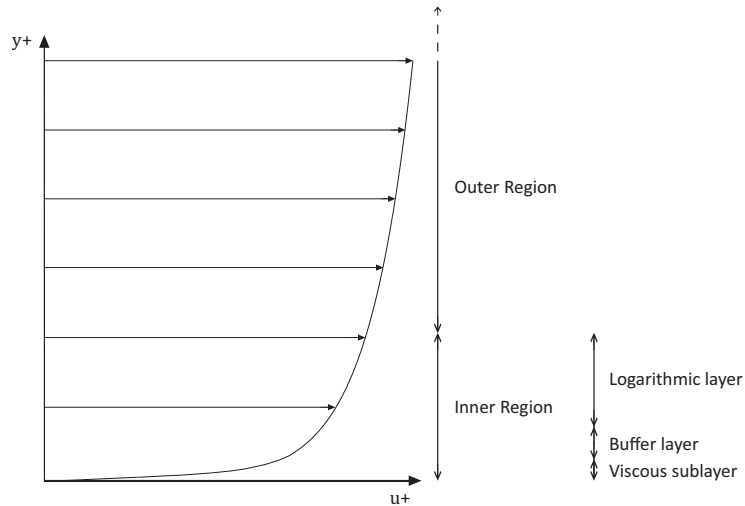


Figure 2.4: Boundary layer with its different parts, note that the scale is not accurate.

Close to the wall, in the viscous sublayer, the velocity fluctuations and the turbulent stresses are damped by the viscous stresses and rapidly vanish as the wall is approached. This means that in this region the flow will be strongly affected by viscous stresses, i.e. the flow is laminar. In the logarithmic layer, away from the wall, effects of viscous stresses are negligible and instead the turbulent stresses play a major role. Here the flow is considered fully turbulent. In the region between, the buffer layer, the importance of the two stresses is equal.

The thickness of the different layers depends on the geometry and the local Reynolds number. By experimental investigations nondimensional lengths have been determined for the different layers in the inner region. These lengths are found in Table 2.1. The nondimensional length, y^+ , is defined as

$$y^+ = \frac{yu_\tau}{\nu} \quad (2.38)$$

where u_τ is the friction velocity defined as

$$u_\tau = \sqrt{\frac{\tau}{\rho}} \quad (2.39)$$

y is the length in meters from the wall to the specified y^+ , ν the kinematic viscosity of the fluid, τ the wall shear stress and ρ the density of the fluid.

Table 2.1: Nondimensional lengths of the different layers in the inner region.

Viscous sublayer	$0 < y^+ < 5$
Buffer layer	$5 < y^+ < 30$
Logarithmic region	$30 < y^+ < 1000$

The fact that the shear stress changes so rapidly near the surface makes it hard to resolve the correct stresses near and far away from the surface with the same set of equations. To solve this problem, many CFD codes introduce a wall function to describe the flow closest to the wall.

2.6.1 Wall functions

There are different kinds of wall functions but their purpose is always the same, to adjust the velocity and turbulence properties (e.g. k and ω or the turbulent viscosity ratio) to follow the empirical models of the near wall region. In addition some models also make sure that the transition between the wall function and the turbulence model is smooth.

This is essentially done by applying new boundary conditions at the first grid points, supporting the turbulence model with the right flow conditions. Since the flow properties are changing significantly when approaching the wall they are represented by different empirical models dependent on the distance between the first grid point and the wall. Figure 2.5 shows the magnitude of a non-dimensionalised velocity u^+ through the three different regions in the inner boundary layer.

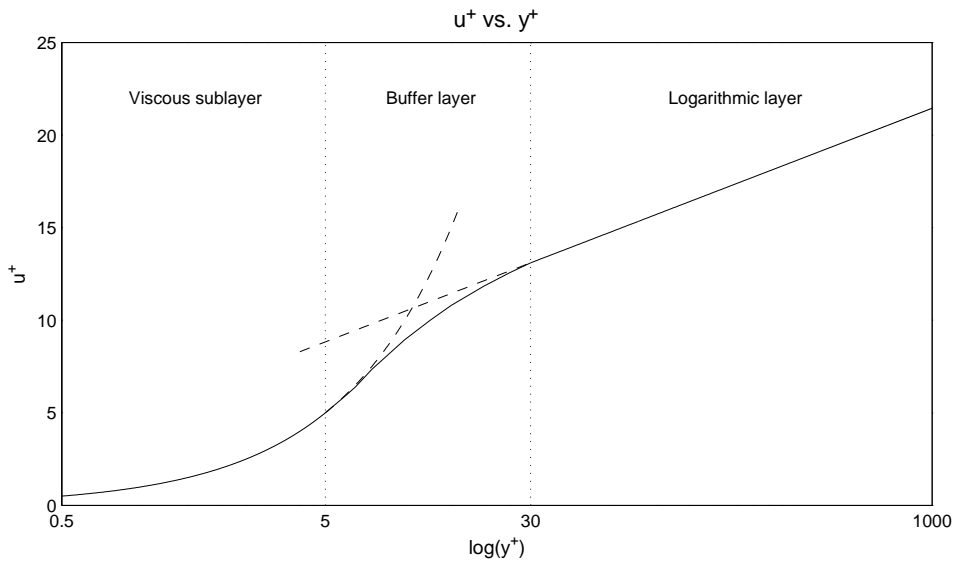


Figure 2.5: Nondimensional velocity profile in the boundary layer.

For y^+ between 1 and 5, in the viscous sublayer, the velocity is controlled by the viscous law, Equation (2.40).

$$U_x^+ = y^+ \quad (2.40)$$

Further out, in the logarithmic region for y^+ between 30 and 1000, the velocity profile is described by the logarithmic law, Equation (2.41).

$$U_n^+ = \frac{1}{\kappa} \ln y^+ + B \quad (2.41)$$

where

$$\kappa \approx 0.42$$

$$B \approx 5$$

Between those regions, in the buffer layer, which is a mix of the two surrounding layers there is no “law” for how the velocity behaves. Therefore it is important to make sure that the first grid point is located either within the viscous sub layer (y^+ below 5) or preferable [6] in the logarithmic region. When aiming

at the latter it should ideally be located somewhere at y^+ between 30 and 100 to give accurate solutions [4].

Because y^+ is a local property the nondimensional distance will vary over the surface, which might result in grid points located within the buffer layer. In this region, where neither the viscous nor the logarithmic law is valid the velocity will, most likely, be either under or over predicted.

To derive how the wall function treats the turbulent properties (e.g. k and ω) is a more complex task and will not be described here. For more information please see e.g. FLUENT manual [5].

Wall functions may not be accurate in many cases of flow since they are mainly defined from observations made on flows over a flat plate under zero pressure gradients. Hence some turbulence models like Spalart-Allmaras and $k-\omega$ SST, which are both described in Section 2.5, are designed to resolve the turbulence all the way down to y^+ around 1. Because of this they are commonly referred to as low-Re models. To do this they need a mesh fine enough to capture the viscous sublayer, i.e. grid points below $y^+=5$. When such a dense mesh resolution is not possible (or desirable) there is often a built in “switch” that will turn on the wall function when the first grid point is located outside a certain y^+ (often around $y^+=10$).

Also, since y^+ on the grid surface may vary significantly, HYDRA employs the Spalding blending function to produce a smooth transition from low Re Spalart-Allmaras into the log law wall function when the local y^+ becomes larger than 11. Similar technique is also used for $k-\omega$ SST.

As can be understood from this subsection the distance between the first grid points off the wall and the wall itself plays an important role on the result.

2.6.2 Slip wall function

Often when the boundary layer mesh is coarse and the first grid point off the wall (locally high Reynolds number) is placed somewhere in the logarithmic region a “slip” (velocity) is introduced on the wall, where there is physically a No slip condition. Without this slip the velocity gradient will be under predicted and there will be a small momentum loss near the wall which can be crucial for accurate shear stress prediction. Figure 2.6 shows the principle of the Slip wall condition.

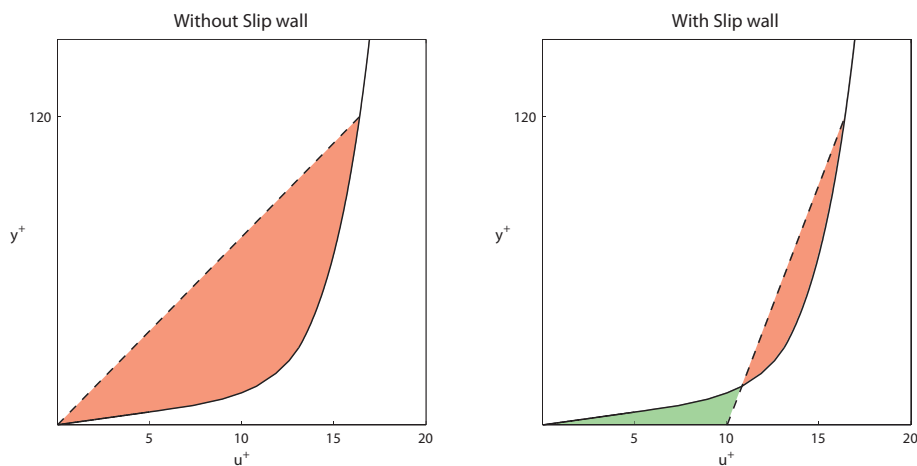


Figure 2.6: The effect of the Slip wall condition is illustrated for a case where the first grid point off the wall is located at y^+ of 120. The red areas indicate the momentum loss.

Benefits are that one can have a coarser mesh in the boundary layer region and still obtain a sufficient solution. Even though the iteration process in the solver might be slowed down by this, there is usually a total gain in calculation speed as a result of a decrease in Degrees of Freedom (DOF). Some other problems resulting from a dense boundary layer can also be avoided like e.g. skewed cells and high aspect ratios.

In FLUENT the Slip wall is controlled automatically (unless it is switched off) while in HYDRA it is always controlled manually.

2.7 Cell vs. Node based solver

FLUENT and HYDRA are using the mesh differently to calculate the flow. The most common way, and the one FLUENT is using, is to calculate and store the flow in the middle of the cell while HYDRA does it at the nodes, i.e. at the corners of each cell.

The DOF ratio (when going towards infinity) between a cell based and a node based solver is between 5-6 to 1 for a tetrahedral mesh since there are 5-6 cells to every node. For a prism mesh the ratio is 2-3 to 1 and for a structured mesh it is 1 to 1. As a trade off a cell based solver is expected to work around 5-6 times slower compared to a node based solver with the same tetrahedral mesh (or 2-3 times slower with a prism mesh).

This will also have effect in the boundary layer where the mesh commonly consists of either prism or rectangular cells. For both cases the distance from the middle of a cell to the wall is always half the distance than from its node, i.e. to capture the same flow in HYDRA as in FLUENT, the boundary layer mesh in HYDRA has to be twice as dense as the one in FLUENT. Referring to Subsection 2.6.1 one can understand that this is important to have in mind.

Since HYDRA is a Finite volume method (FVM) solver it requires a control volume around each node. The technique HYDRA uses to create this volume is called “Median Dual”. The technique enables the solver to reduce the total number of faces on the control volume. This is done by adding two or more surfaces together to shape one surface, i.e. one face. The motivation to reduce the number of faces is that it will reduce the number of equations solved during each iteration, since the flux through each face has to be calculated. To describe how this technique works a 2-dimensional example will be described below.

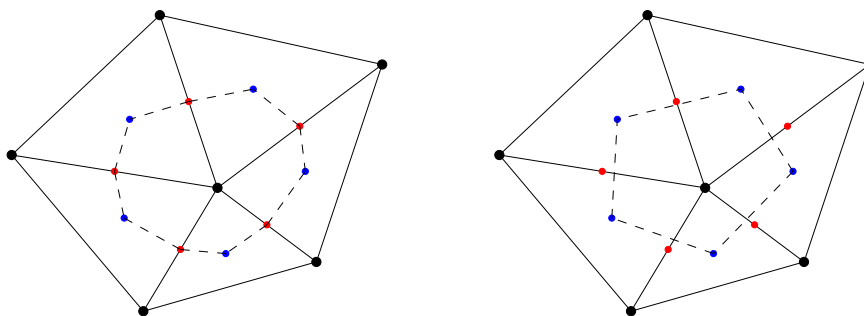


Figure 2.7: A control volume surrounding a node before and after applying “Median dual” technique.

Initially the control volume around a node is defined by joining the centroids and the edge midpoints on all surrounding cells and edges connecting the node, see left side of Figure 2.7. By applying the “Median dual” technique two edges, connecting centroid – midpoint – centroid, will be joined into one,

connecting centroid – centroid. In the above 2-dimensional problem the number of faces is reduced by two, however in a 3-dimensional problem the saving is considerably larger.

The downside with the “Median dual” technique is that the calculated fluxes do not have to be the ones that actually exist on the faces. This is because the flux is always calculated on the midpoint of the edge between two nodes, red dots in Figure 2.7, and the control volume faces, dashed lines, do not necessarily have to pass through these midpoints. Therefore the flux is either under or over estimated and this is why “Median dual” is an approximation.

By looking at Figure 2.7 it can be noted that the grid point in a node based solver, in opposite to a cell based solver, don't have to be in the middle of the control volume (compare blue dots with the black dot in the middle).

2.8 Coupled vs. Segregated solver

In a coupled solver all equations are solved simultaneously since they are collected in a matrix and the solution is attained through the inversion of it. This means that continuity, momentum and energy are updated at the same time, i.e. the solution is in phase. A coupled solver is generally preferred when there is a strong coupling between the flow parameters, e.g. in high speed flows.

In a segregated solver the equations are solved sequentially, i.e. the equations are segregated from each other. This means that, e.g., the pressure from the previous time step is used to solve the velocities in the present – the solution is out of phase.

2.9 HYDRA

HYDRA is mainly designed for high speed flows in ideal gases and because of that designed as a coupled solver which is considered suitable for those kinds of flows. This means that the code has to follow the equations of state and Sutherland's law at all time, see Section 2.3, and this puts constraints on which flows that are possible to simulate with the code, e.g. it is not possible to use water as the operating fluid. Further this means that all fluid is treated as compressible contrary to water which is considered incompressible. To avoid effects of compressibility it is important to make sure that the solution takes place at relatively low Mach numbers where even ideal gases are considered incompressible. To make this possible a feature called Low Mach Pre-Conditioning (LMNP) have been implemented in HYDRA, a closer description follows below in Subsection 2.9.4.

Since HYDRA is only aimed at solving fully submerged flows it has no capability for free surface solution. In those types of flow the lift forces overshadow the gravitational ones and therefore it is reasonable to completely exclude the gravity, something that has been done in HYDRA.

During the study all calculations are made using Steady-RANS calculations where the steady solution is performed by explicit time marching, basically meaning that a steady solution is reached through an unsteady calculation.

The following subsections are aimed at more advanced readers and explain more about the theory behind HYDRA computational scheme.

2.9.1 Flux evaluation

In HYDRA, fluxes are evaluated according to Equation (2.42) seen below. The equation consists of two parts, one inviscid (F^I) and one viscous part (F^V). It can be observed that the viscous part is nonlinear.

$$F(n, Q, \nabla Q) = F^I(n, Q) + F^V(n, Q, \nabla Q) \quad (2.42)$$

The decomposition originates from the mathematical system that forms the backbone of coupled flow solution, i.e. the Eigen system of the mass-momentum and energy equation. The method is acceptable for high speed flows where the effects of viscosity are insignificant (because of the high Reynolds numbers). Hence it is logical and easier to treat the two parts separately. The viscous part, which is more complex to evaluate, is treated as an add-on.

2.9.1.1 Inviscid flux

The way that the inviscid fluxes are calculated is built on the MUSCL (Monotonic Upstream-centered Scheme for Conservation Laws) scheme. This scheme is normally referred as a third order scheme but experiments have revealed that it does not perform any better than a second order scheme on unstructured grids. However, on structured meshes (which are mainly used in HYDRA), it outperforms the second order schemes.

The fluxes are calculated by a central difference method together with a numerical smoothing function, see Equation (2.43). The two first terms inside the bracket are components of the central difference part and the rest are terms for the smoothing function. The central difference is the average of two node values, and thus it is assumed the gradient is linear between the two nodes. The smoothing function is much more complex and includes smoothing between the multigrids and upwinding, however it will not be explained here. For a detailed description of the function see Moinier [14].

$$\phi_{ij}^I = \frac{1}{2} \left(\phi_{ij}(Q_i) + \phi_{ij}(Q_j) - \frac{1}{2}(1 - \kappa) |A_{ij}| (L_j(Q) - L_i(Q)) \right) \quad (2.43)$$

where

$\phi_{ij}(Q_i)$ – Inviscid flux at node i

$\phi_{ij}(Q_j)$ – Inviscid flux at node j

$|A_{ij}|$ – Modulus of inviscid flux Jacobian

$L_x(Q)$ – Undivided pseudo Laplacian at node x (i / j)

2.9.1.2 Viscous flux

In addition to the inviscid part, the viscous part is also dependent of the gradient and is calculated according to Equation (2.44), where the gradient on the faces is determined according to Equation (2.45).

$$\phi_{ij}^V = \mu \nabla Q_{ij} \quad (2.44)$$

$$\nabla Q_{ij} = \overline{\nabla Q_{ij}} - \delta \mathbf{s}_{ij} \left(\overline{\nabla Q_{ij}} \cdot \delta \mathbf{s}_{ij} - \frac{Q_i - Q_j}{|\mathbf{x}_i - \mathbf{x}_j|} \right) \quad (2.45)$$

The first part in Equation (2.45), $\overline{\nabla Q_{ij}}$, is a central differences of the gradients in node i and j , see Equation (2.46), where the gradients are calculated according to Green Gauss theorem.

$$\overline{\nabla Q_{ij}} = \frac{1}{2} (\nabla Q_i + \nabla Q_j) \quad (2.46)$$

$$\begin{bmatrix} \frac{\partial F_{con}}{\partial \rho} & \frac{\partial F_{con}}{\partial u} & \frac{\partial F_{con}}{\partial p} \\ \frac{\partial F_{mom}}{\partial \rho} & \frac{\partial F_{mom}}{\partial u} & \frac{\partial F_{mom}}{\partial p} \\ \frac{\partial F_{ene}}{\partial \rho} & \frac{\partial F_{ene}}{\partial u} & \frac{\partial F_{ene}}{\partial p} \end{bmatrix} \quad (2.49)$$

If the block Jacobi pre-conditioner is used the equations becomes more expensive to calculate, basically because additional terms are added. The reason to anyway include the pre-conditioner is to be able to take larger time steps without affecting the steady solution, i.e. each iteration will take longer time to calculate but fewer are needed to reach convergence. In the end this should contribute to faster convergence.

$$\Delta t = CFL \frac{V}{|\lambda_{max}|dA} \quad (2.50)$$

The common way to calculate the time step, Δt , is by Equation (2.50) in which the time step is determined by dividing the cell volume with the maximum Eigenvalue over all faces. Essentially these Eigenvalues are equal to $|u + c|$. When using the preconditioner the maximum time step is instead calculated by Equation (2.51), where the last term in the equation is the inverse of the matrix inside the block Jacobi matrix corresponding to the cell being calculated.

$$\Delta t = CFL \left[\frac{\partial F}{\partial Q} \right]^{-1} \quad (2.51)$$

2.9.4 Low Mach number pre-conditioning

As mentioned earlier there is a wish when using HYDRA for marine applications to ensure that the effect of compressibility is negligible, this means that the calculations has to take place at relatively low Mach numbers, preferably under 0.3. At those low Mach numbers a solver which is mainly designed for high speed flows may experience problems such as slow convergence and reduced accuracy. To cope with this, and to be able to resolve such kind of flows a special function have been implemented in HYDRA, namely the low Mach number preconditioning, further on called LMNP. Simply described the LMNP will magnify small velocity changes so that the pressure gets a chance to react on them.

The LMNP works by affecting the solvers pre-conditioner to perform in a slightly different way at low Mach numbers. A brief description of this pre-conditioner is found in the previous subsection.

To illustrate the basic idea behind the LMNP Equation (2.50) in Subsection 2.9.3, is rewritten into Equation (2.52), stated below. The only difference between them is that in the latter the actual Eigenvalue (λ), usually used in the most CFD codes, is inserted into the equation. From this equation it can be seen that if the convective speed or the sound speed is increased the time step, Δt , will decrease. It is important to remember that HYDRA does not use this method but the same problems that occur when using this method will also be present when using the pre-conditioner.

$$\Delta t = \frac{V}{\phi(|u_n| + c)dA} \quad (2.52)$$

where

- V – Cell volume
- $|u_n|$ – Absolute value of convective speed at the face
- c – Sound speed

Mainly there are two problems when the convective speed decreases. The first problem appears when the speed drops below Mach number 0.3 air is considered to be considerably less compressible. This means that the density becomes more and more constant, i.e. the rate of change is decreasing. Observing Equation (2.53), describing the speed of sound in an ideal gas it can be seen that when $\partial\rho$ becomes small the speed of sound becomes large. A large value for the sound speed in Equation (2.52), above, will mean that the time step will go towards zero, i.e. the convergence time will increase.

$$c^2 = \frac{\partial P}{\partial \rho} \quad (2.53)$$

The second problem is also related to the sound speed and the decreasing compressibility. The fact that the sound speed gets larger with the decreasing convective speed will eventually result in that the relationship between velocity and relative pressure can no longer be sustained. This is because that even if the speeds within the flow are large compared to each other the solver will not be able to see any difference between them in relationship to the sound speed, e.g. if dividing 0.01 and 0.001 with 10,000 both results will almost be zero even if the ratio between them is 10. This will in the end result in a solution with poor accuracy. At higher Mach numbers this is obviously not a problem because the relative speeds are higher compared to the sound speed.

To get rid of the problems mentioned above the LMNP is altering the speed of sound in the Eigenvalues. Instead of using the actual sound speed it is replaced with a variable θ , which can take any value between the convective speed and the sound speed.

The LMNP is implemented when the speed drops below Mach number 0.25. At this point θ is equal to c , the sound speed. As the Mach number decreases towards zero θ decreases towards the convective speed, u . The relationship can be seen below.

$$Ma \rightarrow 0.00 \Rightarrow \theta \rightarrow u$$

$$Ma \rightarrow 0.25 \Rightarrow \theta \rightarrow c$$

Over all the LMNP will speed up the convergence and give a better result at low Mach numbers. This is mainly because the relationship between pressure and velocity can be resolved more accurate. On the other hand, if the function is used on high Mach numbers the convergence rate will be the same but the calculation time higher because there are additional equations to calculate.

In addition the LMNP also reduces the numerical smoothing term to give even better accuracy at low Mach numbers. For more information about the LMNP the reader is referred to Moinier [14].

2.10 FLUENT

FLUENT is one of the most well known CFD codes to date and it is developed as a general-purpose code compatible with both compressible and incompressible flows. It offers both a coupled and segregated solver as well as free surface capabilities. In this study the segregated solver was used. In the following subsections the used settings and some theory behind them are explained and described.

2.10.1 Pressure – Velocity coupling

When running FLUENT as a segregated pressure based solver there are four options to choose between when deciding how the coupling between pressure and velocity should be sustained. The four pressure – velocity algorithms are SIMPLE, SIMPLEC, PISO and FSM. For calculations at steady state the two main options remaining are SIMPLE and SIMPLEC. The main difference between them is that SIMPLEC converges faster for laminar flow without any turbulence, the trade off is that in highly turbulent flows it has tendencies of being unstable [1] [6]. In cases involving turbulence the convergence rate is similar for the two algorithms. Further, the SIMPLEC algorithm needs an additional input in form of skewness correction. For these reason the SIMPLE algorithm is used in this study.

The SIMPLE scheme in segregated mode works as follows. At each iteration the solver begins with updating all fluid properties, e.g. density and viscosity, based on the current solution. Then the velocities are solved one after another in each cell through the momentum equation, (2.26).

To obtain the related pressure a pressure correction equation is used, see Equation (2.55). This equation is derived from the continuity and the momentum equations. Thereafter are the mass fluxes, pressure and the velocity field updated to agree with the corrected pressure.

As a lasts step the turbulence is solved by the turbulence model and the solver checks if the convergence limit has been reached (if there is one). If not, the solver starts a new iteration by updating the fluid properties.

Momentum equation in x-direction

$$a_p u = \sum_{nb} a_{nb} u_{nb} + \sum p_f A_f \hat{i} + S \quad (2.54)$$

where

a_p – Linearised coefficient at present grid point

a_{nb} – Linearised coefficient at neighbouring grid point

u – Velocity in x direction

P_f – Pressure at face

A_f – Area of face

\hat{i} – Surface vector

S – Source term

Pressure correction equation (Continuity equation)

$$\sum_f^{N_{faces}} J_f A_f = 0 \quad (2.55)$$

where

J_f – Mass flux through face

A_f – Face area

2.10.2 Gradient

In FLUENT 12.0.16 there are three options to chose between when calculating the gradient, they are Green-Gauss cell and node based and the Least-squares (cell based) method. According to FLUENT [6] the Least-squares method performs equivalent to the node based gradient but is less expensive to compute. Both these methods (the node based and the least square) are superior the Green-Gauss cell based method.

The Least-squares method in FLUENT uses an unweighted approach, i.e. the distances to the neighbouring cells are not counted for. This means that a neighbouring cell located far away has the same influence as a cell located right next to the grid point. The result is that the gradient is under estimated on highly stretched meshes in presence of surface curvature. One report has shown that the gradient in the boundary layer can be up to one order of magnitude wrong under these circumstances [13]. As can be seen in Figure 3.4, Subsection 3.4.3, the cells close to the hull are highly stretched, i.e. the Least-square method would not be suitable. Therefore the Green-Gauss node based method was chosen.

The Green-Gauss node based method is calculated according to Equation (2.56) and (2.57).

$$\nabla\phi = \frac{1}{V} \sum_f \overline{\phi}_f \vec{A}_f \quad (2.56)$$

where

V – Number of faces on cell

\vec{A}_f – Surface vector

$\overline{\phi}_f$ – Mean value of ϕ_f

The mean value on each face is calculated as follows

$$\overline{\phi}_f = \frac{1}{N_f} \sum_n^{N_f} \overline{\phi}_n \quad (2.57)$$

where

N_f – Number of nodes on the face

$\overline{\phi}_n$ – Node value

The node values, $\overline{\phi}_n$, are calculated by taking the weighted average of the cell values surrounding the nodes.

2.10.3 Upwind scheme

To calculate the face values of each cell a Second order upwind scheme has been used. The scheme is designed to only use upstream node values to calculate the downstream cell face(s), i.e. it only uses cells from where the flow is streaming. By doing this numerical faults resulting from strong convection are avoided, on the other hand the equation is no longer bounded. The equation is stated below.

$$\phi_f = \phi_i + \nabla\phi_{i-1} \cdot \vec{r} \quad (2.58)$$

where

- ϕ_i – Grid point value
- $\nabla\phi_{i-1}$ – Gradient in the previous grid point
- \vec{r} – Distance to the face from the grid point

The gradient is calculated according to Green-Gauss theorem, discussed in the previous subsection.

2.10.4 Under relaxation factors

From one calculation to another the calculated values, for example pressure and density, can change significantly. This could be an effect of numerical error or just a bad initial guess. To make the calculations more stable and converge towards the right solution so called under relaxation factors are used. The idea is that the new value depends on the old and the new one, see Equation (2.59).

$$\phi_{new} = \phi_{old} + \alpha \cdot \Delta\phi \quad (2.59)$$

where

- ϕ_{new} – New value
- ϕ_{old} – Previous value
- α – Under relaxation factor
- $\Delta\phi = \phi_{new} - \phi_{old}$

By choosing a lower under relaxation factor the new value has less influence and is not as sensitive to extreme values. In all cases the default values have been used for the under relaxation factors.

2.10.5 Multigrid

In FLUENT an algebraic multigrid (AMG) is used as default. As the name tells us this method is algebraic and therefore no physical grids have to be created or stored. FLUENT themselves states that this method is “particularly attractive for use on unstructured meshes” because all coarse level equations are generated without use of any geometry or rediscretisation [5].

3 Test cases

Two different hulls have been subject for testing in this study, their differences can be found both in shape and operating conditions. They are both mathematically defined parabolic ship forms commonly known as Wigley hulls, characterised by their simple symmetrical shape. By using simple geometries it is possible to minimize the complex flows that can appear around appendages such as propellers, rudders, shafts etc, which can be hard to capture. Both hulls have been subjects to rigorously experimental testing in the past and lots of recorded data is available, this makes them perfect for comparison studies.

The first one, Wigley I, appeared in Journée [10] where four different Wigley hulls were tested, named Wigley 1 to 4. In this study the second hull, Wigley 2, has been used, here named Wigley I. The main reason to why this hull was chosen was the fact that it had the most curvature, i.e. the hull that theoretical should create most turbulence. For the experimental results from Journée [10] see Subsection 6.1.1.

The second one, Wigley II appears in Ju [11] where the total viscous resistance component of the hull was extracted through a “wake survey” method, which where proven to give good results. Therefore reliable data for comparison are available. For an overview of the experimental results from Ju [11] see Subsection 6.1.2.

The following sections presents the main particulars, mathematical formula and operating conditions for Wigley I and II.

3.1 Mathematical definition and main particulars

Both hulls can be described by the following mathematical formula found in Ju [11] and Journée [10].

$$y = (1 - z^2)(1 - x^2)(1 + \theta x^2) + \beta z^2(1 - z^8)(1 - x^4)^4 \quad (3.1)$$

where

x – Longitudinal value, positive forwards (-1 – 1)

y – Lateral value, positive to port side (-0.5 – 0.5)

z – Vertical value, positive downwards (0 – 1)

For Wigley I the constants θ and β are 0.2 and 1 respectively, while for Wigley II they are both set to zero, making the equation describe a more slender and less pronounced hull. By multiplying x , y and z with $LPP/2$, $B/2$ and d respectively, the hulls gets dimensions. The main particulars of the hulls are found in Table 3.1.

Table 3.1: Main particulars for Wigley I and II.

	Wigley I	Wigley II
LPP [m]	3.0000	3.0480
B [m]	0.6000	0.1524
d [m]	0.1875	0.1905
S [m ²]	1.9560	1.3810
Cb	0.5610	0.4444

Figure 3.1 shows the body plans for Wigley I and Wigley II. For the full lines drawings see Appendix C.

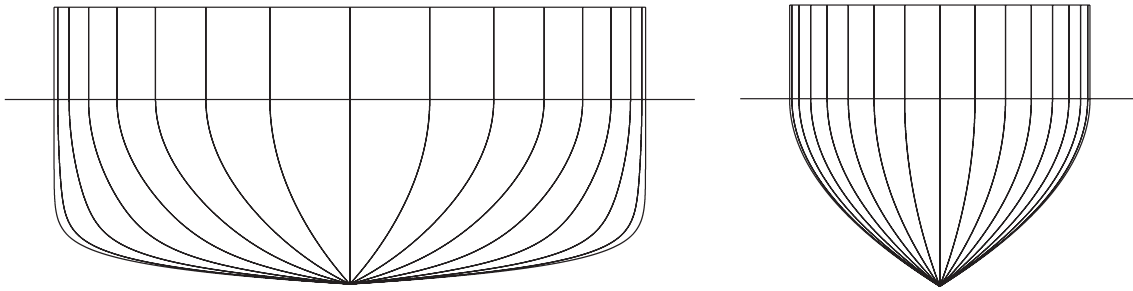


Figure 3.1: Body plans of Wigley I (left) and Wigley II (right), both in the same scale.

3.2 Operating conditions

All calculations were performed to match the conditions present during the experimental testing, see Ju [11] and Journée [10]. For the Wigley I hull the conditions were not found so a rough estimate had to be made. But considering that the method used to subtract the wave resistance for Wigley I, described later in Subsection 6.1.1 and Appendix A, contains a substantial fault marginal the possible deviations from the present conditions are estimated to be within that margin. The testing of the Wigley II hull was performed in fresh water at a temperature of 18.3°C, the conditions were interpolated between ones representing 18 and 19°C found at ThermExcel [18]. The conditions used in both cases are tabulated in Table 3.2.

Table 3.2: Operating conditions.

	Wigley I	Wigley II
g [m/s ²]	9.820	9.803*
μ [Ns/m ²]	0.001000	0.001046
ρ [kg/m ³]	998.000	998.623
V [m/s]	1.086	1.312 – 1.750
Fn	0.20	0.24 – 0.32
Re	3,250,000	3,818,000 – 5,090,000

* The gravitational acceleration force is expected to be the same as in Chicago since the cities are located relatively close to each other and also at about the same height over the sea.

3.3 Geometry generation

The geometries were created from their mathematical formula, Equation (3.1), by an algorithm written in Fortran¹ code. Basically the code generates a surface from a grid of points distributed in a Cartesian coordinate system. 1000 points in the horizontal direction and 65 in the vertical give a total number of 65 000 points or coordinates that together defines the hull. From the coordinates a surface was created according to the structure of the STL² format. Simply explained the surface is created with an algorithm through which three neighbouring points where linked together, forming small triangles. Each triangle then represents a small surface and together they form the hull. The code can be seen in Appendix F.

¹ A general-purpose programming language especially suited for numeric computation and scientific computing.

² An STL file is a triangular representation of a 3D surface geometry.

3.4 Meshing

For both Wigley I and II different meshes with a mix of structured and unstructured cells were created, following from the procedure described in Øye [22]. For Wigley II an additional “high quality” structured mesh was created for further validation with the motivation that a structured mesh is considered to give less dissipation and improve the gradient since the cells are aligned with the flow. Another outcome from a structured mesh is that it will give a similar number of DOF in HYDRA and FLUENT, see Section 2.7. For an unstructured mesh the DOF are to favour for FLUENT as described in Section 2.7 – Cell vs. Node based solver.

The mixed meshes were created in a number of versions for each hull with the only difference being the resolution of the boundary layer and as a direct consequence of that the DOF. For the Structured mesh two versions were created, also with differences in the boundary layer. The calculations for the boundary layer properties, such as thickness and the first cell size (the one nearest the hull surface), are described in Appendix A.

All meshes were created in GAMBIT and exported to msh¹ files, a format compatible with both FLUENT and HYDRA. The following chapters describes and tabulates the properties of the meshes, first out is Wigley I followed by Wigley II.

Note that the main interest with the mesh dependency evaluation were to investigate y^+ and wall function differences between HYDRA and FLUENT. Therefore no substantial work was put into make sure that mesh independency where reached. It could be argued that more work should have been put into reaching mesh independency but a denser mesh would have led to longer calculation and setup times. Further it has never been an intention to investigate form effects in this study, therefore the fact that the hulls are meshed slightly different does not constitute a problem.

3.4.1 Wigley I

The mesh is contained within one large rectangle shaped volume which is divided into two parts, one inner and one outer. The outer volume itself was then divided into 11 smaller volumes to enable the mesh in those regions to be structured. The whole domain extends from the inner volume and ends 4.5 LPP downstream, 2.3 LPP upstream, 3 LPP sideways and 1 LPP downwards from the hull. A large domain makes sure that the boundary conditions will have minimal effect on the solution. The inner volume extends 0.35m from the hulls “largest” coordinates in all four directions forming a smaller rectangle surrounding the hull surface. Figure 3.2 shows domain and its divisions.

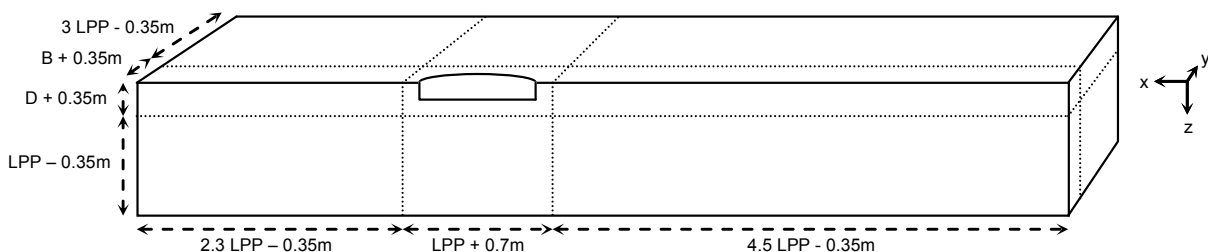


Figure 3.2: Division of control volume for Wigley I and II “mixed meshes”.

¹ Generic mesh file

On the hull's surface the mesh consists of triangular faces with a spacing of 0.01 m. To achieve a denser mesh at the hulls most curved areas a size function has been defined along a line that follows the hull on a depth of 0.1275 m from 0.2 LPP behind the bow to 0.8 LPP m from the aft. It lets the cell size propagate from 0.005 to 0.03 m with a growth rate of 1.1 and it affects both the mesh on the hulls surface and one in the inner volume.

Within the inner volume the mesh consists of tetrahedral and prism cells where the prism ones are exclusively situated in the boundary layer. The cell size is controlled by the volumes surrounding faces and lines and is increased further away from the hull. All surfaces facing the outer volume were meshed structurally with a spacing of 0.06 m forcing a structured transition between the inner and outer volumes, the ones facing the symmetry planes are of triangular type. By letting the inner volume, surrounding the hull, be meshed unstructured with tetrahedral and prism cells the meshing process becomes much simpler for cases where abrupt changes in the geometry occurs. For example near most appendages on a ship hull.

As mentioned the outer volume consist of a structured mesh, and in the same way as the inner volume the mesh becomes coarser further away from the ship, controlled by the surrounding lines and the adjacent surfaces from the inner volume. The cell size extends from 0.06^3 to around 0.3^3 m^3 . A structured mesh in this region where the geometry is constituted of rectangles enables a considerably faster meshing process.

For Wigley I six different meshes with six different versions of the boundary layer were created and they are summarised in Table 3.3 below and Table 3.5 found on page 30. The spacing was chosen by simply matching the desired height of the first cell, Δy , to a specific y^+ . Note that the thickness of the boundary layer, δ , varies slightly between the different meshes. This is because the same growth rate, 1.2, has been used in all cases and the thickness of the boundary was then determined by the number of "layers" it took to pass the calculated reference value for δ (52.9 mm). For a closer look of how the distances to the different y^+ and δ was calculated see Appendix A.

Table 3.3: Wigley I boundary layer properties.

	y^+ (FLUENT/HYDRA)					
	0.5/1	5/10	15/30	30/60	60/120	120/240
δ [mm]	0.060	0.055	0.052	0.058	0.061	0.058
Layers	34	21	15	12	9	6
Δy [mm]	0.024	0.243	0.728	1.457	2.913	5.827

3.4.2 Wigley II

The Wigley II hull was meshed in the same manner as Wigley I with the same ratio between LPP and the domain size, the inner volume was also shaped in the same way, i.e. a rectangle formed 0.35m from the hulls "outer" coordinates. See Figure 3.2 in previous subsection.

Wigley II does not have such a pronounced shoulder as Wigley I and consequently there were no reason to have a size function covering those regions. For Wigley II the critical areas were instead its cusp angles at the bow and stern. Therefore a size function was used on the hulls forward, aft and lower edge forcing the cells to propagate from a spacing of 0.008 m to 0.06 m with a growth rate of 1.1. To achieve a denser mesh in the regions closest to the hull and a smooth transition towards the outer volume a second size

functions was used, this one with its origin in a rectangular shaped volume formed to wrap the hull and its boundary layer. It made the cell spacing propagate from 0.012 m to 0.06 m with a growth rate of 1.07.

Nine different versions of the mesh were created to enable more accurate comparison between HYDRA and FLUENT, by using different meshes to achieve the same y^+ in the two codes. For a discussion on mesh interpretation see Section 2.7, Cell vs. Node based solver. The different versions are shown in Table 3.6 (found on page 30) and Table 3.4. The boundary layer thickness, δ , and the distances to various y^+ were calculated in the same way as for Wigley I (see Appendix A). δ was estimated to 51.7 mm.

Table 3.4: Wigley II boundary layer properties.

	y^+ (FLUENT/HYDRA)								
	0.5/1	1/2	2/4	4/8	7.5/15	15/30	30/60	60/120	120/240
δ [mm]	58,970	56,770	53,870	51,870	55,630	52,120	57,760	61,860	61,560
Layers	35	31	27	23	20	16	13	10	7
Δy [mm]	0.020	0.040	0.079	0.159	0.298	0.596	1.191	2.383	4.766

Table 3.5: Mesh properties for Wigley I.

Description		y ⁺ (FLUENT/HYDRA)											
Type	Location	0.5/1	5/10	15/30	30/60	60/120	120/240	0.5/1	5/10	15/30	30/60	60/120	120/240
Hexahedral	Outer volume	92,502	92,502	92,502	92,502	92,502	92,502	92,502	92,502	92,502	92,502	92,502	92,502
Pyramid	Intersection outer/inner	1,438	1,438	1,438	1,438	1,438	1,438	1,438	1,438	1,438	1,438	1,438	1,438
Tetrahedral	Inner volume	346,754	354,011	358,841	349,963	344,323	349,480	346,754	354,011	358,841	349,963	344,323	349,480
Prisms	Boundary layer	398,208	245,952	175,680	140,544	105,408	70,272	398,208	245,952	175,680	140,544	105,408	70,272
Tot. cells	All volumes	838,902	693,903	628,461	584,447	543,671	513,692	838,902	693,903	628,461	584,447	543,671	513,692
Nodes	All volumes	367,547	290,916	255,780	236,310	217,370	200,271	367,547	290,916	255,780	236,310	217,370	200,271
Cells/nodes	-	2.28	2.39	2.46	2.47	2.50	2.56	2.28	2.39	2.46	2.47	2.50	2.56

Table 3.6: Mesh properties for Wigley II.

Description		y ⁺ (FLUENT/HYDRA)																		
Type	Location	0.5/1	1/2	2/4	4/8	7.5/15	15/30	30/60	60/120	120/240	0.5/1	1/2	2/4	4/8	7.5/15	15/30	30/60	60/120	120/240	
Hexahedral	Outer volume	81,450	81,450	81,450	81,450	81,450	81,450	81,450	81,450	81,450	81,450	81,450	81,450	81,450	81,450	81,450	81,450	81,450	81,450	81,450
Pyramid	Intersection outer/inner	1,198	1,198	1,198	1,198	1,198	1,198	1,198	1,198	1,198	1,198	1,198	1,198	1,198	1,198	1,198	1,198	1,198	1,198	1,198
Tetrahedral	Inner volume	893,772	903,987	915,958	924,126	906,977	924,751	897,845	879,833	881,783	893,772	903,987	915,958	924,126	906,977	924,751	897,845	879,833	881,783	881,783
Prisms	Boundary layer	388,220	343,852	299,484	255,116	221,840	177,472	144,196	110,920	77,644	388,220	343,852	299,484	255,116	221,840	177,472	144,196	110,920	77,644	77,644
Tot. cells	All volumes	1,364,640	1,330,487	1,298,090	1,261,890	1,211,465	1,184,871	1,124,689	1,073,401	1,042,075	1,364,640	1,330,487	1,298,090	1,261,890	1,211,465	1,184,871	1,124,689	1,073,401	1,042,075	1,042,075
Nodes	All volumes	448,223	426,776	405,421	383,531	363,100	342,835	320,831	300,190	283,043	448,223	426,776	405,421	383,531	363,100	342,835	320,831	300,190	283,043	283,043
Cells/nodes	-	3.04	3.12	3.20	3.29	3.34	3.46	3.51	3.58	3.68	3.04	3.12	3.20	3.29	3.34	3.46	3.51	3.58	3.68	3.68

3.4.3 Wigley II structured

The structured mesh is contained within a domain of the same size and shape as for the previous Wigley II meshes, but to enable an entirely structured mesh the volume had to be divided in a different way. Instead of using an outer and inner volume it has been divided into six parts as seen in Figure 3.3 below.

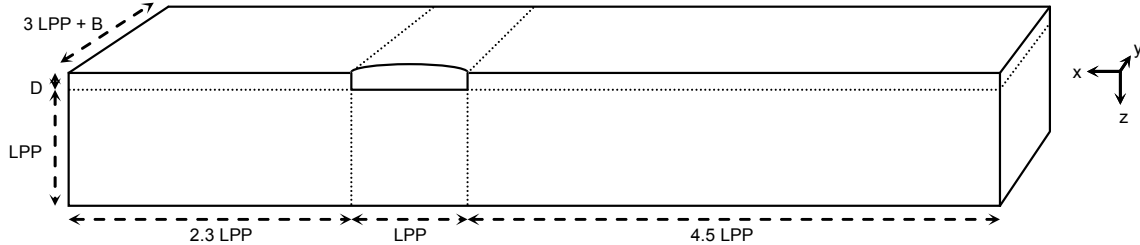


Figure 3.3: Division of control volume for Wigley II structured mesh.

The cell sizing in each of the volumes are defined by the volume’s surrounding edges, making the mesh grow denser closer to the hull. All edges in positive x-direction in front of the hull are meshed with a successive ratio of 1.06 with a total of 77 points. For edges alongside the hull in the same direction 150 points are distributed through a bi-exponential scheme with a ratio of 0.75, concentrating the mesh around the hulls bow and aft. The edges downstream of the hull, in the negative x-direction, have 103 points each spread by a successive ratio of 1.05. Along edges in the z-direction the first 50 points, reaching from the “surface” to the bottom of the hull, are distributed evenly, followed by 52 points distributed with a successive ratio of 1.08. All edges along the y-direction are each meshed with 100 points, where the first ones being affected by the boundary layer, applied to all of the symmetry surfaces, and the following by a first length scheme with start size of 0.012 m.

Since boundary layer was applied to the whole symmetry plane the sharp cells that appeared from Wigley II’s cusp bow and stern in the mixed mesh were avoided. It also resulted in a considerably higher resolution both upstream and downstream where the latter will have a positive effect for the wake prediction. Figure 3.4 highlights the benefits with the structured mesh compared to the mixed mesh for Wigley II.

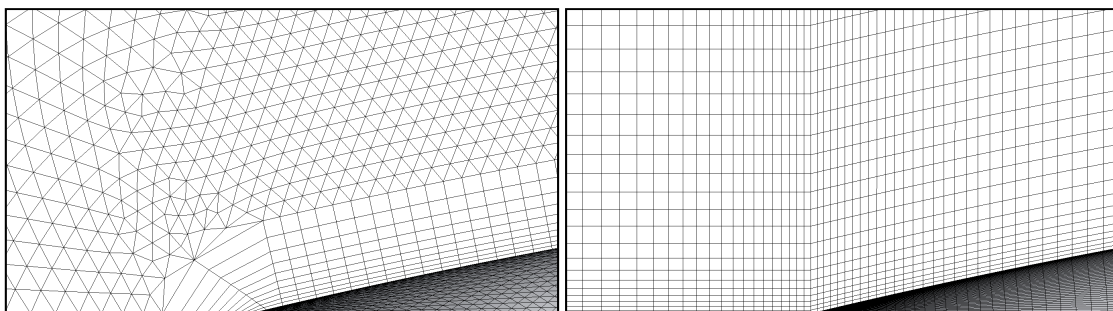


Figure 3.4: Wigley II Mixed vs. Structured mesh around hull bow, looking down at the xy-plane.

For this structured mesh type two different versions were created, again with the differences following from the boundary layer. They were made to Mach y^+ of 1 and 120 in HYDRA and at the same time 0.5 and 60 in FLUENT. How the boundary layers were distributed can be seen by looking in columns “0.5/1” and “60/120” in Table 3.4 above. Both of the meshes, that consist entirely of hexahedral cells, have a total number of 3,366,000 cells and 3,443,393 nodes, giving a node to cell ration of 0.98. This means that the DOF are almost the same in HYDRA and FLUENT, as discussed in Section 2.7.

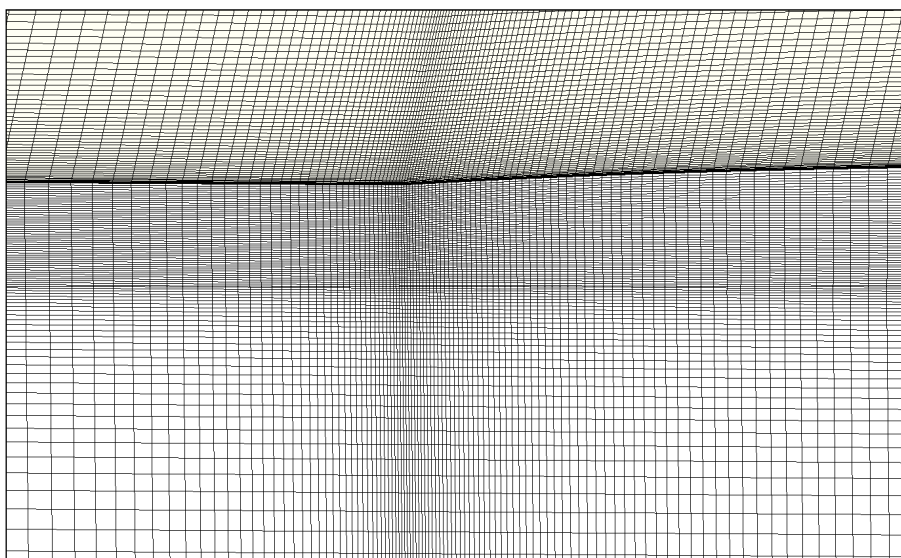
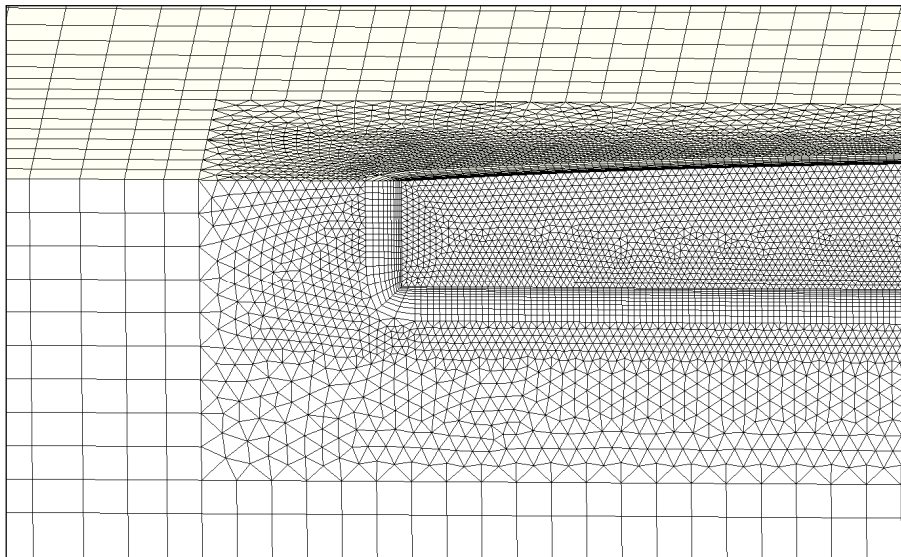
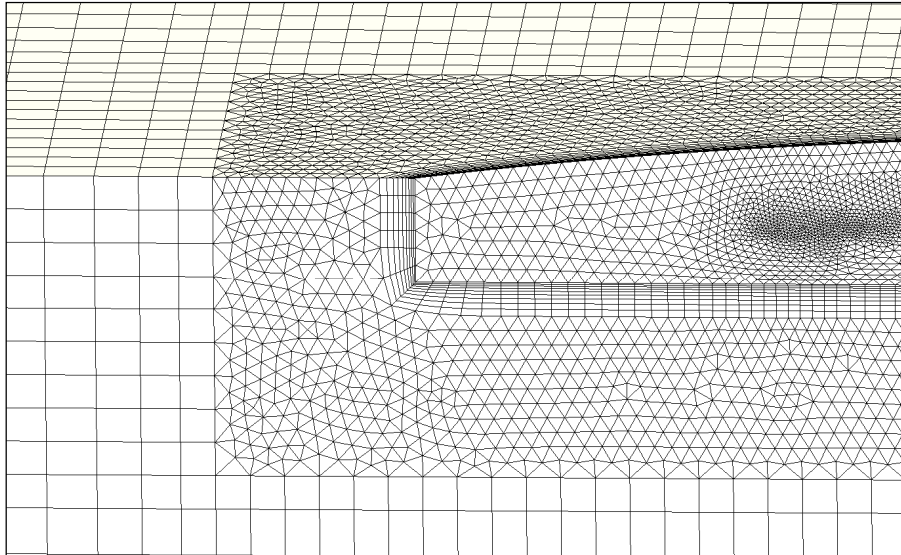


Figure 3.5 A-C: Mesh concentration around the bow. From the top: Wigley I mixed, Wigley II mixed and Wigley II structured, all with y^+ at 120.

4 Hydra setup

Throughout this study HYDRA 6.2.5 has been used, the code has been executed on a UNIX system and all calculations have been performed with double precision.

4.1 Similarity

Since, as learned from previous chapters, HYDRA is designed for high speed flows in ideal gases and there is no possibility to use water as the operating fluid all operating data between the test cases, see Chapter 2, and the input into HYDRA has to be “scaled”. In this study HYDRA can be seen as a wind tunnel in which applications for water is tested.

All scaling was done with respect to the Reynolds number, contrary to many cases in the marine industry where the Froude number is considered since it is the only parameter that will scale the waves correct. Consider the equation for the Froude number below

$$Fn = \frac{U}{\sqrt{Lg}} \quad (4.1)$$

In HYDRA since there is no gravity term the Froude number will have no meaning, the only times when the Froude number had to be taken into account was when the test case velocities where determined (they all have to match the given Froude numbers).

For the scaling to be correct the Reynolds number has to be constant between the different test cases and the CFD calculations, this is done by altering the operation conditions. By conserving the Reynolds number, in theory, the flow in the test cases and the CFD calculations will behave exactly the same. The Reynolds number is defined as

$$Re = \frac{\rho UL}{\mu} \quad (4.2)$$

where ρ is the density, U the freestream velocity, L the length and μ the dynamic viscosity.

To deal with the fact that HYDRA treats the fluid as compressible and to be able to compare results with solvers who can deal with incompressible flow the calculations in HYDRA has to be done at a low Mach number, preferably under 0.3 where the air is considered to behave incompressible [3]. According to previous experience, Moinier [14], HYDRA will run stable down to Mach numbers around 10^{-6} , i.e. calculations should ideally be made at Mach numbers between 10^{-6} and 0.3.

Since the operating velocities of the Wigley hulls are relatively low it is not possible to conserve the Reynolds number and at the same time stay within the preferred Mach number span by only changing the input values from "standard" properties for water to “standard” properties for air and then “scale” the velocity to make up for the difference. To preserve the Reynolds number and still let HYDRA run between Mach number 10^{-6} and 0.3 either the density, viscosity or the length of the hull also has to be scaled. If the length were to be scaled it would results in a larger mesh and through that slower calculations, therefore it is preferred to scale either the density or the viscosity.

If the temperature span in the solution differs too much from the input temperature we have a problem since the viscosity/temperature relation looks completely different for an ideal gas than for a liquid.

While the viscosity for a gas increases, see Figure 2.2 in Subsection 2.3.2, with temperature it decreases for a liquid [8]. I.e. this could result in faults when a flow in water is being represented in air.

The scaling can be done in a few different ways of which two are described in the following section.

4.2 Scaling of input values

All calculations in HYDRA are made in dimensionless form, whether the nondimensionalisation is done before or after the data is fed into HYDRA is of choice to the user. There are three different ways to feed in your input data, SI, STP, and STP2 the ones used in this report are SI and STP2. The reason for using two different ways was to validate whether the scaling was done in the correct way, later in the study only one of the “modes” was used.

In SI mode HYDRA interprets the input as dimensional data and performs a nondimensionalisation by dividing with its own set of reference values. STP2 lets the users specify their own reference values and perform the nondimensionalisation themselves before feeding the data to HYDRA.

Whether SI or STP2 is used the nondimensionalisation occurs (or as for STP2 - has to occur) as follows, note that the nondimensional values are denoted with a “*” in difference to HYDRA [17] where the dimensional “start” values are denoted in that way. This is to follow a convention used in most textbooks.

$$\rho^* = \rho_{input} / \rho_{ref}$$

$$P^* = P_{input} / P_{ref}$$

$$T^* = T_{input} / T_{ref}$$

$$U^* = U_{input} / U_{ref}$$

$$\mu^* = \mu_{ref0} / \mu_{ref}$$

$$L^* = L_{input} / L_{ref}$$

For consistency U_{ref} and μ_{ref} has to be

$$U_{ref} = \sqrt{P_{ref} / \rho_{ref}}$$

and

$$\mu_{ref} = \rho_{ref} U_{ref} L_{ref}$$

It is important to make sure that all values, X^* , X_{input} and X_{ref} are self consistent, i.e. follows the physical laws for ideal gases, see Section 2.3.

There are some limitations following from values that are hard-coded into the program, for example the gas constant (for most cases) has to be the one for air, 286.96. This is because HYDRA in its internal nondimensional stage simply uses the ideal gas equation as

$$P^* = \rho^* T^* \tag{4.3}$$

Expecting $R^* = 1$

Other restrictions are that the reference temperature, the one for which μ_{ref0} in Sutherland's law occurs is fixed to 288K and the constant S_{suth} is fixed to 110.3. This means that for now HYDRA will only work for gases that have the same constants R and S_{suth} as air. By using the STP2, see subsection 4.2.2, mode for feeding data to HYDRA there is a way to get around some of these issues.

For Rolls-Royce's internal purposes the constraint is acceptable since HYDRA at the moment is primarily used for civil air craft engines and the combustion of Jet A1, which is the fuel used in most of the commercial air craft engines, actually has nearly the same R and S_{suth} as air. I.e. HYDRA will work well for those calculations by only altering the value of γ . However, current development towards a more general gaseous fluid is ongoing.

The following chapters describe how HYDRA will interpret input data in SI and STP2 mode respectively.

4.2.1 SI

In SI "mode" all of HYDRA's internal reference values are set to match atmospheric standard values for air (STP) and the reference length is 1 meter, i.e.

$$\rho_{ref} = 1.226 \text{ kg/m}^3$$

$$P_{ref} = 101300 \text{ Pa}$$

$$T_{ref} = 288 \text{ K}$$

$$L_{ref} = 1 \text{ m}$$

$$U_{ref} = \sqrt{101300/1.226} = 287.45 \text{ m/s}$$

$$\mu_{ref} = 1.226 \cdot 287.45 \cdot 1 = 352.41 \text{ Ns/m}^2$$

Further the viscosity is fixed to follow the behaviour of air at all time. This is done through Sutherland's law, Equation (2.23), where the Sutherland reference viscosity μ_{ref0} and the Sutherland temperature S_{suth} are "hardcoded". Of these two μ_{ref0} is the one that needs consideration when applying the SI scaling. For a reference temperature of 288K we have

$$\mu_{ref0} = 1.79 \cdot 10^{-5} \text{ Ns/m}^2$$

As said earlier, the Reynolds number has to remain the same as of the actual test cases at all time. This results in the following

$$Re = \frac{\rho_w U_w L_w}{\mu_w} = \frac{\rho_{input} U_{input} L_{input}}{\mu_{ref0}} \quad (4.4)$$

where

$$L_w = L_{input}$$

and

$$U_{input} = Ma\sqrt{\gamma R_{STP} T_{input}} \quad (4.5)$$

with

$$1 \cdot 10^{-6} > Ma > 0.3$$

The variables denoted “w” represents the actual test case and the ones denoted “input” are the ones to be fed into HYDRA.

Since μ_{ref0} is fixed in the code the choices that remains to satisfy the Reynolds number are to change ρ_{input} , T_{input} , or P_{input} . They have to be changed in, at least, pairs to make sure that the relationship between pressure, density and temperature follows the one for air at all time, i.e. follow the ideal gas law with the gas constant, R , fixed to 286.96. This means that ρ_{input} has to be substituted with $P_{input}/(R_{STP}T_{input})$, according to the ideal gas law, if one wants to perform the calculations on a specific pressure or temperature. For simplicity, here ρ_{input} and P_{input} has been changed to satisfy the Reynolds number, T_{input} is chosen to 288K.

The “new” ρ_{input} is provided by

$$\rho_{input} = \frac{\rho_w U_w L_w \mu_{ref0}}{\mu_w Ma \sqrt{\gamma R_{STP} T_{input}}} \quad (4.6)$$

And then P_{input} from the ideal gas law

$$P_{input} = \rho_{input} T_{input} R \quad (4.7)$$

4.2.2 STP2

In this case the user is responsible for the nondimensionalisation and can use reference values of own choice. Further it is the nondimensional values denoted with a “*” that are to be fed into HYDRA and not the ones denoted “input”. Choosing one’s own set of reference values allows the user more freedom and one can actually change the ideal gas constant R as long as the input values and the reference values represent the same ideal gas i.e. $R^* = R_{input}/R_{ref} = 1$. It is important to remember that gamma also has to be changed if this is done since both gamma and R are determined from the same two constants, see Equations (2.17) and (2.21) in Subsection 2.3.1.

In difference to SI “mode” this time HYDRA will demand that the user supply a nondimensional Sutherland reference viscosity, μ_{ref0}^* , herself. This will make the viscosity-temperature curve offset. As mentioned before both the Sutherland’s temperature (S_{Suth}) and the reference temperature (T_{ref}), at which μ_{ref0} occurs, are fixed inside the code to 110.3K and 288K respectively. This means that when calculating the new μ_{ref0} it has to be done at 288K, and that the working fluid has to be an ideal gas with a Sutherland’s constant of 110.3, i.e. the same as for air.

In this case there is a possibility to change the viscosity instead of the density to make the Reynolds number match. How the nondimensional values are calculated is described below.

From Equation (4.2) for the Reynolds number we get

$$\mu^* = \frac{U^* L^* \rho^*}{Re_w} \quad (4.8)$$

where

$$U^* = \frac{U_{input}}{U_{ref}} = \frac{Ma \sqrt{\gamma R_{input} T}}{\sqrt{R_{ref} T_{ref}}} \quad (4.9)$$

From the nondimensionalised Sutherland's law inside HYDRA we have

$$\mu^* = \mu_{ref0}^* \frac{T^* \sqrt{T^*}}{1 + slaw(T^* - 1)} \quad (4.10)$$

in which

$$slaw = \frac{1}{1 + \frac{S_{suth}}{288}} \quad (4.11)$$

By comparing Equation (4.10) with the original Sutherland's law, Equation (2.23), one can, through some algebra, see that the denominator under S_{suth} , equal to 288 in HYDRA's equation, is in fact T_{ref} .

As said before, to make it all work correct R^* has to be equal to 1 and therefore $R_{input} = R_{ref}$. By letting the reference density and the reference temperature equal their corresponding input values we have $T^* = \rho^* = P^* = 1$. This approach easily resolves the nondimensional reference viscosity since $\mu_{ref0}^* = \mu^*$ when $T^* = 1$. Equations (4.8), (4.10) and (4.12) combined gives the solution in Equation (4.13).

$$U^* = Ma \sqrt{\gamma} \quad (4.12)$$

$$\mu_{ref0}^* = \mu^* = \frac{Ma \sqrt{\gamma} L}{Re_w} \quad (4.13)$$

Without using the simplification where the input temperature is the same as the reference temperature one would have to use the Newton-Raphson¹ method, or some other similar algorithm, to resolve μ_{ref0}^* through iteration. Since both the Reynolds equation and Sutherland's law is dependent on the temperature.

It might feel that it would be more natural to let the "input" values be the ones of the actual case in water and then let the reference values be the ones at STP of air. The problem is that water does not follow the gas law and therefore can't be self consistent when forced into it. If one were to chose values representing water as sea level, for instance by letting $P = 101300$ and $\rho = 998$ and then let them pass through the gas law, together with $R = 286.96$, the solution would have had to take place at a temperature near absolute zero and would have made no sense at all. If the temperature span in the solution is expected to differ more than a few percent it is also probable that the temperature would be forced below zero, which most likely will result in errors in the solver.

¹ The Newton-Raphson method uses an iterative process to approach one root of a function

When using the STP2 scaling the output from HYDRA will be nondimensional as well and has to be scaled back. This is simply a rewinding of the process and is described in Appendix A. Input values for different Mach numbers are presented in Appendix E.

4.3 Boundary conditions

In HYDRA five different boundaries types have been used, Freestream, Inviscid wall, Symmetry plane, No slip and Slip wall. How these have been applied to the geometry can be seen in Figure 4.1.

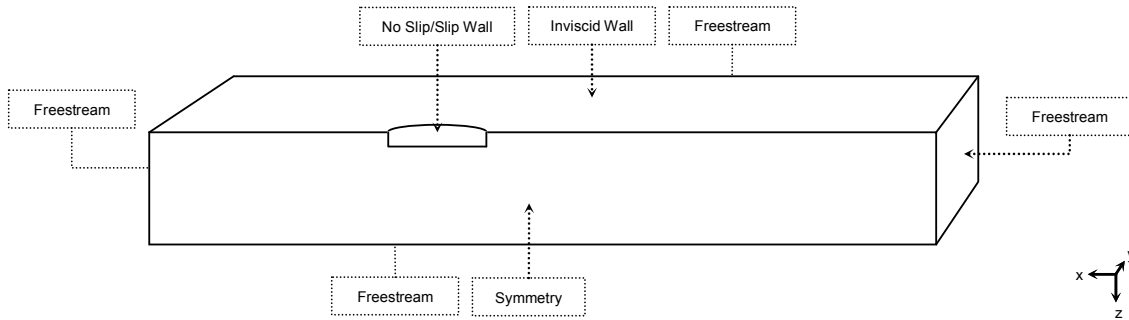


Figure 4.1: Boundary conditions used in HYDRA.

The most logical setup would be to use Symmetry planes on most of the boundaries. The reason why this has not been done is because the Symmetry condition in HYDRA is limited to be applied on only one plane which has to be normal to the y-direction. Therefore the “free surface” has been set to an Inviscid wall while the far field’s in both lateral and downward directions together with the inflow and outflow as Freestreams.

The Inviscid wall boundary should in theory give the same results as if a Symmetry plane had been used, i.e. the gradient normal to the surface is equal to zero. The Freestream condition on other hand is not always an ideal replacement for the Symmetry condition, since it forces the fluid to retain a specified velocity and direction on the boundary. In HYDRA [17] the Freestream boundary is referred to as a “true far field boundary with uniform conditions”. In this case, because that the affected boundaries are located far away from the hull the flow can be assumed to be unaffected by the hull at that point. Consequently Freestreams work fine.

The Freestream boundary was the only one of the five that required definition and the following settings were used, see Table 4.1. Spalart variable is another name for turbulent viscosity ratio.

Table 4.1: Freestream boundary conditions. Because of the STP2 scaling all values are presented in their nondimensionalised form.

	Spalart-Allmaras	k- ω SST
Density	1	1
Pressure	1	1
Mach number	$1 \cdot 10^{-6} - 0.7$	$1 \cdot 10^{-6} - 0.7$
Angle of attack	180	180
Yaw angle	0	0
Spalart variable/Turbulent viscosity ratio	10	1.01
Turbulent intensity	–	1%

The specified density and pressure are the nondimensional values. The angle of attack sets the flow direction in the x-y plane and the yaw angle in the x-z plane, both were chosen to be normal to the inlet boundary. In HYDRA the global coordinate system is specified to “point” opposite to the coordinate system used in the mesh, therefore the angle of attack had to be set to 180 degrees.

The transition point between laminar and turbulent flow is hard to determine in a 3D model and HYDRA will not run with transition turbulence models. Therefore the flow must be assumed to be fully turbulent.

At a late state in the project a discussion rose about whether it was really correct to let a Freestream represent the outflow. To validate this two trial runs were made using different outflow boundaries. For the first one a normal Outflow was used, on which only the static pressure were defined, and for the second a Mass flow outlet, through which the total inflow mass was conserved, was used. Results from both calculations came out the same as with the Freestream boundary.

4.4 Solution methods

All calculations have been performed as steady RANS and using either Spalart-Allmaras or k- ω SST for turbulence modeling, see Table 4.1 in the previous section for details.

Most of the settings in HYDRA are not changeable, because of the simple reason that there are no options to choose between. Therefore HYDRA has been used in “Default” mode for a more thorough explanation of what that means the reader is referred to Section 2.9 and HYDRA [17]. For some calculations with the structured mesh the CFL number had to be altered from 2 to 1 to achieve better control.

For all simulations a multigrid, described in Subsection 2.9.2, has been used. To initialize the flow with correct values and to get rid of singularities 200 pre-iterations have been performed on grid levels two and three, 100 iterations at each.

5 FLUENT setup

Throughout this project FLUENT 12.0.16 has been used, the program has been executed on a UNIX system and all calculations have been performed using double precision. The settings that have been made in the program are specified below.

5.1 Boundary conditions

The boundary conditions in FLUENT was set up according to Figure 5.1. The different boundaries have been located far away from the hull, i.e. the approximations on the boundaries will not affect the area of interest. See Section 3.4, Meshing, for more details.

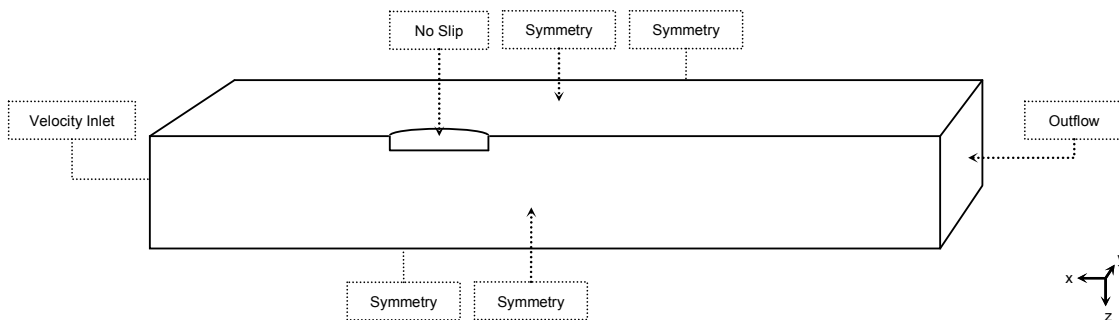


Figure 5.1: Boundary conditions used in FLUENT.

The Velocity inlet, Outflow and the Wall boundary allows you to modify the settings. In these cases have the following settings been used

Velocity inlet The velocity of the fluid entering the control volume normal to the boundary surface was specified together with the turbulent parameters. See Table 5.1 for the settings in the different cases.

Table 5.1: Conditions specified at the velocity inlet boundary.

	Spalart-Allmaras	k- ω SST
Velocity [m/s]	1.08 / 1.42	1.08 / 1.42
Turbulent viscosity ratio	10	1.01
Turbulent intensity	–	1%

Outflow The flow rate weight on the outflow boundary was set to 1, i.e. 100% of the water entering the velocity inlet boundary leaves the control volume through the outflow boundary.

Wall The hull has been chosen to a stationary wall, i.e. not moving (the speed of the fluid represents the speed of the ship). The shear condition is set to no-slip, meaning that the fluid closest to the wall is moving with the same speed as the ship – 0 m/s in these cases. Roughness parameters has been specified to represent a smooth wall (Roughness height = 0) which is believed to be the truth for a towing tank model.

5.2 Fluid properties

The fluid properties, presented in Table 5.2, were chosen to be the same as during the physical experiments, Ju [11] and Journée [10], discussed in Section 3.2.

Table 5.2: Fluid properties specified in FLUENT.

	Wigley I	Wigley II
Density [kg/m ³]	998	998.623
Viscosity [kg/ms]	$1 \cdot 10^{-3}$	$1.046 \cdot 10^{-3}$

5.3 Solution methods

In FLUENT the Segregated Pressure Based solver was used for all calculations, Table 5.3 presents the solution controls. All other available settings have been left as the default ones. As in HYDRA both Spalart-Allmaras and k- ω SST has been used for turbulence modeling, see Table 5.1 in Section 5.1 for details.

Table 5.3: Solution controls used in FLUENT. Note that there is no setting for the turbulent dissipation when using Spalart-Allmaras as turbulent model.

Pressure-Velocity coupling	SIMPLE
Gradient option	Green-Gauss Node based
Pressure	Second order
Momentum	Second order upwind
Turbulent kinetic energy	Second order upwind
Turbulent dissipation	Second order upwind*

*Not applicable for Spalart-Allmaras

For all simulations FLUENT's default multigrid, described in Subsection 2.10.5, have been used.

6 Results and discussion

Over 200 runs have been conducted for the two test cases presented in Chapter 3 with the purpose to investigate how parameters such as Mach number, boundary layer resolution, wall model and turbulence model influenced the results. The runs were made at several Mach numbers between 10^{-6} and 0.7 for up to 17 different meshes. A summary over all calculations can be found in Appendix E.

After a number of preliminary test runs it was decided to use the STP2 scaling, described in Subsection 4.2.2, in HYDRA, mainly because it meant that less data had to be fed into the program when both pressure and density could be set to 1.

When reading through the following chapter there are a few things that are important to bear in mind. Both the viscous and the pressure resistance are calculated through integration over the hull surface in the x-direction, i.e. integrated pressure resistance and integrated viscous resistance. Results are presented as resistance coefficients (C_v , C_p , C_t), how the resistance and its coefficient relate to each other is explained in Appendix A under the Section "Scaling output from HYDRA".

All calculations (except from Section 6.5 where the effect of different Froude numbers is investigated) have been done at constant Reynolds numbers, one for Wigley I and another for Wigley II. This means that when a resistance coefficient changes with the Mach number it is likely an effect of the computational scheme in the code or the mesh rather than a physical phenomenon. How the scaling was done is presented in Section 4.2. Results from FLUENT are not dependent on Mach number since they have only been calculated under the same conditions as in the test cases, see Chapter 5. Therefore they are presented as horizontal lines over a changing Mach number. Obviously the same goes for the experimental data.

In many of the following figures it will be referred to the Froude number, this is because it is the common way to describe a ships velocity. It might seem a bit contradictious after reading Section 4.1, Similarity but it basically means that the CFD calculations are made to preserve the Reynolds number present at the given Froude number for the test case.

In figures y^+ is an estimate from the freestream Reynolds number (see Appendix A for further explanation) and is not directly representing the actual y^+ , which changes over the hull dependently on the local Reynolds number. Further to achieve the same y^+ in HYDRA and FLUENT the resolution of the boundary layer has to be different and therefore different meshes are used for the same y^+ , e.g. a y^+ of 60 in HYDRA corresponds to a y^+ of 30 in FLUENT (see Section 2.7, Cell vs. Node based solver)

A small error was made when scaling the input conditions to STP2 (see Subsection 4.2.2) for the Wigley II test case and it affects all calculations for the Wigley II hull. The effect of the error is assed in Appendix B and shown to be negligible ($< 0.25\%$).

6.1 Experimental results

In the past the two hull shapes have been exhaustively tested and lot of experimental results are available. However, existing total resistance measurements were only found for Wigley II while for Wigley I they had to be estimated using methods from ITTC-57 and Watanabe [12]. For further explanation of the resistance components used in the following subsections the reader is referred to

Section 2.1, Ship resistance. The existing data for the two hulls are presented in the following subsections.

6.1.1 Wigley I

In Journée [10] the resistance for the Wigley I hull at a Froude number of 0.2 is measured. For comparisons between those results and the CFD results for Wigley I the total resistance coefficient (C_t) was calculated by extracting the wave resistance using methods by ITTC-57 and Watanabe. The result from those calculations is essentially the sum of the viscous and pressure force gained from the CFD calculations.

The breakdown of the resistance components are shown in Table 6.1. For a detailed explanation of this procedure see Appendix A.

Table 6.1: Resistance components and total resistance coefficient for Wigley I.

Measured resistance (including wave making and breaking)	5.98 N
Wave resistance	0.72 N
Remaining total resistance	5.20 N
Total resistance coefficient (C_t)	0.00452

Generally this method is not used anymore because newer more accurate methods have been proposed later (ITTC-78). The reason to why this method was used anyway was mainly due to lack of experimental results. However, because of the slender shape of the hull this method is assumed to be accurate enough [12].

6.1.2 Wigley II

In Ju [11] the total resistance coefficient (C_t) for the Wigley II hull was measured and calculated by using a wake survey method. It basically means that the resistance is calculated from wake measurements of the total head (pressure) and the longitudinal velocity component which enables the contribution from wave making and breaking to be excluded. The results were compared with results from various reports for the same hull shape derived by wave-pattern analysis and was proven to agree well at Froude numbers between 0.24 and 0.34. Results from the measurements are shown in Figure 6.1.

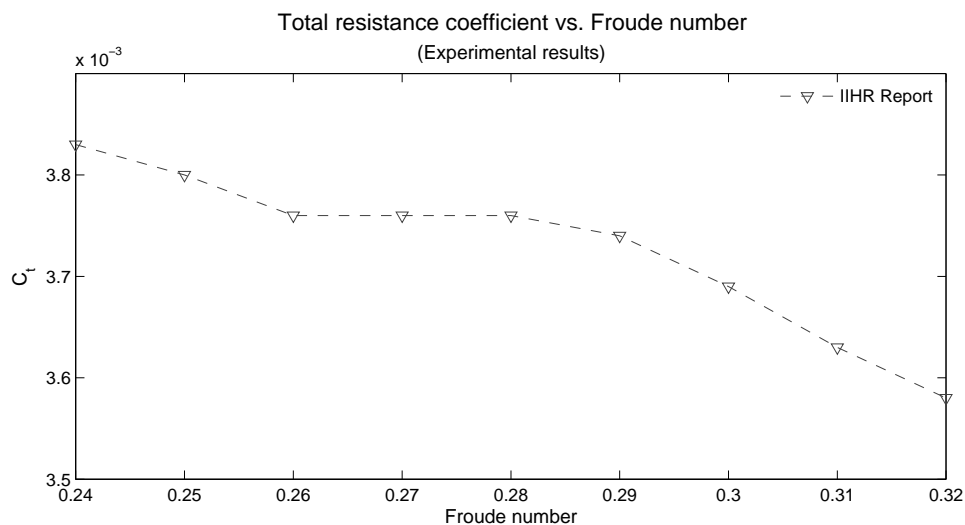


Figure 6.1: Measured total resistance coefficient for Wigley II.

As a validation to the method used for Wigley I the total viscous resistance have been computed in the same way, described in Appendix A, for Wigley II at F_n 0.26. After the wave resistance had been subtracted a total resistance of 4.93 N remained. That gave a C_t of 0.00354 which is around 6% from the wake survey data.

6.2 Mach number dependence

A relationship between Mach number and resistance has been established through a number of runs at Mach numbers between 10^{-6} and 0.7 with constant Reynolds number, both with and without the LMNP. The calculations have been done using the mixed mesh with y^+ at 1 for Wigley I, and for both the mixed and structured meshes, again with y^+ at 1, for Wigley II. For all cases the Spalart-Allmaras turbulence model was used. The results have been validated against experimental data, see Section 6.1, and FLUENT calculations under similar conditions and can be seen in Figure 6.2 A-C and Figure 6.3 A-C for Wigley I and Wigley II respectively.

For Wigley I, Figure 6.2 A-C, large irregularities in the resistance can be observed at the very lowest Mach numbers (10^{-6} and 10^{-5}). A closer look at the convergence history for those runs shows that they have in fact not converged and therefore their results can be neglected (see Section 6.7 for a general convergence discussion).

Observing the total resistance in Figure 6.2 A and Figure 6.3 A for the mixed meshes using the LMNP it can be seen that both curves have a slope towards a peak at Mach number 0.25, where the LMNP is designed to meet the Default solution. For Wigley I the increase is 7.50% and for Wigley II 3.05%. This is in contrast to the results from the structured mesh where there is no slope at all. Therefore it is reasonable to believe that HYDRA has problems with the unstructured cells in the mixed meshes. That the slope is less pronounced for Wigley II than for Wigley I further indicates that the LMNP is either mesh or geometry sensitive.

Judging from the experimental values the best results from HYDRA are obtained around Mach number 0.25 while judging from the results using the structured mesh together with results from FLUENT will say that the most accurate solutions are acquired at the lowest Mach numbers. It seems more reasonable to trust the latter since the resistance calculated with structured mesh gives no tendencies to increase.

In the Mach number range between 0.25 and 0.7 it can be seen that for Wigley I the total resistance remains constant, as a result of an decrease in viscous resistance together with a simultaneously increase in pressure resistance. For Wigley II, with both the mixed and structured mesh, the total resistance decreases, an effect of solely the viscous contribution since the pressure resistance remains fairly constant. The rising pressure curve, most significant for Wigley I, in this region could be an effect of compressibility (see Figure 2.3, Subsection 2.3.3). Note that the curves for the two FLUENT calculations coincide and appear as one in Figure 6.3 C.

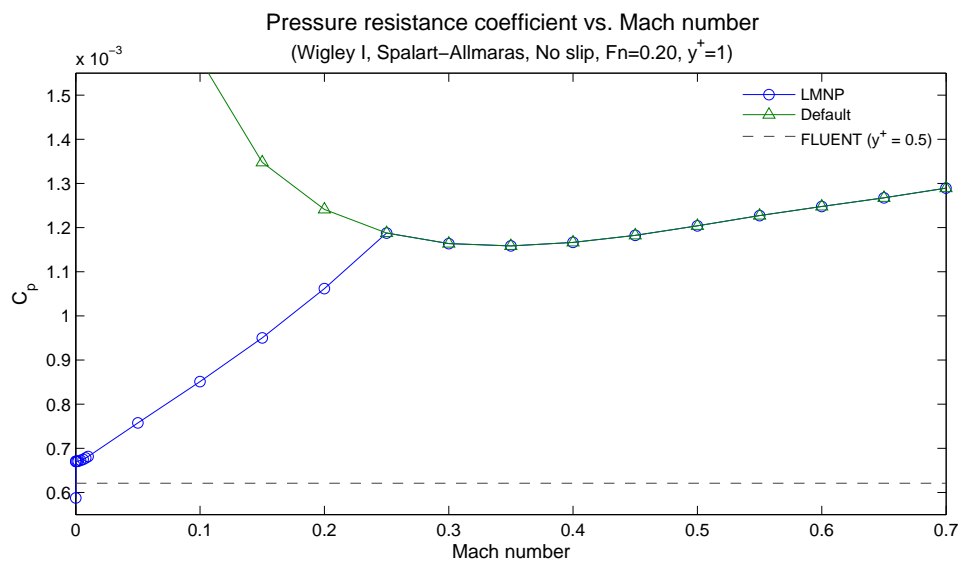
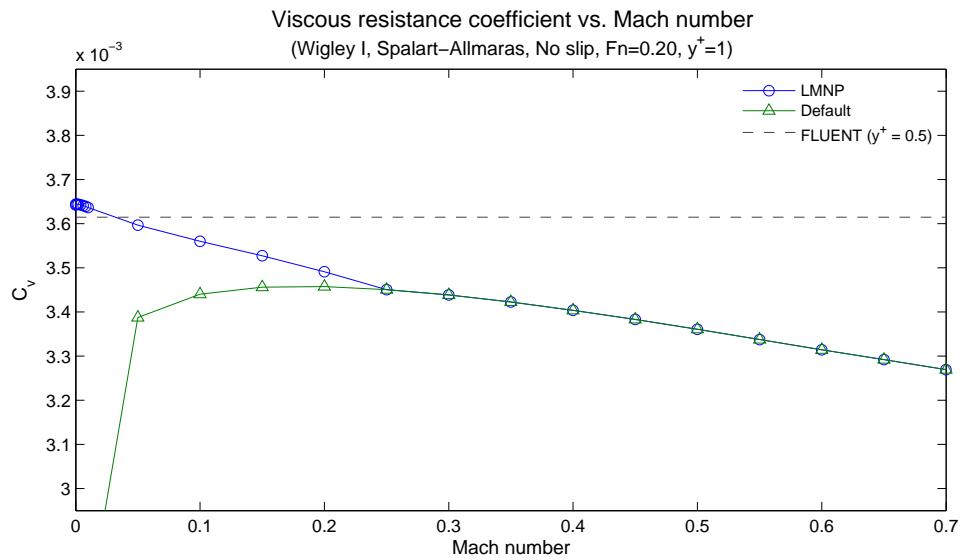
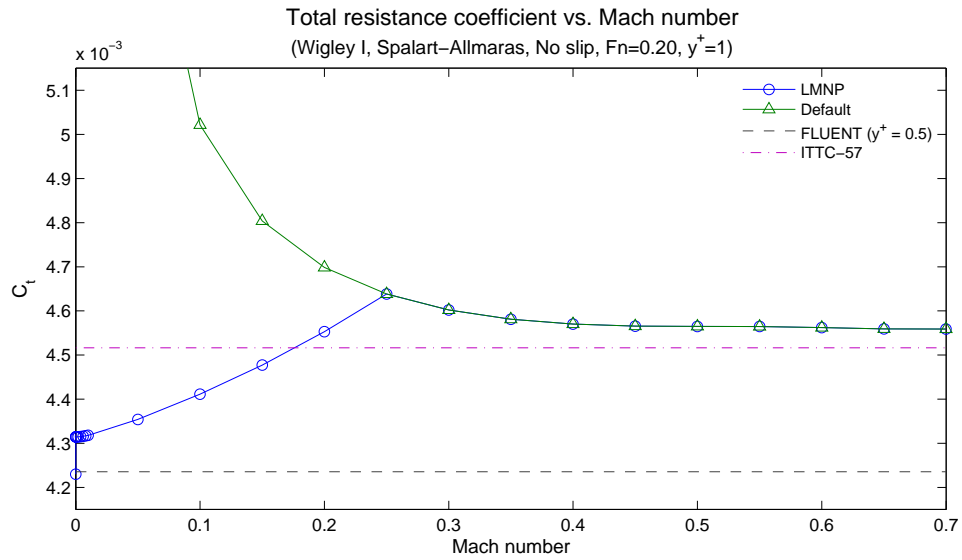


Figure 6.2 A-C: The total (A), viscous (B) and pressure (C) resistance coefficients are shown as a function of Mach number for Wigley I's mixed mesh with y^+ at 1. Using both LMNP and the Default mode.

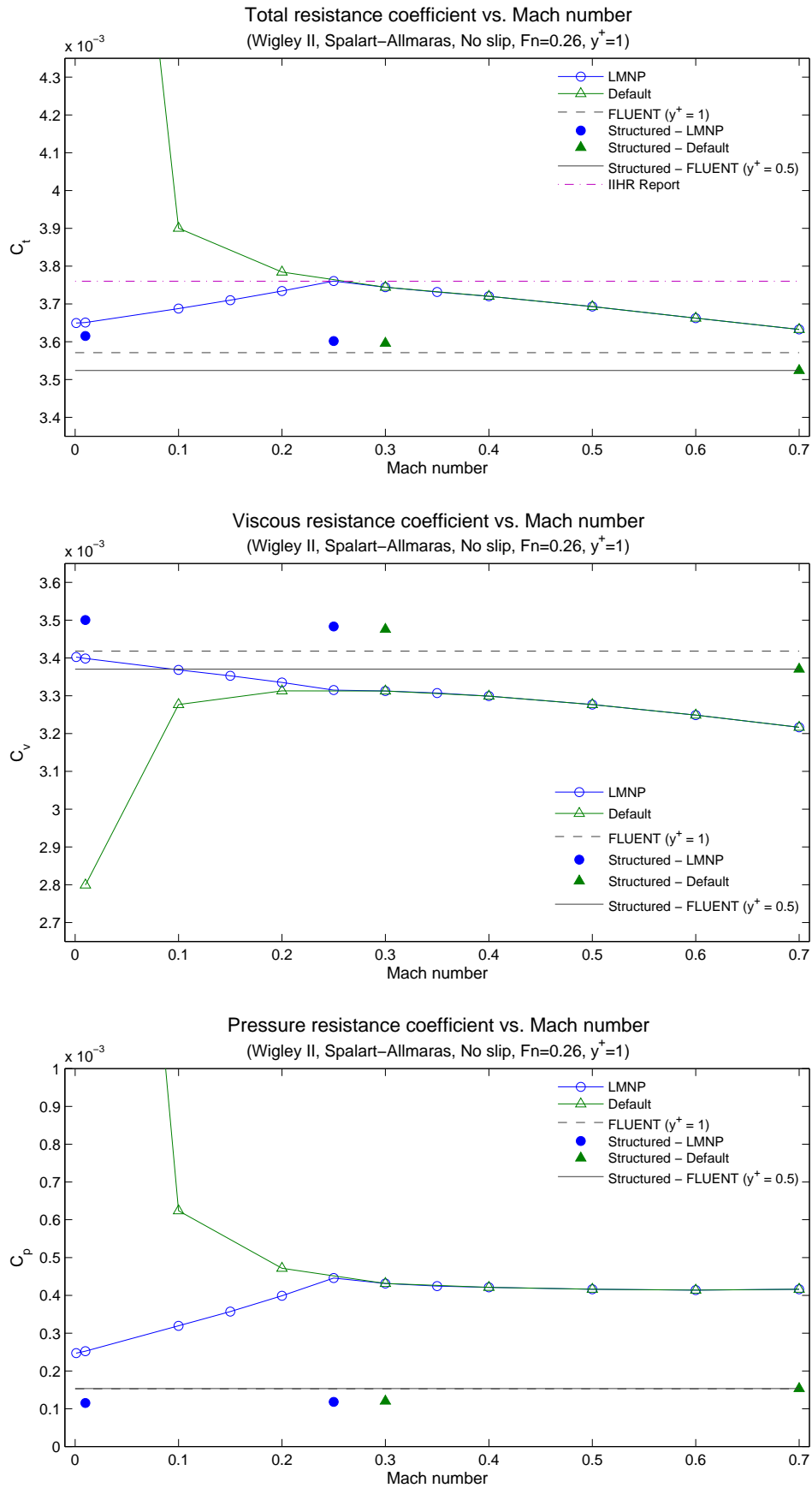


Figure 6.3 A-C: The total (A), viscous (B) and pressure (C) resistance coefficients are shown as a function of Mach number for Wigley II's unstructured and structured meshes with y^+ at 1. Using both LMNP and the Default mode.

With the mixed meshes between Mach numbers 0.25 and 0.7 results from runs using the LMNP and ones using the Default mode are inseparable, indicating that the LMNP have no influence in that region. The LMNP is, as mentioned in Subsection 2.9.4, dependent on the local flow properties and is designed to switch on whenever the Mach number becomes lower than 0.25. For well behaved flows, like the ones around the Wigley hulls, the velocity variations outside the boundary layer are relatively small and the Mach number remains fairly constant. This result in that the LMNP never really kicks in for the runs that have inflows with Mach numbers over 0.25 and therefore those calculations predict the same resistance both with and without LMNP.

On the other hand the statement that the velocity changes are small does not go well with the flow inside the boundary layer, where the velocity drops towards zero when approaching the wall. But since the pressure inside the boundary layer is controlled by its surrounding pressure and also estimated to be constant through its thickness, this area only becomes affected by the LMNP if the velocity of the surrounding flow drops below Mach number 0.25.

6.3 Dependence of boundary layer resolution

The effect on resistance prediction against boundary layer resolution has been investigated for Wigley I as well as for Wigley II, this required all different meshes presented in Section 3.4 to be used. Again the results have been validated against experimental data and FLUENT calculations and can be seen in Figure 6.4 A-C for Wigley I and Figure 6.6 A-C, found in Subsection 6.3.1, for Wigley II.

In Figure 6.4 A, showing the total resistance for Wigley I, it can be seen that for Mach number 0.01, HYDRA results fluctuate around 3.88% over the whole range while FLUENT values stay steadier at 3.61%. If the runs performed at y^+ between 5 and 30 are disregarded, which is fair as they are placed within the buffer layer (see Section 2.6, "Boundary layer and its modelling"), the fluctuations reduces to 3.00% for HYDRA and 2.37% for FLUENT.

The results for Wigley II, Figure 6.6 A-C in next subsection, show a fluctuation of 4.49% in HYDRA and 2.74% in FLUENT, over the whole range. Once again disregarding the meshes which places y^+ inside the buffer layer the fluctuation reduces to 3.07% for HYDRA and 1.52% for FLUENT. Though, it can be argued whether it is fair to place y^+ at 4 since it is on the border to the buffer layer and only a small change in the local Reynolds number could push it over into the buffer layer. But according to FLUENT it should work [6].

From Figure 6.6 B-C it can be observed that even if HYDRA predicts a reasonable total force for higher y^+ the viscous and pressure decompositions differs hugely compared to FLUENT. The explanation is that the slip wall function is turned on automatically in FLUENT while in HYDRA this is an option that has to be implemented manually. In the next subsection results using a Slip wall in HYDRA are presented.

Comparing the curves for Mach numbers below 0.25 with the one at 0.3 it can be seen that the relationship between them changes somewhere around y^+ between 20 and 30, this indicates that the LMNP either is affected by the mesh or the wall function.

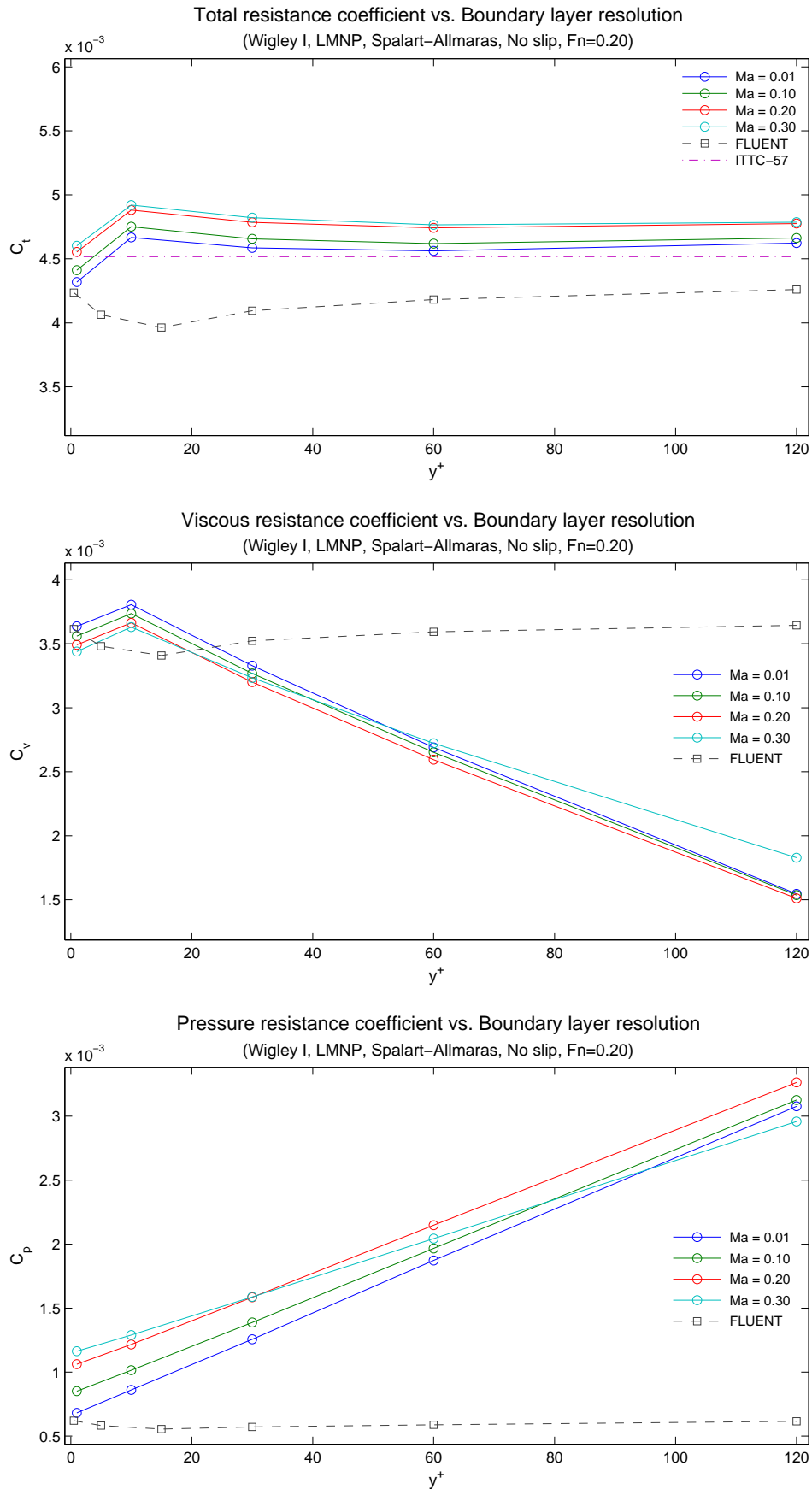


Figure 6.4 A-C: The total (A), viscous (B) and pressure (C) resistance coefficients are shown as a function of boundary layer resolution for Wigley I at four different Mach numbers.

6.3.1 Introducing Slip Wall

A Slip wall condition (see Subsection 2.6.2) has been introduced in HYDRA to enable the code to work with coarser boundary layers. The results for the Wigley II hull can be observed in Figure 6.6 A-C. Results for Wigley I follow the same trends and can be observed in Appendix D.

From Figure 6.6 A-C it can be seen that with the No slip condition the viscous resistance becomes under predicted with the coarsening of the mesh in the boundary layer while in return the pressure resistance becomes over predicted. The explanation is likely that the momentum gradient near the wall becomes under predicted as a result of the coarse mesh (as discussed in Subsection 2.6.2) which in turn results in a small momentum loss and an under predicted viscous resistance. Then, as a result the pressure has to compensate. When using a Slip wall condition the near wall momentum loss is regained through the introduction of a velocity on the wall.

Figure 6.5 shows the actual near wall velocities for three different runs using the mixed y^+ 1 and 120 meshes with No slip and again the mixed y^+ 120 mesh with Slip wall, all for Wigley II at Mach number 0.01 with Spalart-Allmaras. The measurements were made along a line normal to the hull surface midship in the assumed free surface plane ($z=0$). Since the momentum could be interpreted as the velocity square it can be seen that when using the mesh with y^+ at 120 with the No slip condition there is a momentum loss compared to the mesh with y^+ at 1. With the Slip wall condition the loss is compensated.

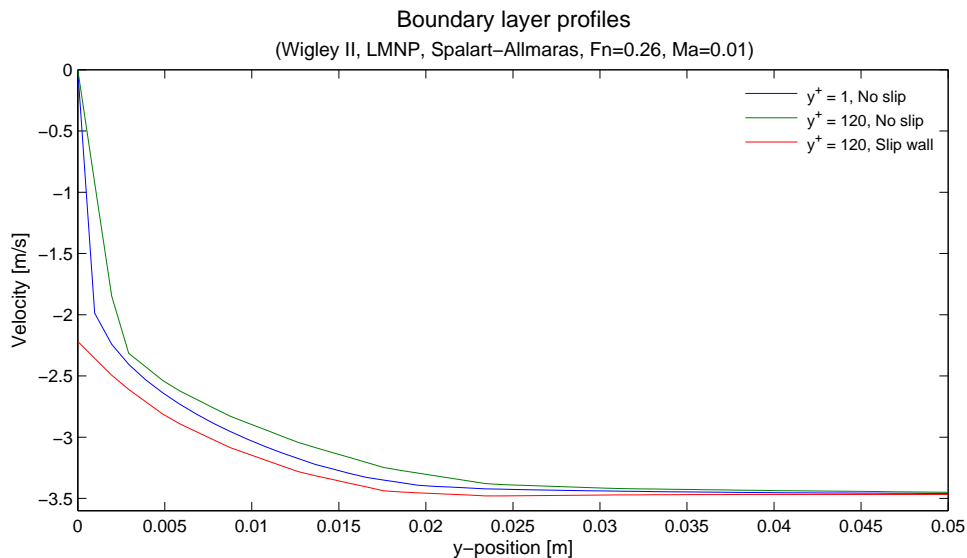


Figure 6.5: Velocity profile along y-position for three different cases.

While the momentum in the near wall region is critical for the correct viscous and pressure resistance prediction it has little effect on the total resistance, as can be seen in Figure 6.6 A where the Slip wall and the No slip cases almost predict equal resistance. The explanation could be that in this case, where the hull is relatively slender and the flow gets fully attached, there is no separation and the total momentum flux in the x-direction will be nearly same for both cases. Further, the loss of momentum in the near wall region is relatively small, compared to the total momentum, and therefore its effect will be insignificant. For the structured mesh with y^+ at 120 the total resistance between the Slip wall and the No slip calculation differ around 2.5%, which still can be considered small and therefore does not interfere with the reasoning for the mixed mesh.

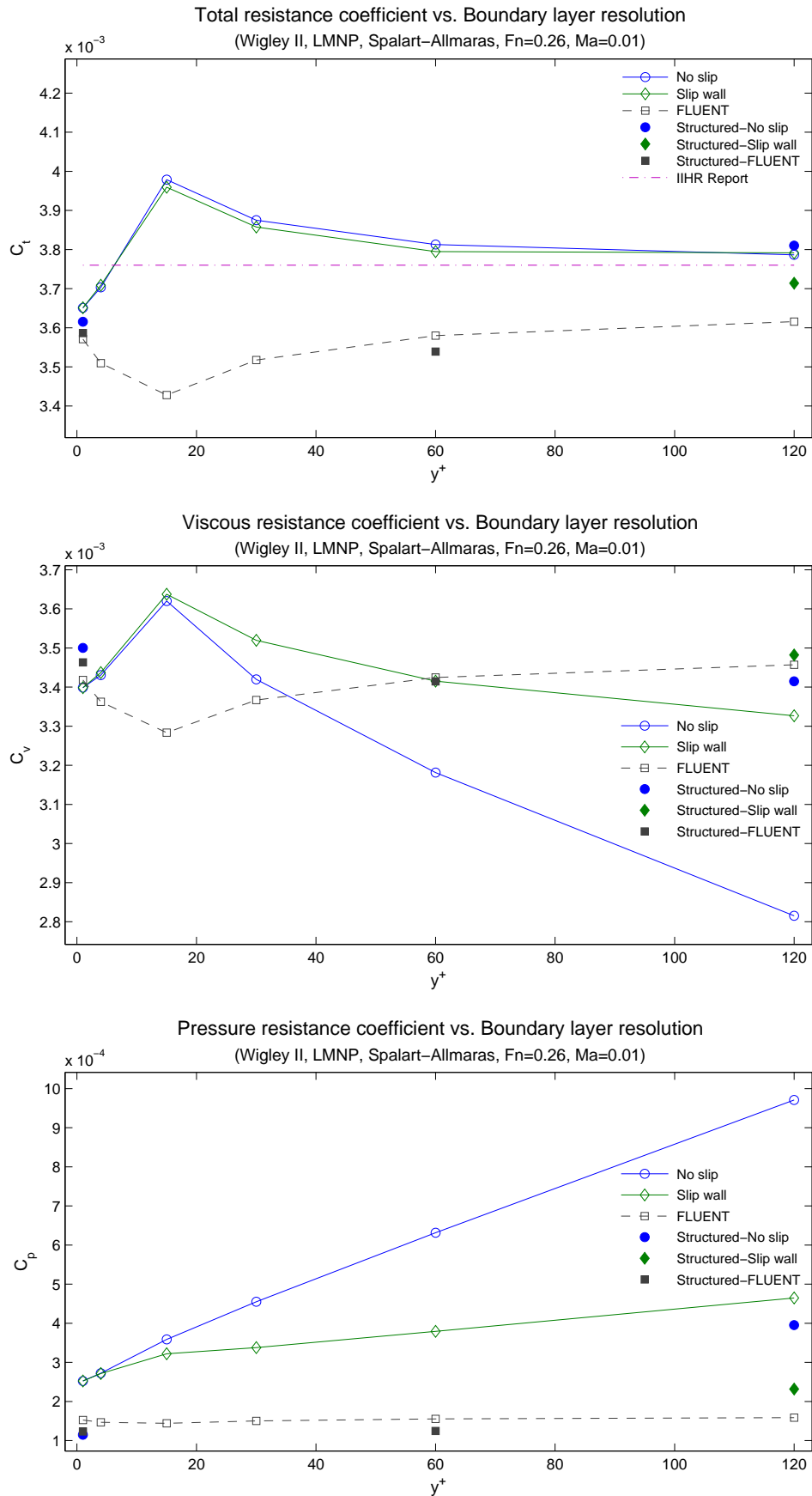


Figure 6.6 A-C: The total (A), viscous (B) and pressure (C) resistance coefficients are shown as a function of boundary layer resolution for all Wigley II's mixed and structured meshes at Mach number 0.01 with S-A turbulence model.

If instead the geometry would have made the flow separate heavily in the aft it is reasonable to assume that the momentum flux in the x-direction would differ between the Slip wall and the No slip run, since separation is arbitrary. Though the total momentum would still add up to, around, the same when taking all directions into account (x, y and z).

Wake cuts between several No slip and a Slip wall cases for the higher y^+ meshes were compared to validated whether the distribution between viscous and pressure resistance was a global or local effect. When no significant changes could be observed it was assumed that the changes occurred within the boundary layer, i.e. a local effect. Therefore the shear stress and pressure distribution over the hulls surface for two different No slip runs with y^+ 1 and 120 meshes have been compared with a Slip wall run using the y^+ 120 mesh. The results can be seen in Figure 6.7 A-C and Figure 6.8 A-C.

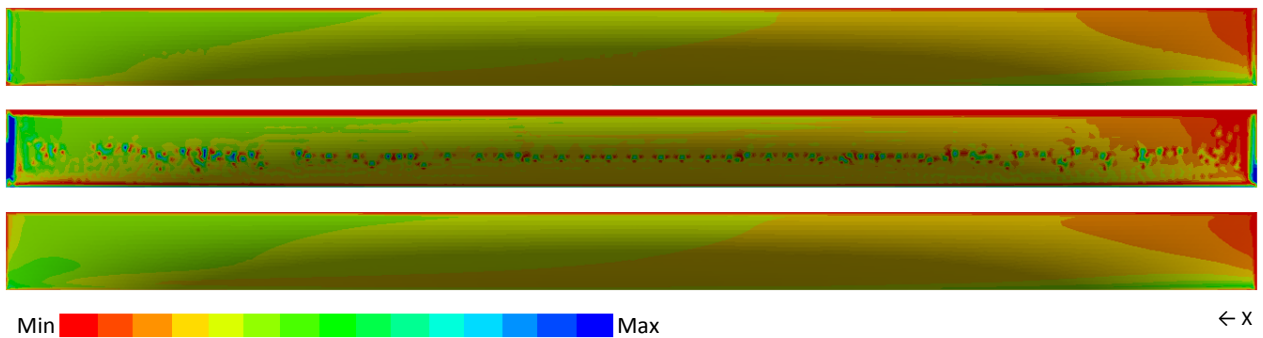


Figure 6.7 A-C: Shear stress distribution in the x-direction over the Wigley II hull, observed in the xz-plane. From the top; A shows results for the y^+ 1 mesh with No slip, B the y^+ 120 mesh with No slip and finally C the y^+ 120 mesh using Slip wall. All calculations performed at Mach number 0.01 using the LMNP.

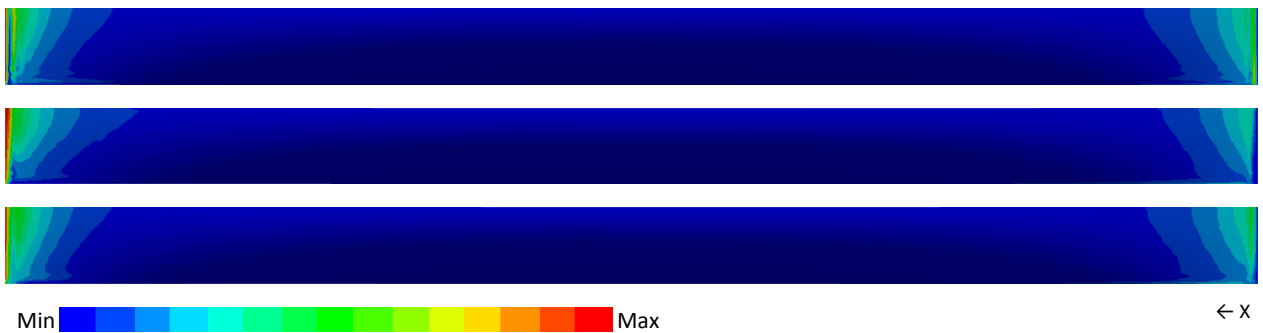


Figure 6.8: A-C: Pressure distribution in the x-direction over the Wigley II hull, observed in the xz-plane. From the top; A shows results for the y^+ 1 mesh with No slip, B the y^+ 120 mesh with No slip and finally C the y^+ 120 mesh using Slip wall. All calculations performed at Mach number 0.01 using the LMNP.

In Figure 6.7 B, showing the shear stress distribution over the hull for the mesh with y^+ at 120 using the No slip condition, it can be seen that the solver struggles and “numerical errors” seems to appear over the hull. A careful observation would also indicate a slight loss in shear stress. In Figure 6.8 B, showing the pressure distribution over the hull for the same case, a pressure peak can be observed in the bow. Figures for the y^+ 1 mesh using No slip (Figure 6.7 A and C) and the ones for the y^+ 120 mesh with Slip wall (Figure 6.8 A and C) shows resemblance in both shear stress and pressure distribution.

6.4 Spalart-Allmaras vs. k- ω SST

Since Spalart-Allmaras is not a turbulence model normally associated with the marine industry, the majority of the calculations for the Wigley II hull was repeated using the k- ω SST model. It has been established from previous sections that the Slip wall condition is something that is needed for calculations at higher y^+ , therefore only results for such calculations are presented in this section.

In Figure 6.9 A-C results are shown for all Wigley II's mixed meshes at Mach number 0.01. It can be noticed that the relations between k- ω SST and Spalart-Allmaras are opposite between HYDRA and FLUENT and now, contrary to with Spalart-Allmaras, FLUENT predicts the highest resistance (disregarding the meshes with y^+ at 1 and 4). From observing Figure 6.9 C of the pressure resistance, it can be concluded that the differences between runs using k- ω SST and Spalart-Allmaras lies solely in the viscous resistance prediction. This goes for both HYDRA and FLUENT.

Further it can be noticed that FLUENT struggles with low y^+ indicating that the k- ω SST model is not used properly all the way down to the wall.

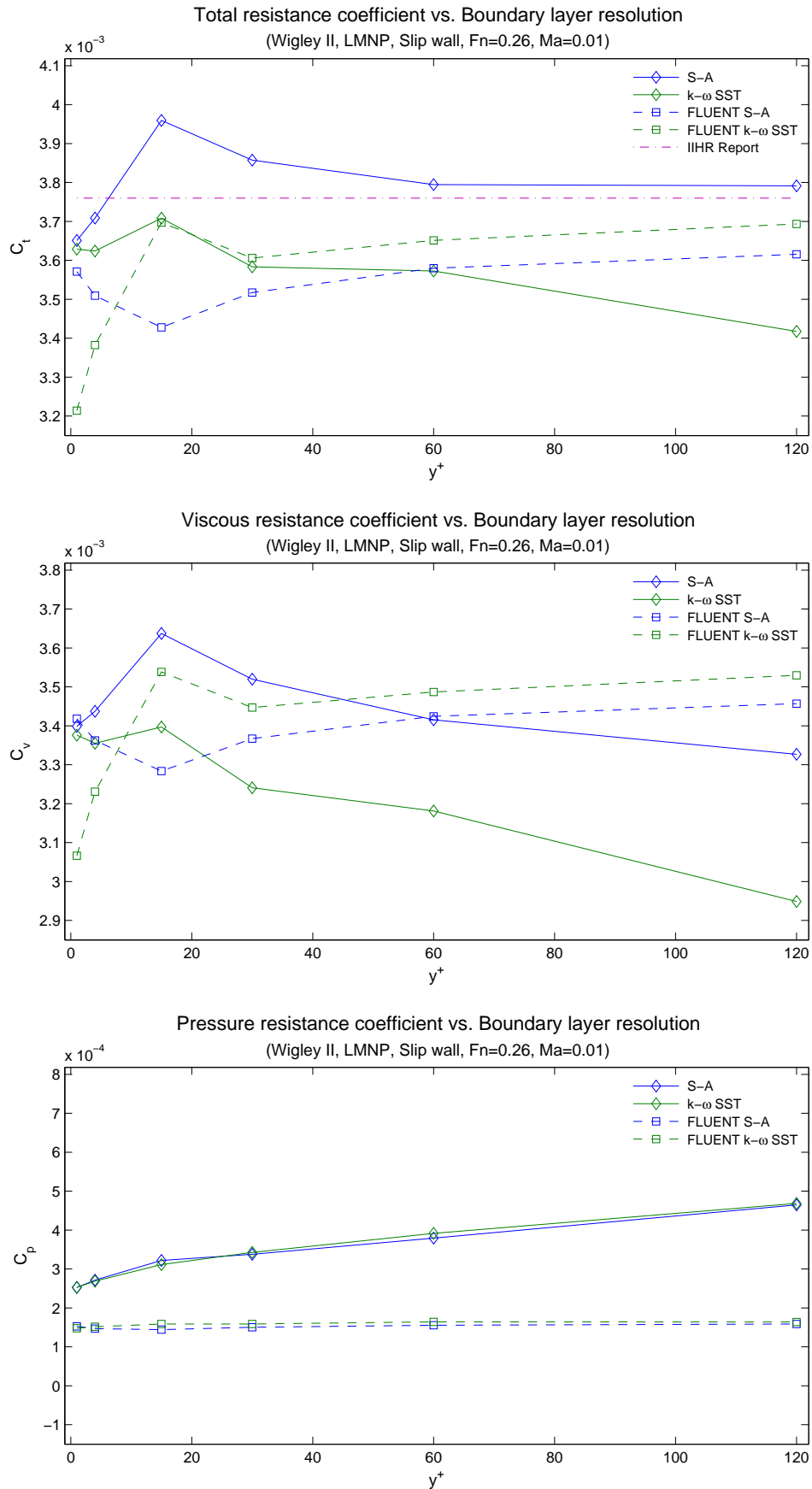


Figure 6.9 A-C: The total (A), viscous (B) and pressure (C) resistance coefficients are shown as a function of boundary layer resolution for all Wigley II's mixed meshes at Mach number 0.01 with $k-\omega$ SST turbulence model.

6.5 Froude number span

Figure 6.10 shows how well four different HYDRA calculations and one FLUENT calculation resemble the experimental data from Ju [11] over various Froude numbers. The calculations are made for the Wigley II hull using the unstructured mesh with y^+ at 1 in HYDRA and FLUENT respectively.

All results shows good agreement and the slope of the curves between HYDRA and FLUENT calculations with Spalart-Allmaras are almost equal. Comparing the Spalart-Allmaras runs with the k- ω SST run it can be seen that the latter has a slightly more aggressive slope. Further no inconsistency in the slope can be observed between the runs using the Default mode (Mach number 0.3) and the ones using the LMNP.

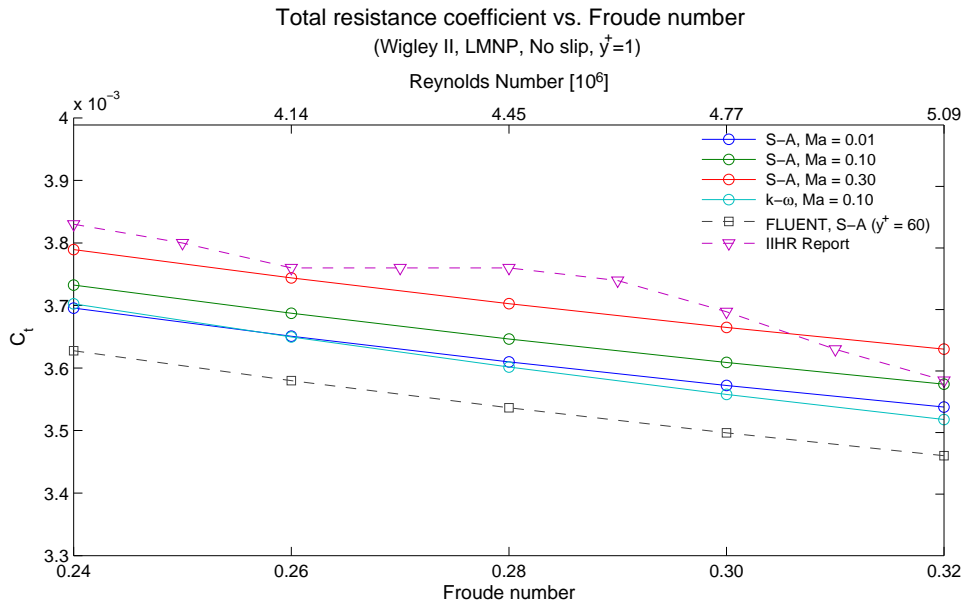


Figure 6.10: Total resistance prediction over various Froude and Reynolds numbers are validated against experimental results.

6.6 Wake cuts

Figure 6.11 shows wake cuts for Wigley II at seven positions, starting midship and extending to around 10 m behind the hull. The two top rows are both HYDRA calculations, the first one uses the unstructured mesh with y^+ at 1, and the second the structured mesh with y^+ at 1. The bottom row shows results for a FLUENT calculation using the unstructured mesh with y^+ at 1. Spalart-Allmaras has been used as turbulence model in all cases.

Because of the structured mesh's higher number of cells/nodes and its boundary layer that extends all the way to the outflow it is expected to give the highest and most precise resolution of the wake, which can clearly be seen in the figure.

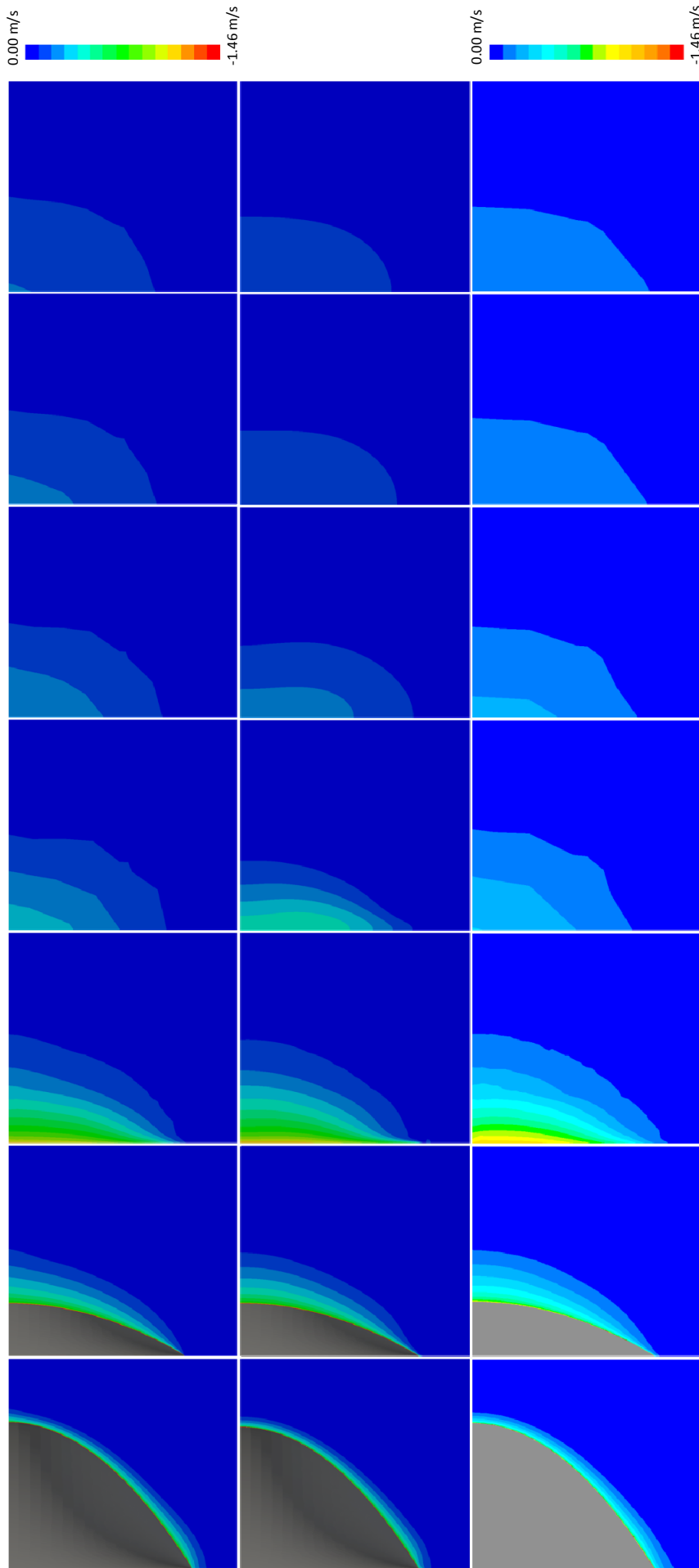


Figure 6.11: Wake cuts at different x-coordinates for Wigley II. Seen from the top; HYDRA unstructured mesh with y^+ at 1 and finally FLUENT unstructured mesh with y^+ at 1. Spalart-Allmaras was used as turbulence model for all three cases. The x-coordinates are, from the left: $x = 0$ (Midship), -1.250, -1.534, -2.524, -5.124, -8.524, -10.524.

6.7 Convergence

A way to determine if a solution has converged, or i.e. will give a trustable solution, is to examine the convergence history which shows how big the residual (the difference in flux in and out of a control volume) has been during each iteration. Note that a converged solution does not necessarily mean that the physical solution is correct; it only shows how well the mathematical problem has been solved. In an ideal case the residual should drop all the way down to zero. In FLUENT residuals are presented for each unknown, the continuity, the velocities (in x, y, z direction) and the turbulence property/properties. HYDRA, on the other hand, only presents the largest residual.

A common way to conclude whether the residual is small enough to provide an “accurate” solution is to determine how many orders of magnitude it has lowered compared to its value at the first iteration. Commonly said a drop of three in magnitude (e.g. from $2 \cdot 10^{-1}$ to $2 \cdot 10^{-4}$) means a converged solution and it is one of the limits that have been used during this study.

To easily present the drop in the figures all residuals in HYDRA were normalized with the value at iteration 201, which means disregarding the pre-iterations performed on the coarser multigrid levels, see Subsection 2.9.2. The result is a curve starting at zero and (if converging) moving downwards as the number of iterations grow. When the curve reaches -1 it means that it has dropped one in magnitude and so on. For FLUENT the third iteration is used as reference to prevent influence from a bad initial guess.

On top of the criterion that ensures that the residuals have converged there is another one ensuring that the total resistance has converged, since it is one of the main parameters of interest in this study. To decide when the total resistance was converged an average of the last 100 values from the resistance history file (a file to where the resistance is updated for every iteration) was used as a reference. Then to allow some fluctuations two limits were chosen, one stricter limit where the resistance was only allowed to deviate 0.01% from the mean and one less constrained where a deviation of 0.20% was allowed. Then, at the first iteration from where the resistance stayed within the limits the solution was considered to be converged, see Figure 6.12.

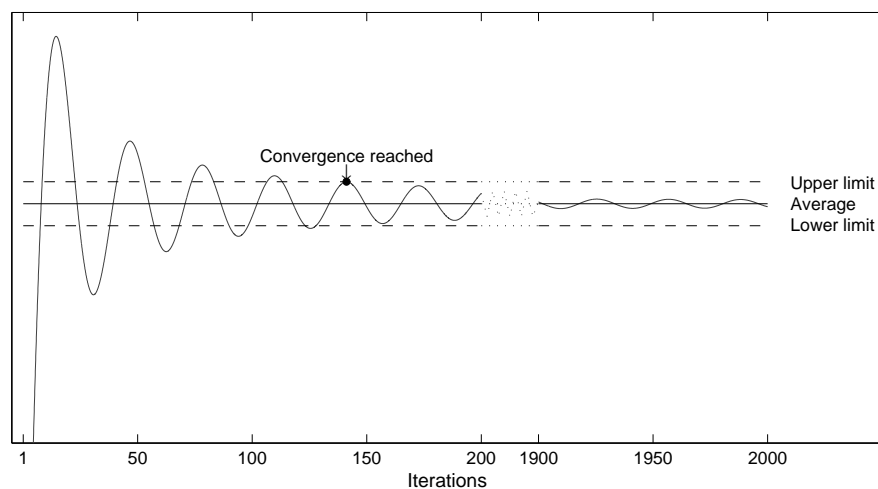


Figure 6.12: Once the total resistance stays within the limits it is assumed to be converged.

The iteration at which the total resistance is considered converge, with the stricter limit, is marked by vertical dashed lines through the figures displaying the residual history in the following two subsections.

6.7.1 HYDRA

Figure 6.13 shows four different runs performed at different Mach numbers using the $y^+ 1$ mesh for the Wigley I hull. As can be seen in the figure the convergence drop varies significantly with the Mach number. Even if the residual becomes steady for the lowest Mach numbers ($< 10^{-4}$) and in that sense has converged the residual is still nearly as big as when the flow was initialized. Therefore it is not reasonable to assume that the correct solution has been obtained.

Figure 6.14 shows the differences in convergence history between calculations using the Default solver and the LMNP. The results are presented for three different Mach numbers and it can be seen that as the Mach number gets closer to zero the convergence drop for the Default solver decreases. At Mach number 0.3 there is no difference in the convergence between the Default solution and the one using LMNP. The same goes for all runs made at Mach numbers higher than 0.25. Also notice that at Mach number 0.15 using the Default mode the solution converged but was not correct as can be seen in Figure 6.2 A.

Figure 6.15 present the convergence drop for six different meshes, all performed at Mach number 0.01 using the Spalart-Allmaras turbulence model. It can be observed that for the mesh with y^+ at 1 the drop is not as steep as for runs carried out on meshes with larger y^+ . This is simply because the DOF are decreasing with increasing y^+ (nodes get fewer).

In Figure 6.16 the y^+ dependence for k- ω is presented. Here it can be observed, in contrast to Spalart-Allmaras results in Figure 6.15 above, that the residual is unstable at low y^+ .

In the next figure, Figure 6.17, the differences between the No slip and Slip wall condition on the Wigley II hull is shown. The same behaviour, as observed in Figure 6.15, is also detected here where the drop is steeper for high y^+ . Observing the vertical lines that mark the convergence of the total resistance it can be concluded that since the Slip wall condition gives no negative effects on the convergence it can probably divide the time needed for a calculation by at least half using a mesh with y^+ at 120 instead of 1. That is to say if it gives solutions of the same accuracy as a No slip solution at y^+ at 1. The accuracy is discussed in Subsection 6.3.1.

Figure 6.18 presents the convergence drop for three different Mach numbers with both Spalart-Allmaras and k- ω SST as turbulence models. For the k- ω SST model at the two lowest Mach numbers large fluctuations appear after around 500 iterations. If this is an effect of using a mesh with y^+ at 1 or low Mach numbers is impossible to tell from the figures presented in this subsection. However, it has been concluded by observing Figure 6.16 and 6.18 among others that the residual from the k- ω SST model will fluctuate both at low y^+ and low Mach numbers. It seems that some of the problems can be avoided by applying the Slip wall condition for meshes with large y^+ . Note that all fluctuations occur after the final solution for the resistance is obtained.

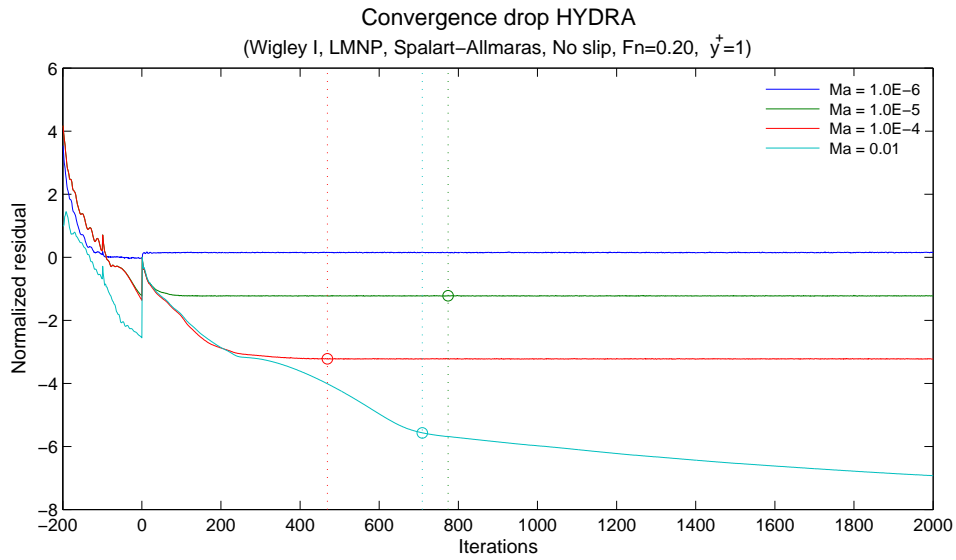


Figure 6.13: Convergence drop for 4 different runs. Two of the solutions have not converged.

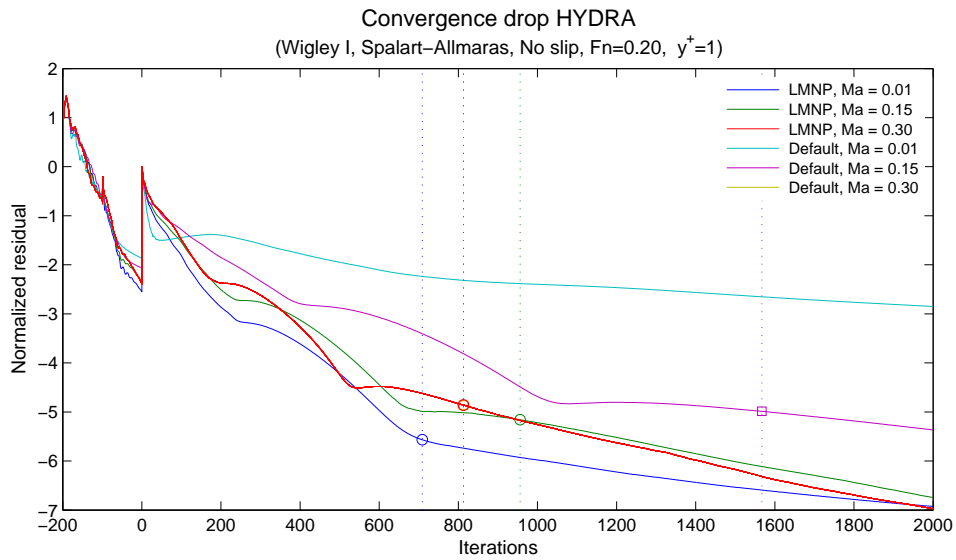


Figure 6.14: Comparison between the Default and the LMNP solver.

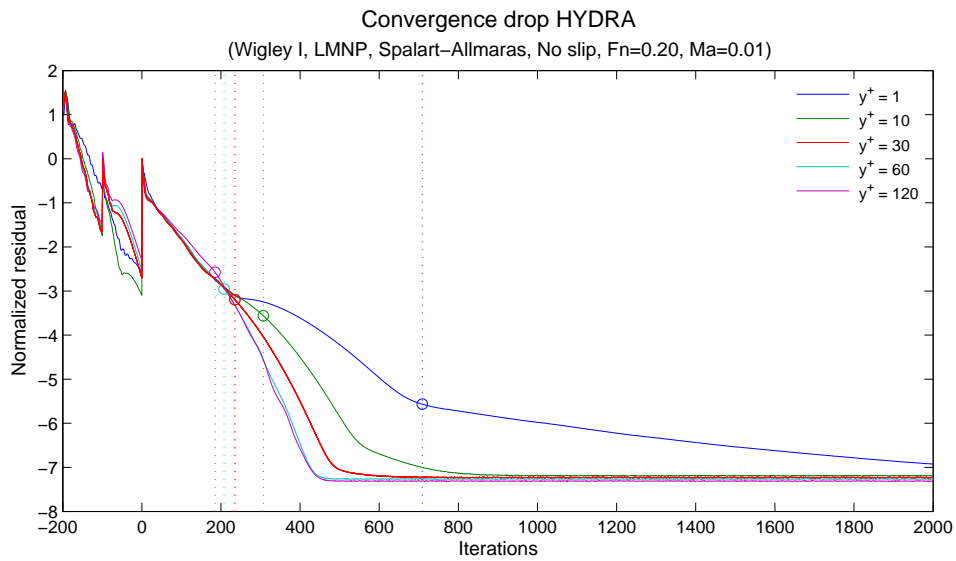


Figure 6.15: Mesh dependence on convergence drop with Spalart-Allmaras.

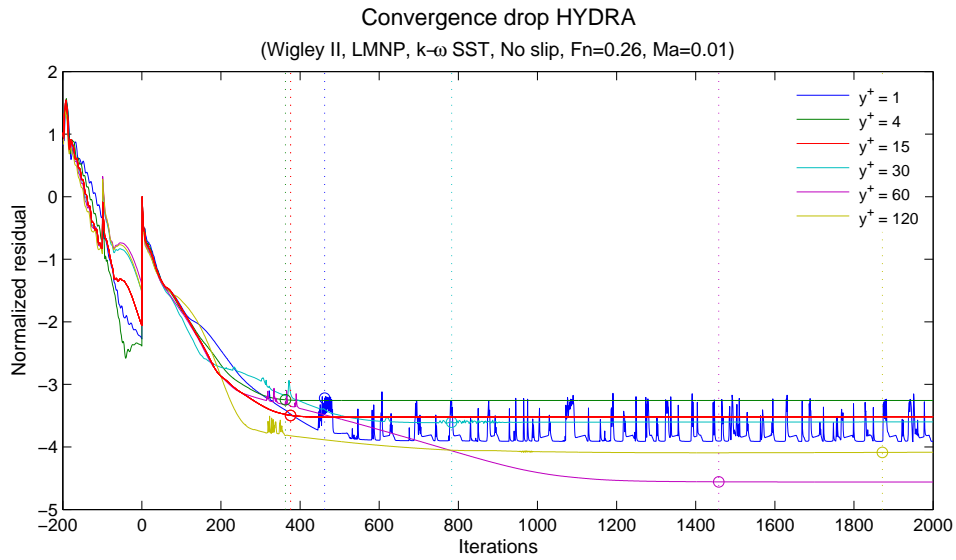


Figure 6.16: Mesh dependence on convergence drop with $k-\omega$ SST.

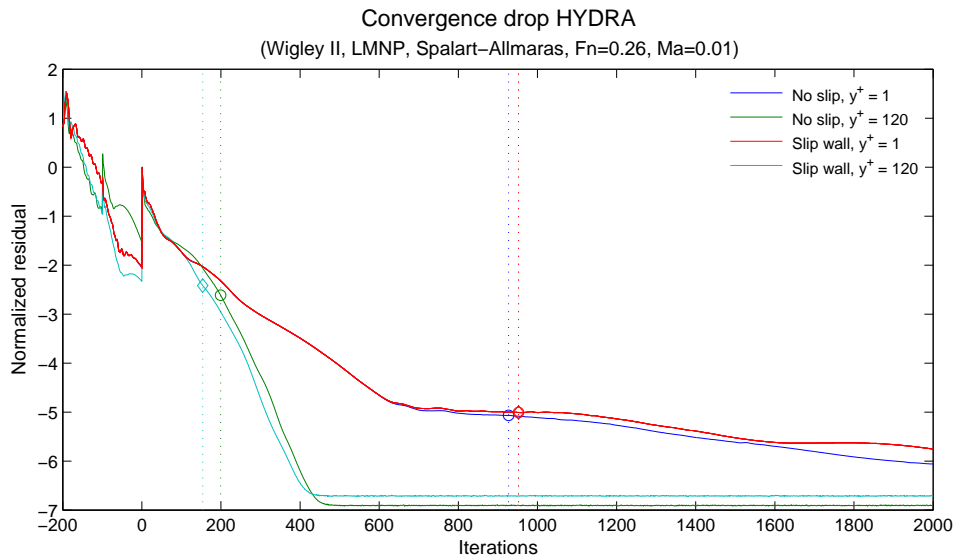


Figure 6.17: Convergence for two different cases, both performed with and without Slip wall.

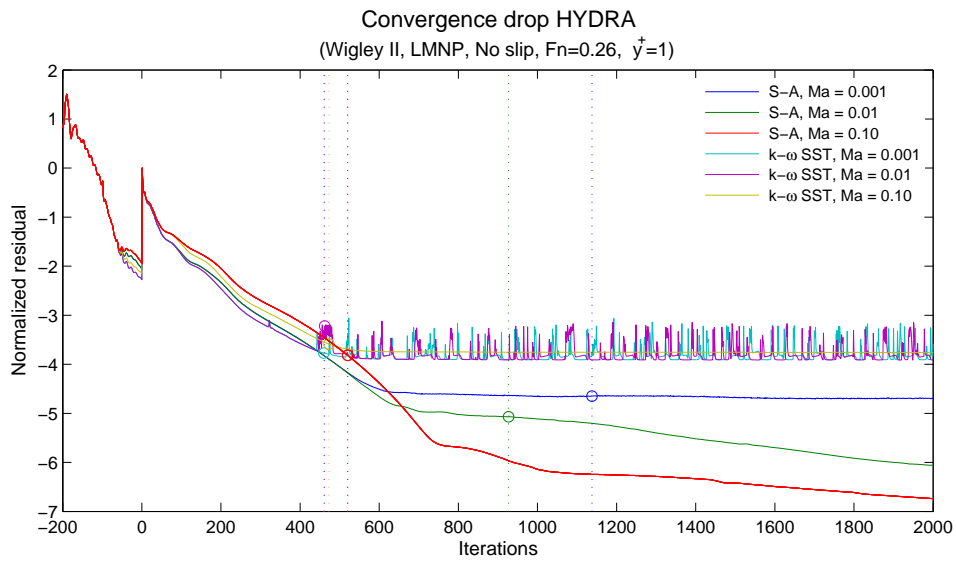


Figure 6.18: Comparison between the Spalart-Allmaras and the $k-\omega$ turbulence model.

Figure 6.19 shows convergence for the structured mesh with y^+ at 1 for various Mach numbers. The solution showed to be very “stiff” and had to be calculated for up to 20,000 iterations to ensure convergence. Even if the “drop three in magnitude” occurred relatively fast, solutions near those iterations (around 5000) showed discrepancies at the symmetry plane which took many more runs to get rid of. Further it can be concluded that higher Mach numbers converges faster and that the residual continues to decrease all the way past 20,000 iterations.

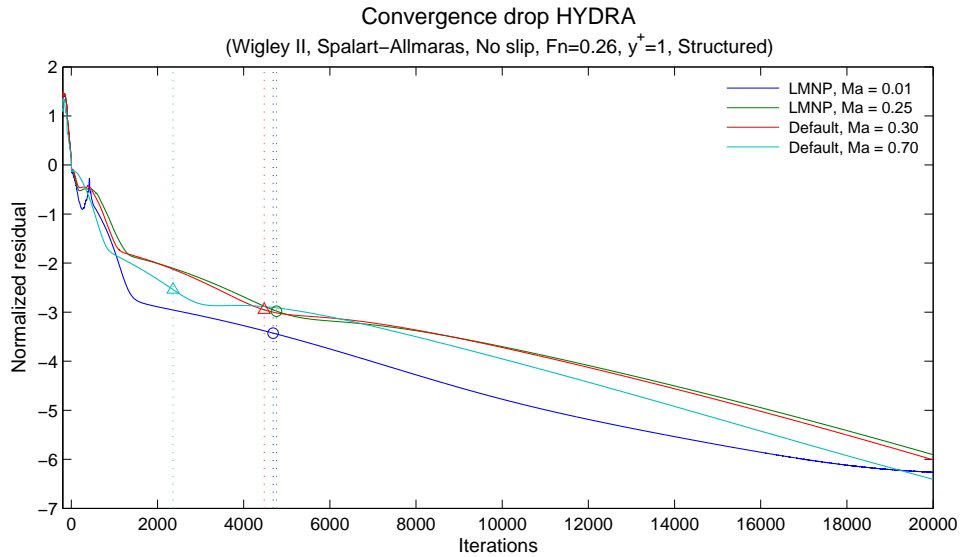


Figure 6.19: Convergence influenced by Mach number and LMNP using the structured mesh.

In Figure 6.20 the convergence for two structured meshes with y^+ at 1 and 120 using the No slip condition are compared with the y^+ at 120 mesh using the Slip wall condition. Here the DOF are the same between the two meshes (y^+ at 1 and 120) and because of that it can be concluded that it is mainly the boundary resolution that controls the convergence, since the mesh with y^+ at 120 converges much faster than the one with y^+ at 1. Between the No slip and the Slip wall there is a slight advantage towards the Slip wall, in agreement with previous results for the mixed meshes.

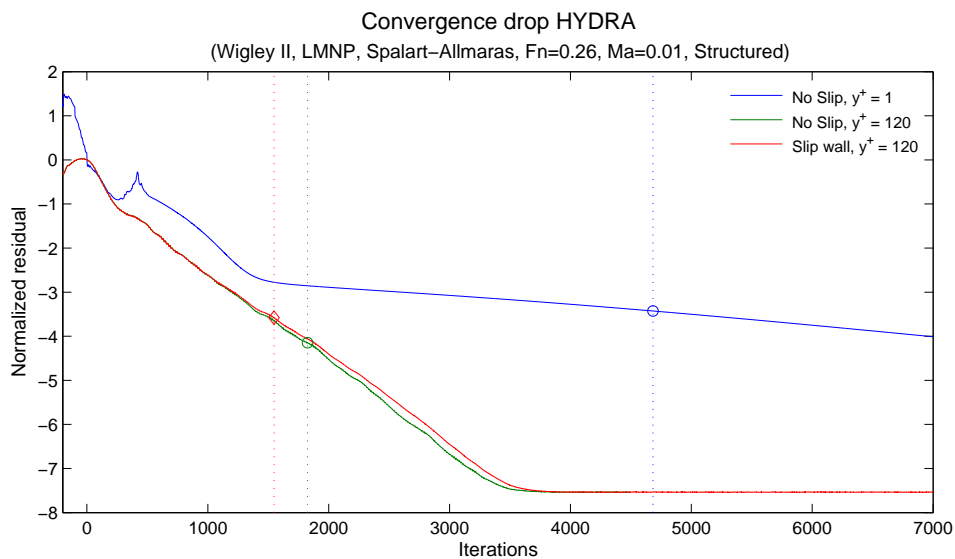


Figure 6.20: Convergence influenced by Slip wall and boundary layer resolution for the structured mesh.

6.7.2 FLUENT

Figure 6.21 A and B shows the convergence in FLUENT for Wigley II using meshes with y^+ at 1 and 60 and Spalart-Allmaras as turbulence model. In both cases it is the turbulence residual, the nut, that is “lagging behind” and for the y^+ 60 mesh it does not even drop below three in magnitude. Overall it can be concluded that the drop in HYDRA is considerably larger (since it is always the largest residual that is shown in HYDRA it can be compared to the nut directly). The drag convergence occurs at around half of the iterations for y^+ 60 mesh compared to the y^+ 1 mesh.

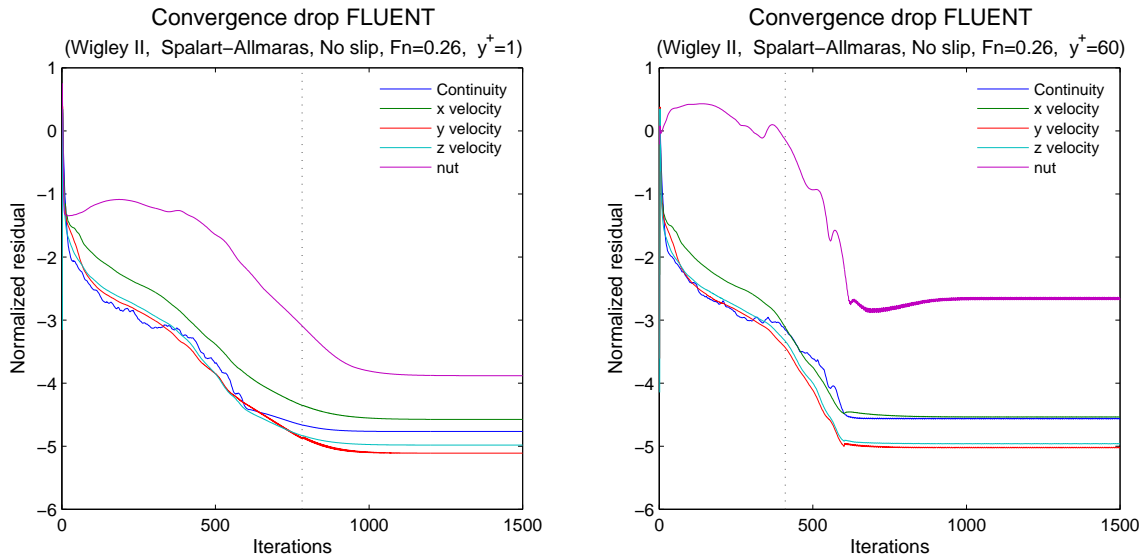


Figure 6.21 A-B: Convergence history for Wigley II with S-A as turbulence model for FLUENT. Figure A on fine grid ($y^+ = 1$) and B on coarser ($y^+ = 60$).

With the $k-\omega$ SST turbulence model the turbulence convergence in FLUENT improves significantly, see Figure 6.22 A and B where the nut has been replaced with k and ω . The other residual factors are following the same trends (and values) as in Figure 6.21.

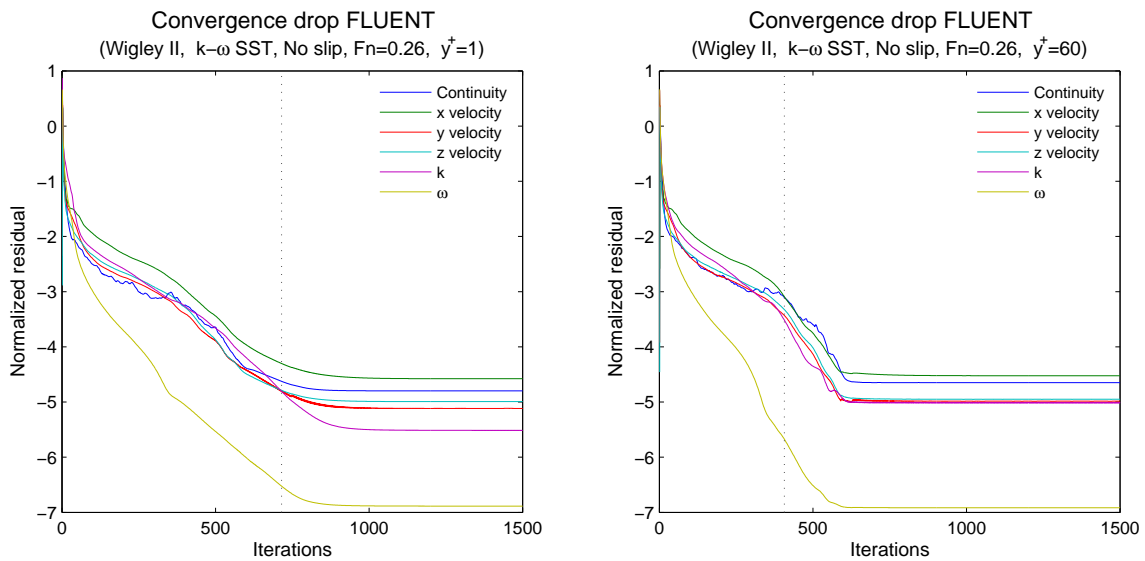


Figure 6.22 A-B: Convergence history for Wigley II with $k-\omega$ as turbulence model for FLUENT. Figure A on fine grid ($y^+ = 1$) and B on coarser ($y^+ = 60$).

6.8 CPU utilisation

6.8.1 CPU time Default vs. LMNP

In the chapter explaining the LMNP, Subsection 2.9.4, it was stated that the convergence time would decrease if the function was used on low Mach numbers while instead increase for high Mach numbers. To examine how effective, from a convergence point of view, the LMNP is on low Mach numbers, and how “ineffective” it is on high Mach numbers, a small comparison was done to estimate the convergence time versus Mach number.

As explained in Section 6.7 the total resistance was observed to determine when the solution had converged. Even if it is desirable to ensure that the largest residual have dropped three in magnitude this is not always the case for the results presented in the figures below, since the less constraint limit for resistance fluctuations (0.20%) were sometimes met before the drop of three in magnitude had occurred. However, for the stricter limit (0.01%) the residual drop always occurred first. Further it can be shown, observing Figure 6.13 found in Subsection 6.7.1, that the drop of three never occurred for some of the runs on the very lowest Mach numbers.

Figure 6.23 shows the time elapsed to convergence for the two different fluctuation limits, 0.01% (blue lines) and 0.20% (green lines), against the Mach number for the Wigley I hull. The results show that the convergence time decreases significantly if the LMNP is used on low Mach numbers. This is exactly what is expected referring to the theory. Additionally it was also stated that at high Mach numbers the LMNP should be more time-consuming, something that also can be seen. However, the differences are not very big implying that convergence time would not increase much if the LMNP was enabled at all time. Though this can be an effect of the simple geometry and the differences could be larger for other cases.

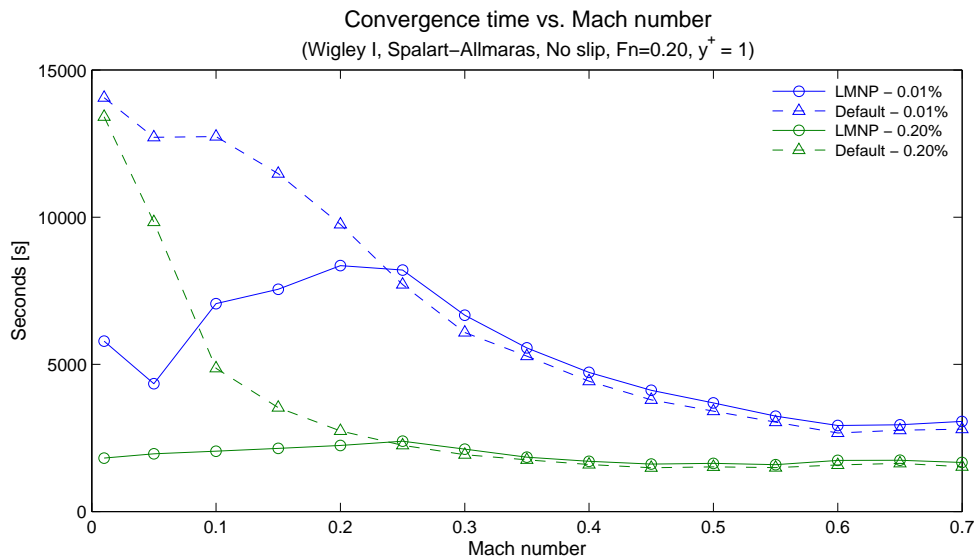


Figure 6.23: Convergence time influenced by Mach number and LMNP for Wigley I. The LMNP kicks in at Mach numbers below 0.25 and reduces the convergence time considerably.

Additionally it can be observed that for both the LMNP and the Default runs at the 0.01% fluctuation limit the convergence time experiences a drop at Mach number 0.05. With the 0.20% limit the drop disappears. It is not clear why this behaviour is observed.

To validate the results observed in Figure 6.23, for Wigley II the same plot was created for Wigley II. The results are shown in Figure 6.24 and agree well with the ones for Wigley I, though this time no dip in the convergence time is observed at any of the Mach numbers. This could be because the Mach number resolution (number of measurement points) is not as fine as for Wigley I. Further the gap between the two limits reduces significantly compared to Wigley I, which might indicate that the flow around Wigley II is more well behaved.

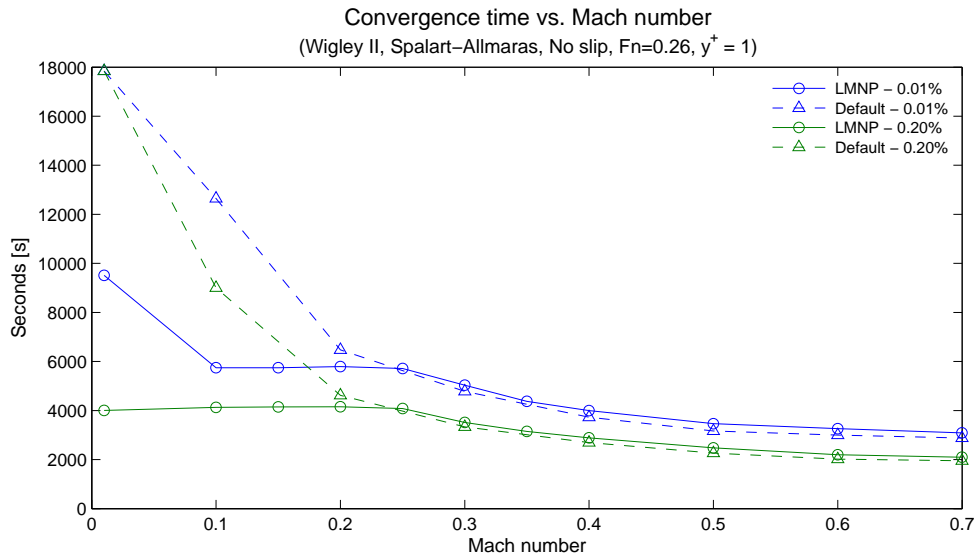


Figure 6.24: Convergence time influenced by Mach number and LMNP for Wigley II. The LMNP kicks in at Mach numbers below 0.25 and reduces the convergence time considerably.

6.8.2 CPU time vs. boundary layer resolution

The same limits as used in the previous subsection and described in Section 6.7 were applied to investigate how the boundary layer affected the convergence time. Figure 6.25 shows the time to convergence versus y^+ and DOF for Wigley II using Spalart-Allmaras at Mach number 0.01. For y^+ over 30 the time to convergence decreases with the Slip wall condition. Generally it can be concluded that a higher y^+ can save a lot of computational time. That is to say if the solution is accurate enough.

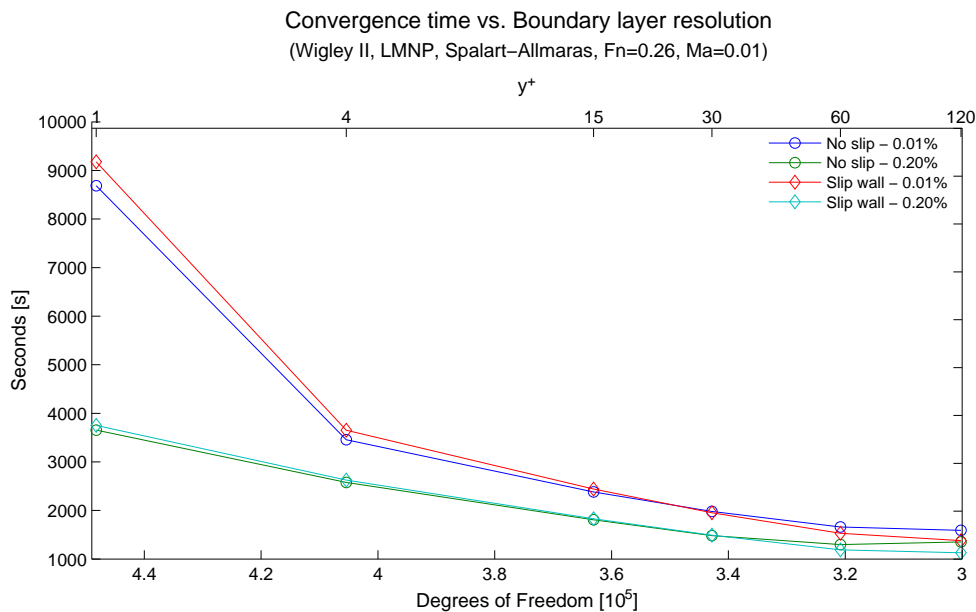


Figure 6.25: Convergence time influenced by Slip wall condition and boundary layer resolution.

6.8.3 Scalability

During this study the majority of the calculations in HYDRA have been done on eight cores while most of the FLUENT calculations were done using either one or four cores (a restriction in the licence made it impossible to run FLUENT on more than four cores simultaneously). Apart from that they have also been made on different computational clusters, HYDRA calculations on “sophy3” and FLUENT calculations on “sophy2”, and therefore on different processors. See Appendix E for further description of the clusters.

A relationship was established between time taken to calculate one iteration and number of cores used. This was done by running a number of HYDRA calculations on both sophy2 and sophy3 using one to eight cores. All calculations ran to 2000 iterations and then a mean value per iteration was established simply by dividing the total time with 2000.

In Figure 6.26 the relationships between number of cores and the time taken to complete one iteration is presented. It is clearly visible that the time it takes to complete one iteration in HYDRA is considerably larger than in FLUENT. However this does not mean anything since the two codes do different things during their iterations, see Section 2.8, and it is rather the time to convergence that has to be compared. Additionally it can also be noted that the processors on sophy3 are faster than the ones on sophy2.

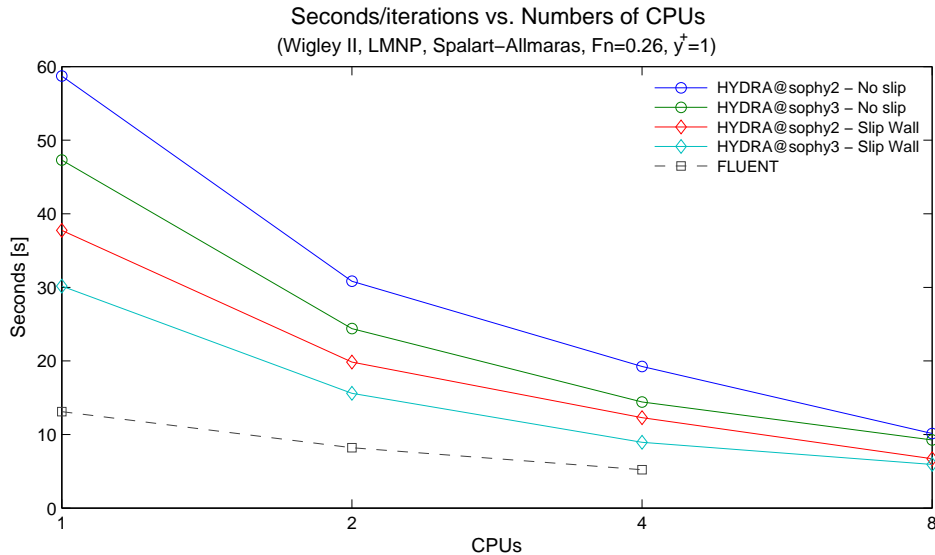


Figure 6.26: Seconds to complete one iteration for different runs and CPU's.

A quick look at Figure 6.26 above could give the impression that HYDRA is significant better at utilise multiple cores. Even if this is the case the improvement is not as big as it seems to be. Figure 6.27 shows the actual gain in speed up as the number of cores is doubled.

From Figure 6.26 it can be established that to scale the results from 8 cores on sophy3 to one core on sophy2 it has to be multiplied by a factor of 6.35. To instead scale the results to 4 cores on sophy2 the factor is 2.07. These factors have been validated against other runs and the given values have shown acceptable agreement.

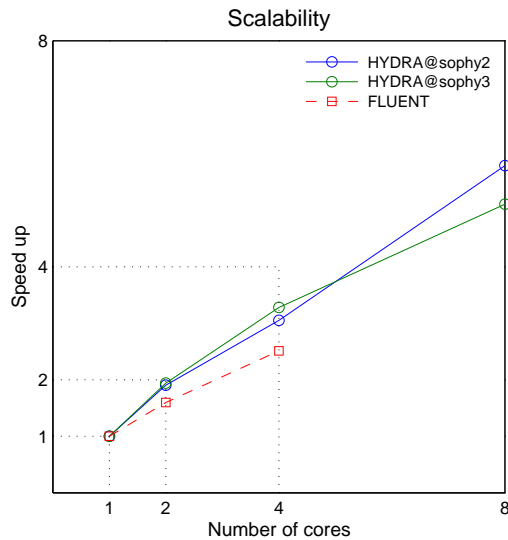


Figure 6.27: Scalability between HYDRA and FLUENT, as well CPUs on Sophy2 and Sophy3.

6.8.4 CPU time HYDRA vs. FLUENT

In the previous subsection it was mentioned that the HYDRA and FLUENT calculations have been performed on different computational clusters. For a fair comparison between codes two cases were chosen and remade in HYDRA on the same server used for FLUENT. The two cases were Wigley II meshes with y^+ at 0.5/1 and y^+ at 60/120, $Fn = 0.26$ and $Ma = 0.01$ (only valid for HYDRA) with Spalart-Allmaras as turbulence model.

The convergence criteria were the total resistance using the stricter fluctuation limit of 0.01%. Both cases were computed using first one and then four cores. By multiplying the iterations taken to reach convergence with the time taken to complete one iteration, as presented in Figure 6.26 in the previous subsection, the total convergence time was determined. Results are presented below in Table 6.2.

Table 6.2: CPU time, HYDRA vs. FLUENT, using mixed meshes with y^+ at 1 and 60.

		DOF	1 core	4 cores
$y^+ = 1$	HYDRA	448,223	60,294 s	19,756 s
	FLUENT	1,364,640	10,305 s	4,086 s
$y^+ = 60$	HYDRA	300,190	9,586 s	3,121 s
	FLUENT	1,073,401	4,623 s	1,746 s

As it can be seen in the table above FLUENT is much faster than HYDRA, even if the DOF are more than three times larger in FLUENT (for a more detailed comparison between the meshes see Table 3.6 in Section 3.4). This can be explained by that in these cases where the flow is subsonic and rather simple (due to the geometry) the pressure field controls the convergence, hence a segregated solver (like SIMPLE used in FLUENT) is a natural choice. If instead the geometry had been more complex and most important the speed higher HYDRA is expected to perform better.

7 Conclusions

From Section 6.2, Mach number dependence, it could be concluded that HYDRA's predictions with the mixed meshes becomes more accurate as the Mach number decreases (compared to FLUENT and the structured results), i.e. for these cases HYDRA will produce the most accurate solution in the low Mach number range using the LMNP. However the increase in resistance towards Mach number 0.25, seen in Figure 6.2 A and Figure 6.3 A, indicates that the solver struggles with unstructured meshes. The slope of the curve is worrying when a problem contains high velocity gradients, e.g. in a jet turbine with a cooling system. It would mean that solutions in different parts of the problem become inconsistent between each other. For marine use the slope of the curve is not as worrying since in most cases the velocity remains fairly constant. For HYDRA's defence it should be mentioned that the code is constructed for structured meshes where this issue disappears.

Comparing the curves between the two hulls, Figure 6.2 A and Figure 6.3 A, it can be seen that their slope differs; further indicating that there is either a mesh or geometry effect. As mentioned in Section 3.4 the meshes for the two hulls are slightly different, both in DOF and form. This means that if one wants to perform e.g. an optimisation study results may not be consistent between different cases.

Apart from the problems that HYDRA displays in the low Mach number range it can also be concluded, from Figure 6.4 A-C and Figure 6.6 A-C – observing the viscous and pressure contributions separately, that the wall function in HYDRA is not as reliable for higher y^+ as the one in FLUENT. The Slip wall in HYDRA improved the separate prediction of the viscous and pressure contributions, but not to the same standard as FLUENT when using the unstructured meshes.

Possible error sources for the mixed/unstructured meshes can be; DOF not large enough, skewed cells from the cusp angle at bow and stern, bad resolution in the wake or that unstructured meshes are in general more diffusive. For now an unstructured Mesh can only be used with caution at low Mach numbers (down to 10^{-3}) and preferably low y^+ . Higher y^+ can be used if the total resistance, rather than the decomposition into viscous and pressure contributions, is of interest.

With the structured mesh the DOF in HYDRA and FLUENT is almost equal, i.e. the node to cell ratio for the mesh is almost one. This gave a more fair comparison between the two codes and the results indicate that HYDRA performs well with a structured mesh.

Over a Froude number range HYDRA shows good agreement with the experimental data from Ju [11] according to Figure 6.10. No inconsistency can be seen between the Default and LMNP modes.

Measurements of the CPU time for LMNP vs. Default at the higher Mach numbers indicate that LMNP can be used at all time without compromising the convergence or computational time. Though, this would need further studies using different geometries. CPU time comparisons between coarse and dense boundary layers (small and large y^+) indicates that there is a possibility to save considerable computational time with a coarse boundary layer. However, this requires some additional work on the Slip wall function if the same accuracy as for using a mesh with y^+ at 1 is required.

When comparing CPU time between HYDRA and FLUENT for these type of cases FLUENT comes out as the winner, but on the other hand that is expected.

8 Further work

As this study only was meant as a first step to investigate HYDRA's marine capabilities some questions still remains. The most important thing to further address is the issues HYDRA displays with unstructured meshes, e.g. the inconsistency in the low Mach number range with the LMNP and the odd distribution between pressure and viscous forces with an increasing. This should preferably be done using even simpler cases to enable meshes with low skewness (e.g. no cusp edges). Since there are additional versions of HYDRA which are better calibrated for unstructured cells it is recommended to use them and repeat some of the calculations in this study (with the existing Wigley meshes) for further validation. It is also recommended to perform a more thorough investigation o the Slip wall function, using a hull/shape that makes the flow separate.

9 References

- [1] 24.8.1 SIMPLE vs. SIMPLEC. (n.d.). Retrieved April 2010, from <http://jullio.pe.kr/fluent6.1/help/html/ug/node847.htm>
- [2] Anderson, J. D. (1995). *Computational Fluid Dynamics – The Basics with Applications*. McGraw-Hill.
- [3] Anderson, J. D. (2001). *Fundamental of Aerodynamics* (Third ed.). Singapore: McGraw-Hill.
- [4] Andersson, B., Andersson, R., Håkansson, L., Mortensen, M., Sudiyo, R., & Van Wachem, B. (2009). *Computational Fluid Dynamics for Chemical engineers* (Fifth ed.). Gothenburg, Sweden.
- [5] ANSYS FLUENT 12.0 Theory Guide. (2009). ANSYS Inc.
- [6] ANSYS FLUENT 12.0 User's Guide. (2009). ANSYS Inc.
- [7] Bardina, J. E., Huang, P. G., & Coakley, T. J. (1997). *Turbulence Modeling Validation, Testing and Development*. NASA-TM-110446, Ames Research Center, Moffett Field.
- [8] Bird, R. B., Stewart, W. E., & Lightfoot, E. N. (1960). *Transport Phenomena*. Wisconsin: John Wiley & Sons.
- [9] Ferziger, J. H., & Peric, M. (2002). *Computational Methods for Fluid Dynamics* (Third ed.). Berlin Heidelberg, Germany.
- [10] Journée, J. M. (1992). *Experiments and Calculations on 4 Wigley Hull Forms in Head Waves*. Report no. 0909, Delft University of Technology, Ship Hydromechanics Laboratory.
- [11] Ju, S. (1983). *Study of Total and Viscous Resistance for the Wigley Parabolic Ship form*. Report no. 261, Iowa Institute of Hydraulic Research, Iowa.
- [12] Larsson, L., & Raven, H. C. (2004). *Ship Resistance and Flow*. Gothenburg and Wageningen.
- [13] Mavriplis, D. J. *Revisiting the Least-Squares Procedure for Gradient Reconstruction on Unstructured Meshes*. VA 23666, National Institute of Aerospace, Hampton.
- [14] Moinier, P. (1999). *Algorithm Developments for an Unstructured Viscous Flow Solver*. St Hughs College. Trinity Term.
- [15] Spalart, P. R., & Allmaras, S. R. (1992). A One-Equation Turbulence Model for Aerodynamic Flows. AIAA-92-0439.
- [16] Sutherland, W. (1893). The viscosity of gases and molecular force. *Philosophical Magazine*, pp. 507-531.
- [17] *The HYDRA User's Guide* (Version 6.1.7-beta ed.). (2009). Rolls-Royce plc.
- [18] *ThermExcel*. (n.d.). Retrieved February 2010, from http://www.thermexcel.com/english/tables/eau_atm.htm

- [19] Tristante, I. T. (2004). *A Mesh Transparent Numerical Method for Large-eddy Simulation of Compressible Turbulent Flows*. PhD Thesis, Loughborough University.
- [20] Versteeg, H. K., & Malalasekera, W. (1995). *An introduction to Computational Fluid Dynamics, The finite volume method*. Addison Wesley Longman Limited.
- [21] White, F. M. (2006). *Fluid Mechanics* (Sixth ed.). McGraw-Hill.
- [22] Øye, G. Å. (2009). *CFD validation UT731CD*. Report RRM-R&T_09-008, Rolls-Royce Marine, R&T, Ulsteinvik.

Appendix A – Calculations

Calculating boundary layer properties

These approximations, built on empirical results, are not always suitable to use closest (near) to the wall but works well for the outer parts of the boundary layer.

Table A.1: Input parameters for boundary layer calculations

	Wigley I	Wigley II
V_S [m/s]	1.0855	1.4212
L [m]	3.000	3.048
ν [m ² /s]	$1.002 \cdot 10^{-6}$	$1.047 \cdot 10^{-6}$

As a first step the length of the laminar boundary layer is calculated. It is assumed that the flow should behave laminar until the critical Reynolds number is reached, i.e. when turbulence starts to develop. This number is normally around $5 \cdot 10^5$ for flows along surfaces, and so in this case too. That means that the laminar boundary layer length is assumed to be

$$x_{crit} = \frac{Re_{crit} \cdot \nu}{V_S} \quad (A.1)$$

E.g., for Wigley I Equation (A.1) gives that the first 0.46 m, of approximately 3 m (disregarding hull curvature), will experience laminar flow and the rest, 2.54 m, turbulent flow. In other words the first 15.4% of the boundary layer is laminar. For Wigley II the corresponding part is 12.1%.

To determine how thick the boundary layer should be made in the mesh the boundary layer thickness has to be calculated. For that Equation (A.2) – (A.4) is used.

$$n = \log(Re) \quad (A.2)$$

$$\theta = 0.036 \frac{x}{\sqrt[5]{Re_x}} \quad (A.3)$$

$$\frac{\theta}{\delta} = \frac{n}{(1+n)(2+n)} \quad (A.4)$$

As a first step the variable n and the momentum thickness, θ , are calculated, where n depends on the pressure gradient and to some extent on the Reynolds number but is normally approximated by Equation (A.2) [12]. The momentum thickness has been calculated in the aft of the ship ($x = 3$ for Wigley I) where the momentum, and hence the boundary layer thickness should be largest. By using Equation (A.4) the boundary layer thickness can be estimated to 52.9 mm for Wigley I and 51.7 mm for Wigley II.

To determine where the first grid point should be located, the local skin friction coefficient has to be calculated. This is done through the power law approximation.

$$C_f = \frac{0.058}{\sqrt[5]{Re_x}} \quad (A.5)$$

With the local skin friction coefficient the friction velocity can be calculated as

$$u_\tau = V_S \sqrt{\frac{C_f}{2}} \quad (\text{A.6})$$

By using Equation (A.7) the distance to any given y^+ can be calculated. And in that way the first layers of grid points from the wall can be placed at a wished y^+ .

$$y = \frac{\nu y^+}{u_\tau} \quad (\text{A.7})$$

Scaling output from HYDRA

To be able to extract resistance/forces from HYDRA a “force monitor” had to be implemented manually in the input file, see HYDRA [17]. The force monitor was set to write the integrated pressure and viscous resistance for a chosen surface to a user specified file during each iteration. Because the STP2 scaling mode was used when the data was fed into the code the output became scaled in the same way, i.e. to get actual forces the nondimensional had to be scaled back. How this was done is described below.

Generally a force coefficient is defined as

$$C_d = \frac{F}{\frac{1}{2} \cdot \rho \cdot U^2 \cdot S} \quad (\text{A.8})$$

where

F – Force

ρ – Density

U – Freestream velocity

S – Wetted surface area

Between cases with the same Reynolds number C_d is constant, this gives the following connection

$$\frac{F^*}{\frac{1}{2} \cdot \rho^* \cdot U^{*2} \cdot S^*} = C_d = \frac{F}{\frac{1}{2} \cdot \rho \cdot U^2 \cdot S} \quad (\text{A.9})$$

Since $S^* = S$, following from $L^* = L$, and $\rho^* = 1$ this leaves us with

$$F = F^* \cdot \frac{U^2 \cdot \rho}{U^{*2}} \quad (\text{A.10})$$

and

$$C_d = \frac{F^*}{\frac{1}{2} \cdot U^{*2} \cdot S} \quad (\text{A.11})$$

Wigley I experimental results

This text explains how the wave resistance for the Wigley I Hull was extracted from the measurements in Journée [10] using methods from ITTC-57 and Watanabe. As a first step the total (including wave making and breaking) ship resistance coefficient was calculated according to Equation (A.12).

$$C_T = \frac{R_t}{\frac{1}{2} \cdot \rho \cdot V^2 \cdot S} \quad (\text{A.12})$$

where

$$\begin{aligned} R_t &= 5.98 \text{ N} && \text{(Total resistance)} \\ \rho &= 998 \text{ kg/m}^3 && \text{(Density of water in towing tank)} \\ V &= 1.085441 \text{ m/s} && \text{(Ship speed at Fn=0.2)} \\ S &= 1.956 \text{ m}^2 && \text{(Wetted surface)} \end{aligned}$$

To separate the wave part from C_T the two following equations were used, Equation (A.13) – ITTC-57 and Equation (A.14) – Watanabe

$$C_f = \frac{0.075}{(\log_{10}(Re) - 2)^2} \quad (\text{A.13})$$

$$k = -0.095 + 25.6 \frac{C_b}{\left(\frac{L}{B}\right)^2 \cdot \sqrt{\frac{B}{d}}} \quad (\text{A.14})$$

where

$$\begin{aligned} Re &= 3.25 \cdot 10^6 && \text{(Reynolds number from Wigley I test case)} \\ C_b &= 0.56 && \text{(Box coefficient)} \\ L &= 3 \text{ m} && \text{(Ship length)} \\ B &= 0.6 \text{ m} && \text{(Beam of the ship)} \\ d &= 0.1875 \text{ m} && \text{(Draught)} \end{aligned}$$

The residuary force which is essentially the wave resistance was then calculated with the following equation

$$C_R = C_T - (1 + k)C_f \quad (\text{A.15})$$

and the residuary contribution to the total part was then estimated by Equation (A.16).

$$fraction = \frac{C_R}{C_T} \quad (\text{A.16})$$

This gives a wave resistance contribution of 13.12% and the remaining 86.88% is the pressure and viscous resistance. Hence for Wigley I the remaining resistance to be compared with the CFD calculations is

$$5.98 \cdot 0.8688 = 5.2 \text{ N}$$

Appendix B – Corrections

Correction Wigley II

A mistake, affecting all Wigley II calculations, was discovered at a very late state in the project when there was no time left for corrections. The fault was that the wrong hull length had been used (3 m instead of the correct 3.048 m) when calculating the reference viscosity for the STP2 scaling. Luckily the nature of the mistake made it consistent between all calculations and all “trends” observed is still valid. Although it resulted in a minor error of which the extent is explained below.

From Equation (4.13) in Subsection 4.2.2, explaining the STP2 scaling, we have the reference viscosity

$$\mu_{ref0}^* = \mu^* = \frac{Ma\sqrt{\gamma} \cdot L}{Re_w} \quad (B.1)$$

where Re_w is the Reynolds number from the test case and therefore the one strived for in the simulation. From Section 3.2 we know that $Re_w = 4,135,663$

$$\frac{\mu_{ref0_correct}^*}{\mu_{ref0_wrong}^*} = 1.02 \quad (B.2)$$

As shown, by using the wrong length, L , in Equation (B.1), above, the reference viscosity, μ_{ref0}^* , needed to reach the desired Reynolds number got underestimated by about 2%. This meant that the Reynolds number present during the calculations also was underestimated by 2%.

$$Re = \frac{Ma\sqrt{\gamma} \cdot L}{\mu^*} \quad (B.3)$$

$$\frac{Re_{correct}}{Re_{wrong}} = 1.02 \quad (B.4)$$

As can be seen from the equations the error at this stage is linear but to make sure that the error did not grow during the calculation, comparisons were done between one old, and miscalculated, solutions and one new calculation using the correct values.

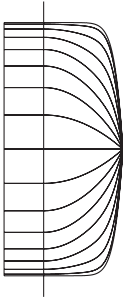
$$\frac{C_{p_correct}}{C_{p_wrong}} = 1.001312 \quad (B.5)$$

$$\frac{C_{v_correct}}{C_{v_wrong}} = 1.002496 \quad (B.6)$$

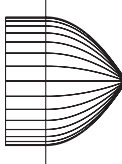
$$\frac{C_{t_correct}}{C_{t_wrong}} = 1.002414 \quad (B.7)$$

These results shows that the error stays below 0.25% and the conclusion would be that it is well within an acceptable range and the results are still valid.

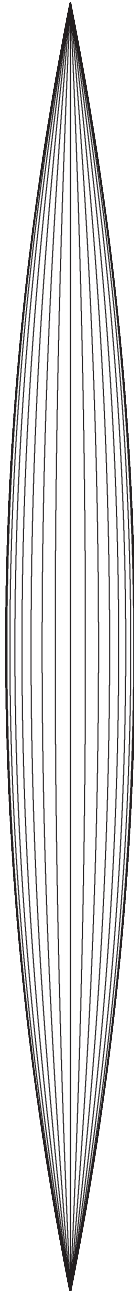
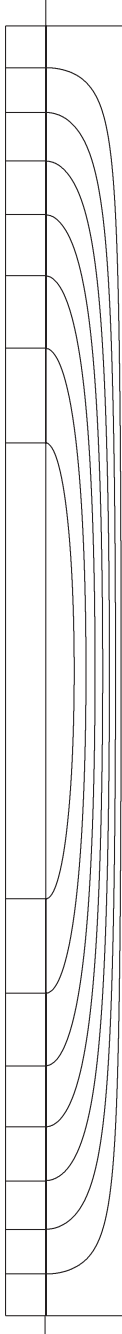
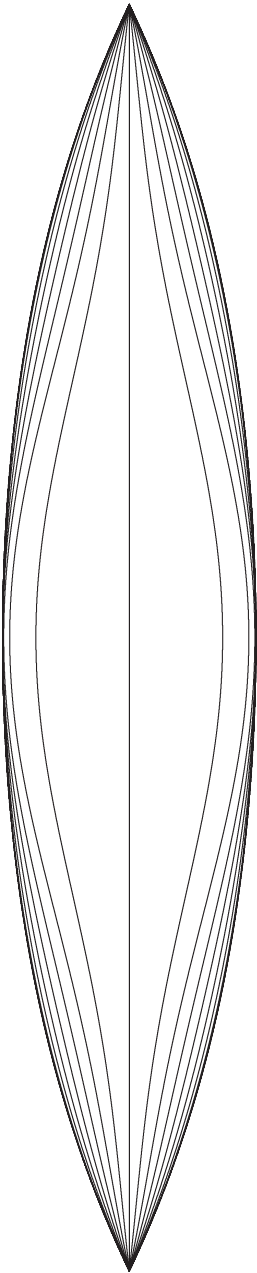
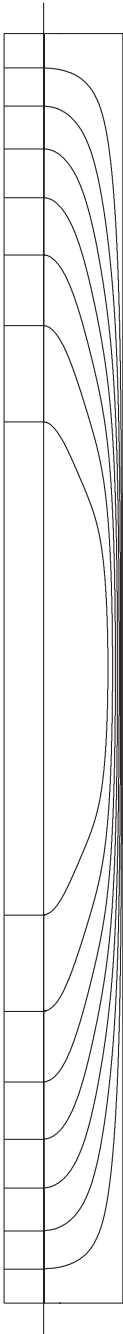
Appendix C - Line drawings



Wigley I

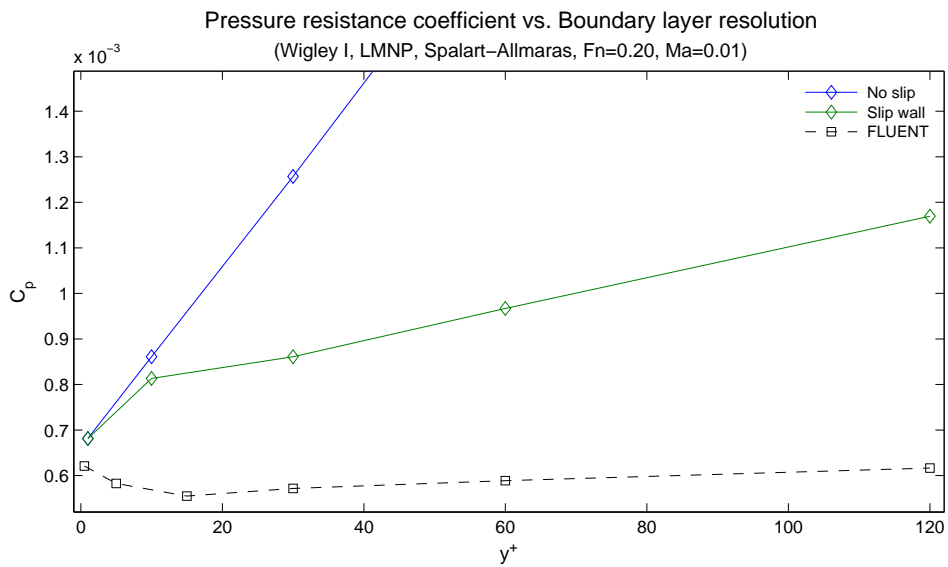
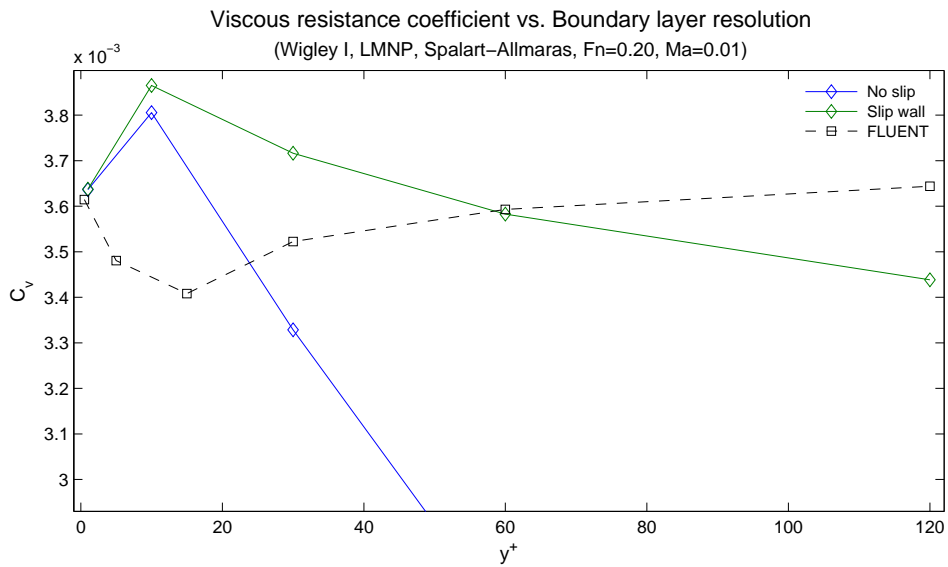
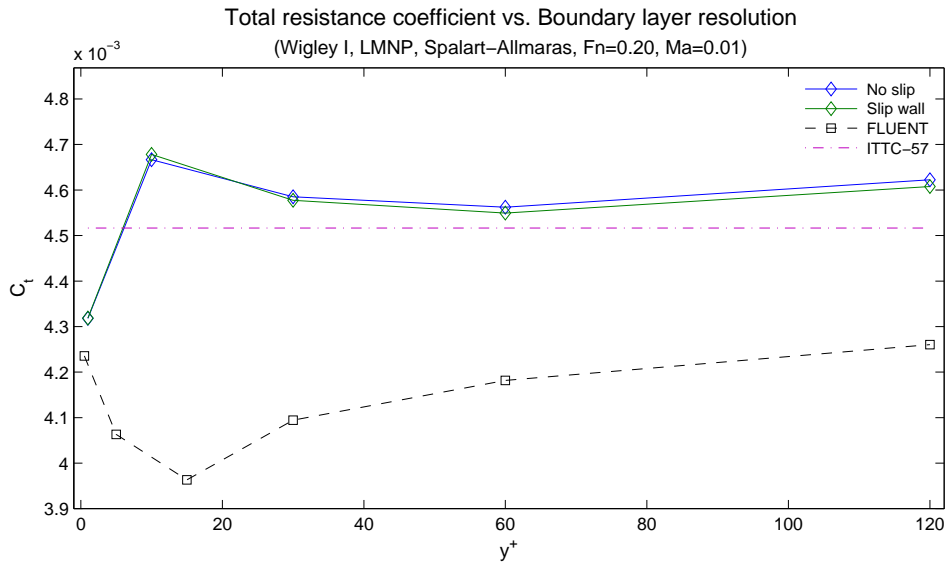


Wigley II



Appendix D – Figures

Additional results – Wigley I



Appendix E – Tables

Table E.1: Table of runs made with Wigley I hull in HYDRA.

Input variables				Mesh					
Mode	Turb. model	Hull boundary	Mach No	0.5/1	5/10	15/30	30/60	60/120	120/240
Default			0,010000	x	x	x	x	x	x
			0,050000	x	x	x	x	x	x
			0,100000	x	x	x	x	x	x
			0,150000	x	x	x	x	x	x
			0,200000	x	x	x	x	x	x
			0,250000	x	x	x	x	x	x
			0,300000	x	x	x	x	x	x
			0,350000	x					
			0,400000	x					
			0,450000	x					
			0,500000	x					
			0,550000	x					
			0,600000	x					
			0,650000	x					
LMNP	S-A	Viscous wall	0,700000	x					
			0,000001	x					
			0,000010	x					
			0,000100	x					
			0,001000	x					
			0,002000	x					
			0,004000	x					
			0,006000	x					
			0,008000	x					
			0,010000	x	x	x	x	x	x
			0,050000	x	x	x	x	x	x
			0,100000	x	x	x	x	x	x
			0,150000	x	x	x	x	x	x
			0,200000	x	x	x	x	x	x
			0,250000	x	x	x	x	x	x
			0,300000	x	x	x	x	x	x
			0,350000	x					
			0,400000	x					
		0,450000	x						
		0,500000	x						
		0,550000	x						
		0,600000	x						
0,650000	x								
0,700000	x								
		Slip wall	0,010000	x	x	x	x	x	x

Table E.2: Table of runs made with Wigley II hull in HYDRA

		Input variables			Mesh										
Mode	Turb. model	Hull boundary	Mach No	Fn	0.5/1	2/4	7.5/15	15/30	30/60	60/120	0.5/1-S	60/120-S			
Default			0,2000	0,26	x										
			0,3000	0,26	x										
			0,4000	0,26	x										
			0,5000	0,26	x										
			0,6000	0,26	x										
			0,7000	0,26	x										
LMNP	S-A	Viscous wall	0,0010	0,26	x	x	x	x	x	x	x				
			0,0100	0,26	x	x	x	x	x	x	x	x	x		
			0,1000	0,24	x										
			0,1000	0,26	x										
			0,1000	0,28	x										
			0,1000	0,30	x										
			0,1000	0,32	x										
			0,1500	0,26	x										
			0,2000	0,26	x										
			0,2500	0,26	x										
			0,3000	0,26	x								x		
			0,3000	0,24	x										
			0,3000	0,26	x										
			0,3000	0,28	x										
			0,3000	0,30	x										
			0,3000	0,32	x										
			0,3500	0,26	x										
			0,4000	0,26	x										
			0,5000	0,26	x										
			0,6000	0,26	x										
			0,7000	0,26	x								x		
					Slip wall	0,0010	0,26	x	x	x	x	x	x		
						0,0100	0,26	x	x	x	x	x	x		
						0,1000	0,26	x	x	x	x	x	x		
LMNP	k- ω SST	Viscous wall	0,0010	0,26	x	x	x	x	x	x					
			0,0100	0,24	x										
			0,0100	0,26	x	x	x	x	x	x		x			
			0,0100	0,28	x										
			0,0100	0,30	x										
			0,0100	0,32	x										
			0,1000	0,26	x	x	x	x	x	x	x				
			0,3000	0,24	x										
			0,3000	0,26	x										
			0,3000	0,28	x										
			0,3000	0,30	x										
			0,3000	0,32	x										
				Slip wall	0,0010	0,26	x	x	x	x	x	x			
					0,0100	0,26	x	x	x	x	x	x			
					0,1000	0,26	x	x	x	x	x	x			

Table E.3: Wigley I and II operating conditions.

		Wigley I	Wigley II
Length	L	3 m	3.048 m
Density	ρ	998 kg/m ³	998.623 kg/m ³
Viscosity	μ	0.001 kg/ms	0.001046 kg/ms
Gravity	g	9.82 m/s ²	9.803 m/s ²
Froude number	Fn	0.2	0.26
Velocity	u	1.085541 m/s	1.421217 m/s
Reynolds number	Re	3250111	4135663
Gas property	γ	1.4	1.4

Table E.4: Reference viscosities and velocities after scaling.

Mach	Wigley I		Wigley II	
	μ_{ref}	u^*	μ_{ref}^1	u^*
0.000001	1.092E-12	1.183E-06	8.720E-13	1.183E-06
0.000010	1.092E-11	1.183E-05	8.720E-12	1.183E-05
0.000100	1.092E-10	1.183E-04	8.720E-11	1.183E-04
0.001000	1.092E-09	1.183E-03	8.720E-10	1.183E-03
0.002000	2.184E-09	2.366E-03	1.744E-09	2.366E-03
0.004000	4.369E-09	4.733E-03	3.488E-09	4.733E-03
0.006000	6.553E-09	7.099E-03	5.232E-09	7.099E-03
0.008000	8.737E-09	9.466E-03	6.976E-09	9.466E-03
0.010000	1.092E-08	1.183E-02	8.720E-09	1.183E-02
0.050000	5.461E-08	5.916E-02	4.360E-08	5.916E-02
0.100000	1.092E-07	1.183E-01	8.720E-08	1.183E-01
0.150000	1.638E-07	1.775E-01	1.308E-07	1.775E-01
0.200000	2.184E-07	2.366E-01	1.744E-07	2.366E-01
0.250000	2.730E-07	2.958E-01	2.180E-07	2.958E-01
0.300000	3.276E-07	3.550E-01	2.616E-07	3.550E-01
0.350000	3.823E-07	4.141E-01	3.052E-07	4.141E-01
0.400000	4.369E-07	4.733E-01	3.488E-07	4.733E-01
0.450000	4.915E-07	5.324E-01	3.924E-07	5.324E-01
0.500000	5.461E-07	5.916E-01	4.360E-07	5.916E-01
0.550000	6.007E-07	6.508E-01	4.796E-07	6.508E-01
0.600000	6.553E-07	7.099E-01	5.232E-07	7.099E-01
0.650000	7.099E-07	7.691E-01	5.668E-07	7.691E-01
0.700000	7.645E-07	8.283E-01	6.104E-07	8.283E-01

¹ This is the correct μ_{ref} using L = 3.048

Table E.5: Properties and performance of Sophy2 and Sophy3.

	Sophy2	Sophy3
Processor	Intel(R) Core(TM)2 Quad CPU	Intel(R) Xeon(R) CPU
CPU family	6	6
Model	15	23
Stepping	7	10
Type	64-bit	64-bit
Core speed	2.40 GHz	2.50 GHz
Cache size	4096 KB	6144 KB
CPU cores	4	4
FPU	Yes	Yes

Appendix F - Hull generation

Fortran code for Wigley hull generation

```
C Wigley hull
program wigley
implicit none
real*8 alfa, B, L, D, Dr, Lr, x(3001), y(3001,188), z(188)
real*8 yy(1000), zz
integer i, j, r, s, Lstep, Dstep
alfa = 1
x(1) = -1
B = 0.6
L = 3.0
D = 0.1875
Lstep = 1000
Lr = 500
Dstep = 65
Dr = 65
open(unit=10,file="hull.dat",status='unknown')
do i=1,Lstep
z(1) = 0
do j=1,Dstep
Y(i,j) = (1-z(j)**2)*(1-x(i)**2)*(1+0.2*x(i)**2)+alfa*z(j)
&**2*(1-z(j)**8)*(1-x(i)**2)**4
write(10,*)x(i),y(i,j),z(j)
z(j+1) = z(j)+1/Dr
end do
x(i+1) = x(i)+1/Lr
end do
close(10)

c Create array for a finer grid at large curvature
open(unit=20,file="curvature.dat",status='unknown')
do i=200,801
zz = 0.1275/0.1875
yy(i) = (1-zz**2)*(1-x(i)**2)*(1+0.2*x(i)**2)+alfa*zz
&**2*(1-zz**8)*(1-x(i)**2)**4
write(20,*)x(i)*L/2,yy(i)*B/2,zz*D
end do
close(20)

c Adding dimensions
open(unit=30,file="hull_dim.dat",status='unknown')
do i=1,Lstep+1
x(i)=x(i)*L/2
do j=1,Dstep+1
y(i,j)=y(i,j)*B/2
write(30,*)x(i),y(i,j)
end do
end do
do j=1,Dstep+1
z(j)=z(j)*D
write(30,*)z(j)
end do
close(30)
```

```

c Create STL-file for ss02 and GAMBIT
open(unit=40,file="solid.stl",status='unknown')
write(40,*)'solid'
do i=1,Lstep
  do j=1,Dstep
    write(40,*)'facet'
    write(40,*)'outer loop'
    write(40,*)'vertex ', x(i), y(i,j), z(j)
    write(40,*)'vertex ', x(i), y(i,j+1), z(j+1)
    write(40,*)'vertex ', x(i+1), y(i+1,j), z(j)
    write(40,*)'endloop'
    write(40,*)'endfacet'
    write(40,*)'facet'
    write(40,*)'outer loop'
    write(40,*)'vertex ', x(i), y(i,j+1), z(j+1)
    write(40,*)'vertex ', x(i+1), y(i+1,j+1), z(j+1)
    write(40,*)'vertex ', x(i+1), y(i+1,j), z(j)
    write(40,*)'endloop'
    write(40,*)'endfacet'
  end do
end do
write(40,*)'endsolid'
close(40)

stop
end

```